Journal of Energy Storage 80 (2024) 110293

Contents lists available at ScienceDirect

Journal of Energy Storage

journal homepage: www.elsevier.com/locate/est

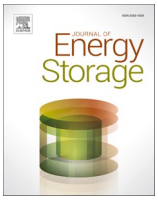

Review article

A roadmap of recent advances in MXene@MOF hybrids, its derived composites: Synthesis, properties, and their utilization as an electrode for supercapacitors, rechargeable batteries and electrocatalysis

Narasimharao Kitchamsetti [a,b,*], Jung Sang Cho [b]

[a] Department of Electronic Engineering, Institute for Wearable Convergence Electronics, Kyung Hee University, 1732 Deogyeong-daero, Giheung-gu, Yongin 17104, Republic of Korea
[b] Department of Engineering Chemistry, Chungbuk National University, Chungbuk 361-763, Republic of Korea

ARTICLE INFO

Keywords:
MOF
MXene
Composites
Supercapacitors
Metal ion batteries
HER
OER
ORR

ABSTRACT

Metal-organic frameworks (MOFs) are constructed through the self-assembly of metal ions and organic linkers. Over recent decades, MOFs have emerged as highly appealing materials in energy-related applications owing to its exceptional characteristics with high surface area, excellent porous nature, and remarkable tailor ability. However, MOFs often struggle with intrinsic issues like low electronic conductivity and susceptibility to chemical instability, factors that have significantly impeded their scalability and practical utilization. In recent times, MXene has emerged as a promising solution, given its abundant surface terminations and exceptional metallic conductivity, which may improve both the stability and conductivity of pristine MOFs. This review provides a comprehensive summary of preparation approaches for MXene@MOF related composites, encompassing MXene@MOF hybrids, MOF derived materials combined with MXene, and MXene derived materials coupled with MOF derived materials. The multifaceted properties of MXene@MOF derived composites are thoroughly examined. MXenes play a dual role in enhancing the properties of MOFs. On the one hand, they improve the conductivity as well as stability of individual MOFs. On the other hand, they introduce new functionalities, such as serving as templates. These benefits have positioned MXene@MOF derived composites for applications across various domains, including supercapacitors, batteries, and electrocatalysts. Additionally, the review delves into the effect of structural variations on the MXene@MOF derived composites properties. In closing, the authors offer insights into the future opportunities and challenges awaiting exploration in the realm of MXene@MOF derived composites.

1. Introduction

In our swiftly advancing society, the escalating consumption of Earth's resources has triggered severe environmental pollution and energy depletion. The pressing requirement for environmentally friendly, sustainable, and eco-conscious energy solutions has fueled a quest for smart, effective methods to harness, store, and employ energy [1–3]. Energy storage and conversion show a crucial role in mitigating the intermittent associated with renewable sources like wave, solar, and wind power. Presently, batteries and capacitors stand as prime examples of energy storage and conversion technologies, and they were already achieved commercial viability [4–6]. Supercapacitors, as an innovative class of electrochemical energy conversion devices, present impressive capacitance levels and possess the capability to deliver both high power and energy. They are considered promising contenders in the realm of energy storage sectors, standing alongside batteries and conventional capacitors. The effectiveness and durability of energy storage sectors, including capacitors and batteries, are profoundly impacted by the electrode materials employed [7,8]. Thus, the search for moderate and exceptional electrode materials is a major focus in addressing the energy challenges outlined in Table 1.

Since the successful isolation of two-dimensional (2D) graphene [9], the concept of 2D materials has captivated researchers worldwide leading to the discovery and exploration of various 2D materials for instance transition metal oxides [10–13], hydroxides [14,15], and sulfides [16–18]. These materials have attracted considerable attention due

* Corresponding author at: Department of Electronic Engineering, Institute for Wearable Convergence Electronics, Kyung Hee University, 1732 Deogyeong-daero, Giheung-gu, Yongin 17104, Republic of Korea.
E-mail address: kitchamsetti.rao@khu.ac.kr (N. Kitchamsetti).

https://doi.org/10.1016/j.est.2023.110293
Received 23 October 2023; Received in revised form 21 November 2023; Accepted 24 December 2023
2352-152X/© 2024 Elsevier Ltd. All rights reserved.

Table 1
The merits and demerits of two preparation approaches.

Preparation method	Merits	Demerits
In-situ growth	The structural merits of distinct components are preserved. Convenience and simple reaction conditions.	It is feasible to influence the preparation of MOFs and affect the performance.
Physical mixing	Simple and easy process route by mechanical treatment of both of their components.	Prepared derivatives whose performance is worse than that of materials organized in other strategies.

to their exceptional physical properties, such as high surface areas and superior electron transmission efficiency [19–22]. Among the diverse array of 2D materials, MXenes have emerged as a distinct class, capturing the interest of researchers since their discovery by Gogotsi and colleagues in 2011 [23]. MXenes result from the selective etching of ternary layered compounds known as MAX phases, characterized by a general equation of $M_{n+1}X_n$, where n can be 1, 2, or 3. In this formula, M represents a transition metal, A is typically denoted as Al, and X comprises nitrogen and/or carbon [24–26]. The etching process introduces surface functional groups, including O, $^{-}$OH, F, and their presence varies depending on the specific etchant employed. Presently, researchers have successfully synthesized over 30 distinct MXenes experimentally, and >100 theoretical MXenes, each exhibiting diverse physical and chemical properties, have been predicted [27–29]. Among these, $Ti_3C_2T_x$ stands out as one of the most comprehensively investigated MXenes, synthesized through the selective monoatomic Al layer etching within the Ti_3AlC_2 MAX phase precursor, a process typically involving the use of hydrofluoric (HF) acid [30]. MXenes exhibit promising potential in various fields, including energy storage, EMI shielding, electrocatalysis, sensing, and more, owing to their layered structure and extraordinary performance [31–33]. In electrochemical applications, MXenes have garnered significant attention, thanks to their remarkable metallic conductivity and hydrophilicity. For instance, $Ti_3C_2T_x$ demonstrates a specific capacitance of 1500 F. cm^{-3} (380 F. g^{-1}) using H_2SO_4 as an electrolyte [34]. Moreover, Naguib et al. [35] prepared Ti_2CT_x by etching the Al layer in Ti_2AlC with HF and used it as an anode in lithium-ion batteries (LIBs). The findings revealed a reversible capacity of 225 mA h. g^{-1} at a charge-discharge rate of C/25, slightly lower than that of conventional graphite. While MXenes alone might not exhibit exceptionally high specific capacity, their distinctive layered structure, excellent conductivity, and effective ion transport capabilities make them well-suited for incorporation into composite systems alongside other high-capacity materials. This enables the utilization of MXene-based composite materials as cathodes in lithium batteries, leading to enhanced capacity. Various composite materials incorporating MXenes, such as metal oxides [36,37], chalcogenides [38,39], graphene [40–42], carbon nanotubes [43–45], etc. (Fig. 1). These composite materials harness the strengths of each component, sparking considerable interest as a unique class of materials with promising attributes.

MOFs represent an innovative class of porous materials formed through the coordination of metal ions with organic linkers via coordination bonds [52,53]. These crystalline materials possess a significant specific surface area, distinct structure, and adjustable morphology, contributing to notable advancements in battery technology, catalysis, gas sensing, and various other domains [54–57]. The ability to control the size and shape of MOFs is crucial for their practical applications. Recent research has focused on crafting nanostructures of MOFs with precise geometric configurations, including 1D, 2D, or 3D structures [58–60]. These approaches for morphological control infuse MOFs with novel properties. In particular, the production of 1D MOF nanomaterials (NMs) has made significant advancements owing to the distinctive anisotropy of 1D nanostructures. By judiciously choosing organic linkers and inorganic metal ions, 1D nanoscale MOF materials with appealing attributes and customizable structures, such as nanowires (NWs) [61], nanorods (NRs) [62], and nanofibers (NFs) [63], can be attained. On the other hand, in the realm of 2D structures, innovative methods have been devised to govern the creation of 2D NMs, including thin films and nanosheets (NSs) [64,65]. Ultra-thin, single/multi-2D MOF NMs with high aspect ratios and abundant active sites hold great potential for various applications, like sensing and catalysis [66,67]. Typically, two notable approaches, known as the top-down and bottom-up approaches, are employed for crafting 2D MOF structures. In contrast, 3D MOFs pertain to hollow or porous structures with specific morphologies in 3D space [68]. These structures are constructed using straightforward MOF building blocks, such as MOF NPs, NRs, and NSs. These 3D components inherit the unique properties of their building blocks, including 0D NPs, 1D NRs, and 2D nanomaterials, resulting in exceptional benefits. Due to

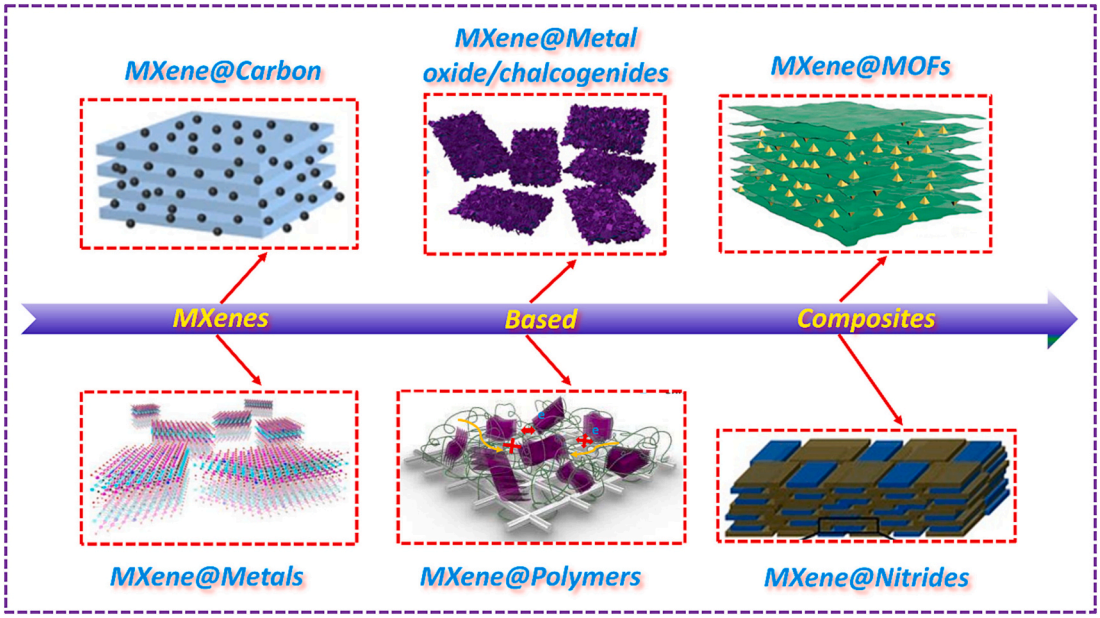

Fig. 1. MXenes based composite materials. Adopted with permission from Ref. [46–51], Copyright 2022, Elsevier B.V. Copyright 2016, Wiley-VCH. Copyright 2022, Wiley-VCH. Copyright 2019, Wiley-VCH. Copyright 2018, Springer. Copyright 2021, Springer.

its distinctive 3D structure, 3D MOFs find functions in energy storage and catalysis [69,70]. Nevertheless, pristine MOFs often exhibit inadequate conductivity, which impede its feasible use as energy storage materials. Currently, several strategies are being explored to enhance the MOFs conductivity. One approach involves the development of 2D conductive MOFs by altering the organic linkers types [71,72]. Another method is to create MOFs with high conductivity by selecting planar, conjugated, and redox-active ligands as molecular structural units [73,74]. The third strategy involves exploring multifunctional MOF-based composites. These composites exhibit novel physical and chemical properties arising from synergistic interactions between the components and structures, resulting in high activity and stability. Moreover, MOFs can perform as precursors to create MOF-derived materials that retain the porous structure of the MOF precursors while offering high conductivity [75–77].

The rapid growth of the MXene and MXene@MOF fields is evident from the increasing trend in publications since 2012 and 2013, respectively (Fig. 2a, b). The number of annual publications on MOF/MXene-based composites has been steadily increasing, indicating the growing attention from researchers in this area. Fig. 2c illustrates the widespread utilization of MOF/MXene-based composites across various fields over the past few years. These composites have found applications in batteries, supercapacitors, electrocatalysts, photocatalysts, sensors, wave absorption, and other areas, showcasing their diverse and promising potential.

Recently, there is a raising interest in MXene@MOF hybrids and their derivatives in the energy storage field [93–95]. The design of MXene@MOF hybrid materials is motivated by several factors. Firstly, MXenes, with their abundance of negatively charged surface groups, serve as excellent substrates for supporting the MOFs growth. This not only prevents the agglomeration of MXene and MOF NPs but also exposes more accessible surface areas. Furthermore, the highly conductive nature of the MXene framework within these hybrids establishes efficient conductive channels and shortens ion-diffusion pathways. Subsequently, the strong interfacial interactions between MXene and MOFs contribute significantly to superior structural integrity and stability. Lastly, the tunable crystal structures and diverse MOFs morphologies provide these hybrids with versatility for different purposes. Consequently, the utilization of MXene@MOF composites as functional materials in electrochemical sectors exhibits great promise. Moreover, optimizing and enhancing the electrochemical performance of MXene@MOF composites can be achieved by transforming MOFs into functional MOF-derived NMs. Fig. 3 shows the key properties of MOFs, MXenes, MXene@MOF composites. Indeed, the synergy resulting from the hybridization of MXene with MOFs or MOF-derived NMs effectively overcomes the inherent constraints of individual components while opening up new potentials.

This paper specifies a timely and comprehensive review of MXenes@MOFs hybrids in the context of energy storage and electrocatalysis. In contrast to prior reviews that were often focused on specific subfields, this review takes a holistic approach, centering its focus on the MXenes@MOFs hybrid structure. It thoroughly examines the advantages of these hybrids, delves into the structure-property relationship, and discusses reasonable design principles in depth. Detailed insights into the structure and synthesis routes of MXenes@MOFs hybrids are meticulously presented. The primary emphasis lies on the

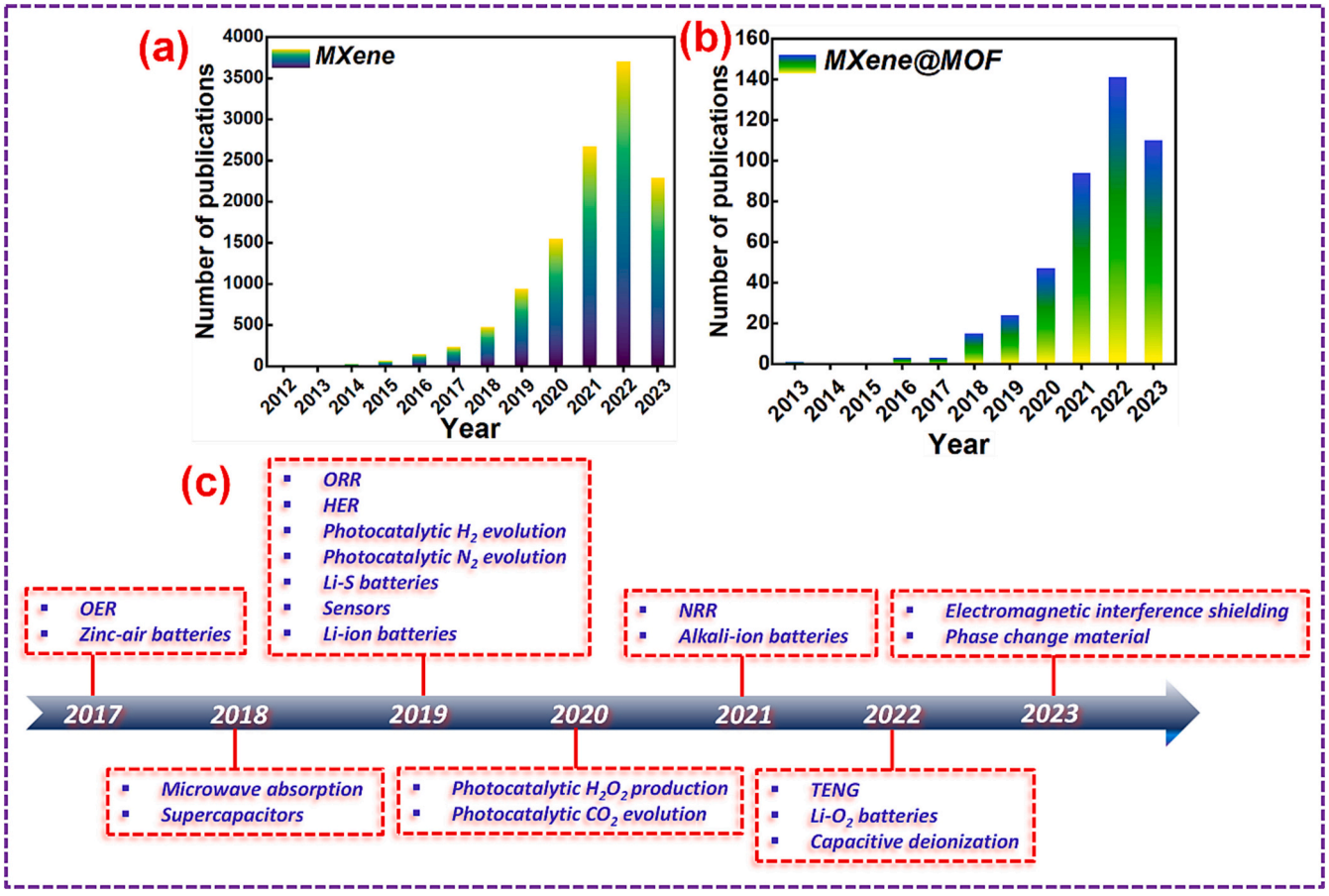

Fig. 2. (a, b) Publications of MXenes and MXene@MOF hybrids over the past few years. The data collected from the web of science by selecting the keywords "MXenes" and "MXene@MOF" derivatives (up to August 24, 2023). The publications number of MXenes almost doubled every year since 2012, and the same trend is being followed by the MXene@MOFs since 2013. (c) Timeline chart indicating the major advances of and progress in MXene@MOF hybrids in terms of their diverse preparation routes and wide range of applications [78–92].

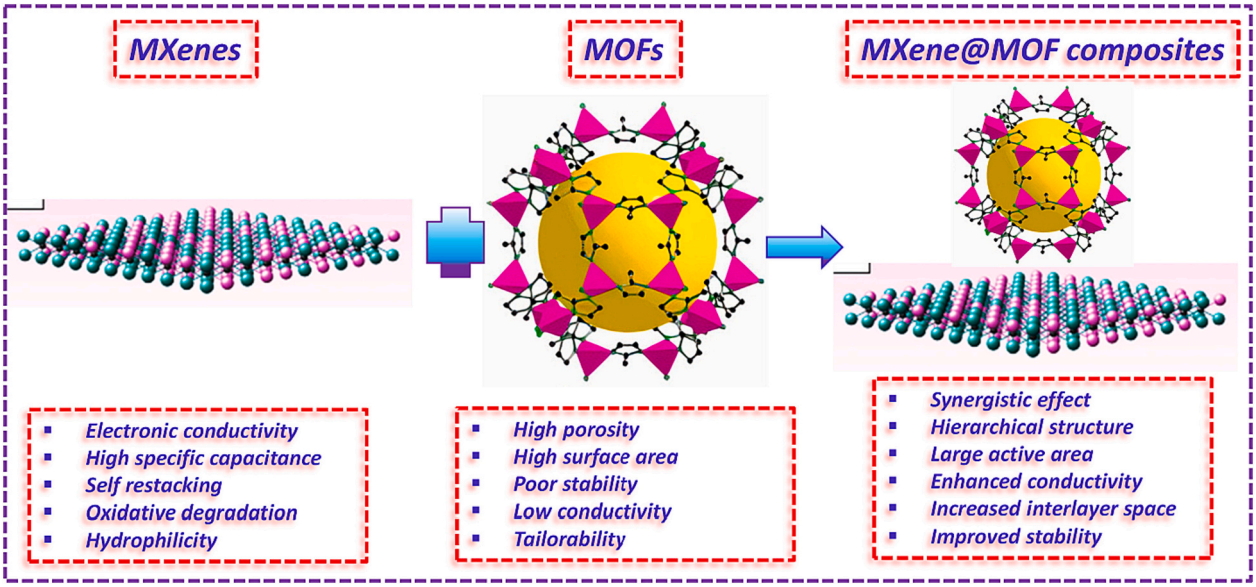

Fig. 3. The properties of MOF, MXene, and MXene@MOF composites. Adopted with permission from Ref. [96, 97], Copyright 2023, MDPI. Copyright 2020, Springer.

MXenes@MOFs application in energy storage, with special attention to recent research advancements in supercapacitors (SCs) and metal ion batteries as illustrated in Fig. 4. Furthermore, the review goes beyond merely outlining current limitations; it offers a forward-looking perspective on the future development of MXenes@MOFs materials, injecting fresh enthusiasm into this promising research area. In summary, this comprehensive review sheds light on the importance of MXenes@MOFs hybrids, elucidates their structural merits, and highlights their potential applications in energy storage and electrocatalysis. It stands as a valuable guide for advancing this exciting field.

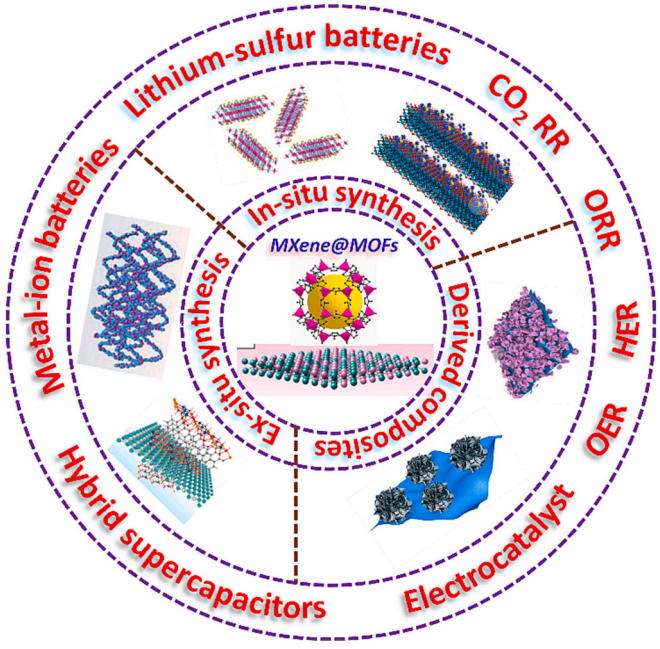

Fig. 4. The image demonstrates the synthesis routes, energy storage, and electrocatalysis applications of MXenes@MOFs hybrids. Adopted with permission from Ref. [98–103], Copyright 2021, Elsevier B.V. Copyright 2022, Elsevier B.V. Copyright 2022, Elsevier B.V. Copyright 2021, The Royal Society of Chemistry. Copyright 2023, Elsevier B.V. Copyright 2022, Elsevier B.V.

2. MXene structure, MOF structure, and MXene@MOF's hybrid structure

2.1. MXene structure

MXenes can be prepared utilizing two primary routes: top-down and bottom-up. In the top-down route, MXenes are produced by stripping them from their bulk counterparts. Conversely, bottom-up route implies the MXenes growth from atoms or molecules, like α-Mo_2C [104], yielding MXenes with fewer defects and larger transverse dimensions, which is advantageous for studying their intrinsic properties. The majority of MXenes have been prepared using the top-down approach, where specific atomic layers (e.g., Al, Si, and Ga) are selectively etched from the MAX phase. The MAX phase is a broad family of ternary carbides and nitrides, including solid solutions and ordered double-transition metal structures [97,105]. This structure consists of transition metal carbide or nitride layers interleaved with atomic layers of element A, forming a hexagonal structure [106,107]. Since M-A bonds are metallic, mechanical shearing of the MAX phase to separate the $M_{n+1}X_n$ layers and generate MXenes is not feasible. Moreover, the chemical activity of M-A bonds is higher than that of M-X bonds, permitting for the selective etching of the A-element layers. Therefore, the key to successful bottom-up synthesis lies in selecting a proper etchant.

For instance, Gogotsi's team employed HF to etch the Al layer from Ti_3AlC_2, resulting in $Ti_3C_2T_x$. HF etching is the most commonly utilized way for preparing $Ti_3C_2T_x$. Following HF treatment, the dense Ti_3AlC_2 solid undergoes a transformation into a loosely stacked multilayered $Ti_3C_2T_x$ structure, resembling an accordion. In addition to HF, MXenes can also be prepared utilizing a combination of strong acids and fluoride salts, providing an alternative to HF. Ghidiu et al. [108] achieved analogous etching outcomes as with HF by in situ reacting HCl and LiF to produce HF. The LiF-HCl etchant proved to be insignificant than HF, leading to larger laterally flaked $Ti_3C_2T_x$ with increased layer spacing, likely due to weakened interlayer interactions caused by water or cation (Li^+) intercalation. Subsequently, similar techniques applying combinations of fluoride salts (e.g., NaF, KF, and NH_4F) and acids as etchants have been successfully developed [109–111]. Moreover, MXenes can also be synthesized through alkali etching, molten salt etching, and other techniques [112–114]. It is evident that numerous etchants exist for the synthesis of $Ti_3C_2T_x$, with each etchant being suitable for specific applications. When selecting an appropriate etchant to each precursor,

consideration should be given to the anticipated material's properties and the target application.

After HF etching, the multilayer MXenes can undergo further layering through intercalation, leading to the production of few or monolayer MXenes. These few-layer MXenes are amenable to intercalation with different polar organic molecules, such as isopropylamine or larger organic base molecules [115–118]. Following intercalation, mechanical vibration or acoustic treatment in water can be applied to generate colloidal solutions of few-layer MXenes (Fig. 5a). Conversely, when using fluoride salts mixed with acids (e.g., HCl and LiF) for etching, no additional intercalation step is necessary. This is for the reason that the MXene, once etched, already contains embedded metal cations. These cations can be introduced with gentle mechanical vibration, such as through handshaking of the solution.

MXenes possess a hexagonal compact packing (hcp) crystal structure characterized by P63/mmc space group symmetry, which closely resembles that of MAX phases. In this arrangement, transition metals occupy the M sites and form a closely packed lattice, while X atoms occupy octahedral positions located among the atomic planes of M. The structural representation of MXenes is depicted as $(MX)_nM$, where there is n + 1 layers of M covering n layers of X [121,122]. MXenes come in various formulations based on their structure, including M_2X, M_3X_2, and M_4X_3. In wet chemical etching, MXenes typically undergo complete termination, with the addition of surface atoms like O, OH, F, H, and/or Cl. Density functional theory (DFT) investigations have confirmed the thermodynamic stability of functionalized MXenes [123,124]. Remarkably, fully functionalized MXene surfaces exhibit greater stability when compared to partially functionalized ones. In summary, MXenes exhibits a layered NS structure enriched with rich surface functional groups. The composition and proportion of elements determine the specific surface chemical groups present in each MXene. In the realm of 2D materials, MXenes are distinctive, renowned for their exceptional chemical properties, which arise from their outstanding metal conductivity and the hydrophilic nature of their terminal groups, which can be $^{-}$OH or O.

2.2. MOF's structure

The concept of MOFs was originally proposed by Yaghi and Li et al. [125] in the year 1990. MOFs represent a class of porous crystalline materials characterized by lattice-structured crystals, formed through the strong coordination of metal ions to organic linkers via robust coordination bonds (Fig. 5b). They offer numerous advantages, including excellent crystallinity, the flexibility to tune crystal structures, and adjustable compositions [126,127]. The adaptability of MOFs arises from their ease of customization through alterations in organic ligands, metal components, or adjustments to the synthesis conditions [128]. To date, over 20,000 distinct MOFs with diverse crystal structures, compositions, and morphologies have been discovered, and this number continues to grow [129]. Within MOFs, the framework is constructed from metal ions, which constitute secondary building units (SBUs). Examples of these SBUs include $Zn_4O(COO)_6$, $Cu_2(COO)_4$, $Cr_3O(H_2O)_3(COO)_6$, and $Zr_6O_4(OH)_{10}(H_2O)_6(COO)_6$ [130–132]. These nodes are interconnected through coordination bonds with organic linkers,

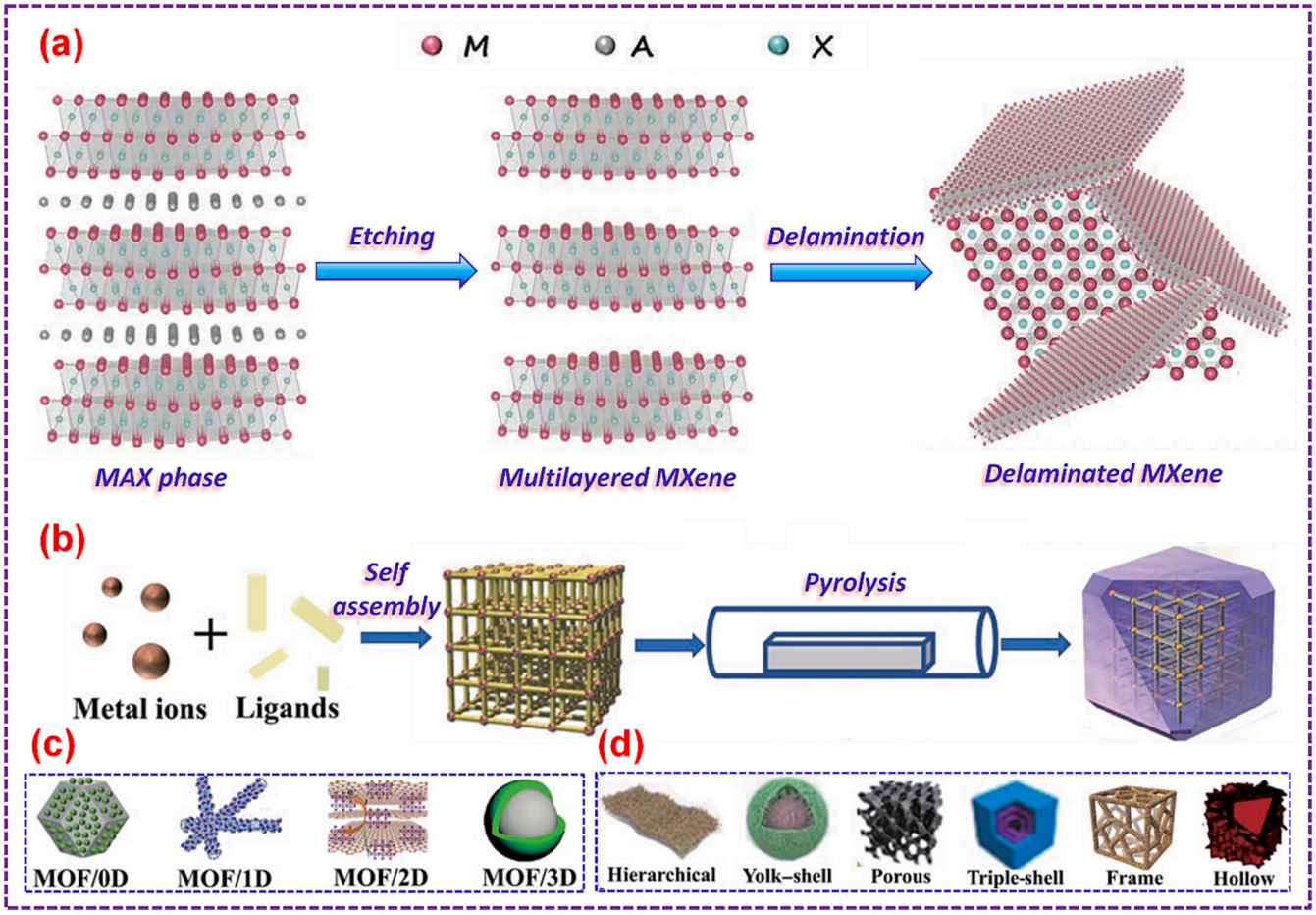

Fig. 5. (a) The synthesis of MXene from the MAX phase. Adopted with permission from Ref. [119], Copyright 2021, Wiley-VCH. (b) Pictorial representation of controlled preparation of MOFs, and their derived composites. Morphology design of MOF (c) composites, and (d) derivatives. Adopted with permission from Ref. [120], Copyright 2022, Springer.

often featuring carboxylates, phosphonates, pyridines, imidazolates, or other azole acid functional groups. The combination of various linkers with metal nodes or SBUs, each having diverse geometries and connectivity, results in a wide array of framework topologies.

Various kinds of MOFs have been extensively examined, and some of the most notable ones are as follows:

1. *Iso-reticular MOFs (IRMOFs)*: These materials primarily consist of $[Zn_4O_6]^+$ metal clusters bonded to organic ligands based on carboxylic acids, which give rise to substantial pores and a high pore capacity. For instance, MOF-5, belonging to the IRMOFs series, was initially synthesized by Yaghi's research group. They employed zinc ions and 1,4-phenylene terephthalic acid to create 3D materials [133]. MOF-5 stands out due to its remarkable specific surface area and its exceptional ability to adsorb gases and organic molecules.
2. *Zeolitic Imidazolate Frameworks (ZIFs)*: ZIFs exhibit various structures and can be readily functionalized. Among the different types, ZIF-8 and ZIF-67 are the most frequently encountered. These materials are recognized for their robust thermal and chemical stability, with ZIF-8, in particular, demonstrating exceptional resistance to an 8 M NaOH aqueous solution even at elevated temperatures for prolonged durations [134].
3. *Lavoisier Material Institute (MILs)*: MILs employ trivalent transition metal ions coordinated with carboxylic acid dependent linkers. These substances boast exceptionally large surface areas, with MIL-100 and MIL-101 representing two of the more prevalent variants [135].

These different types of MOFs offer diverse structural and adsorption properties, making them highly promising materials in various applications. Initially, MOF materials were mainly used for gas storage, but their applications have expanded to various fields, including drug delivery, multiphase catalysis, and gas/liquid adsorption and separation [136,137]. With their pore volume and large specific surface area, MOFs are now being explored as probable candidates for advanced energy storage technologies. Through careful selection and processing of building blocks during synthesis, MOFs can be tailored to exhibit desired properties. Notably, the porosity of MOFs is a crucial feature that significantly influences energy storage and charge transport processes [138,139].

2.3. MXenes@MOF's structure

As discussed earlier, MOFs exhibit promising potential for many applications, specifically in the energy storage field. Nonetheless, their practical utility is hampered by inherent issues related to poor conductivity and stability. To address these limitations, researchers have harnessed the capabilities of MOFs by incorporating them into composites with NMs like metal oxides, CNTs, activated carbon (AC), graphene, and conducting polymers [140–144]. These composite materials not only enhance the whole conductivity but also introduce novel properties through synergistic effects. Additionally, MOFs can assist as valuable templates for producing derived materials that exhibit improved conductivity and stability. By subjecting them to controlled calcination processes, a variety of nanostructured derivatives have been synthesized, making use of MOFs as versatile multifunctional templates and precursors. These MOF-derived NMs offer distinct benefits over conventional MOFs, involving controlled morphology, increased surface area, enhanced electrical conductivity, and a more regular structure, as illustrated in Fig. 5c,d. Furthermore, utilizing MOF composites as precursors expands the range of potential multifunctional superstructures.

2D MXenes offer numerous advantages, including their spacious specific surface area, diverse chemical composition, adaptable interlayer spacing, and excellent metallic conductivity. These qualities make them versatile for EMI shielding, photocatalysis, and energy storage applications. Furthermore, the existence of electronegative functional groups on the MXene surface provides effective anchoring sites for other active materials, resulting in advanced electrical conductivity and exceptional performance in MXene composites. However, the persistent challenge of self-stacking can undermine the electrochemical properties of MXenes. Fortunately, the integration of MXenes with MOFs offers a compelling solution. Combining MXenes with MOFs not only overcomes the self-stacking issue but also improves the conductivity and stability of the resulting composites, rendering them highly suitable for practical electrochemical applications. The formation of MXenes@MOFs composites can occur through various methods, including in situ synthesis, simple mixing, and more. Alternatively, MXenes and MOFs can serve as sacrificial precursors to generate MXenes@MOFs derived NMs. In the upcoming sections, we will initiate design strategies for MXenes@MOFs structures and examine their microstructure through structural characterization.

3. Preparation routes

MOFs are fabricated by linking metal ions with polydentate organic ligands through coordination bonds [145]. These structures are highly adaptable, making MOFs an excellent precursors that can be converted into carbon materials, metal oxides, and various compounds through derivatization. On the other hand, MXenes represents novel 2D layered materials with outstanding conductivity [146,147]. However, they are prone to oxidation [148,149]. Because of the existence of reactive metal atoms on their surface. These metal atoms can spontaneously react with oxygen-containing groups, resulting in the formation of more stable metal oxides in the presence of air and water [150,151]. To improve the oxidation resistance of MXenes, vacuum drying/freeze-drying techniques are frequently employed [152,153]. Additionally, the addition of antioxidants like dimethyl sulfoxide (DMSO), can be effective [152]. Moreover, MXenes can serve as templates for the creation of MXene-derived materials, inheriting the advantageous properties of MXenes. Given the derivatization potential of both MXenes and MOFs, MOF@MXene based composites can be classified into three primary categories: MOF@MXene composites, MOF derivatives@MXene composites, and MOF derivatives@MXene derivatives. Table 2 provides an overview of the latest preparation approaches for these MOF@MXene based composites.

3.1. MXene@MOF

3.1.1. In-situ synthesis

In-situ preparation is a widely employed approach for fabricating composites due to its ability to facilitate spontaneous growth, leading to a strong bonding interface in the resulting material [170]. This approach offers the advantage of streamlining the process and avoiding intricate multi-step procedures. When it comes to MOF/MXene composites, the preparation involves adding MXenes to solutions containing well-dissolved metal ions and organic ligands, and the composite is formed using the same synthesis procedure as that used for MOFs. This method encompasses various techniques, including ambient temperature diffusion, interdiffusion reactions, hydrothermal methods, and others [171–174].

The ambient temperature diffusion technique stands out as one of the cost-effective and straightforward preparation techniques owing to its simplicity and mild preparation conditions [11,175–177]. For example, Wang's group prepared Ni-MOF/$Ti_3C_2T_x$ hybrid NSs by introducing $Ti_3C_2T_x$ into a solution containing Ni^{2+} ions and terephthalic acid, then stirring the mixture at room temperature [178]. Similarly, Luo's group prepared bimetallic CoNi-ZIF-67/$Ti_3C_2T_x$ composites by adding MXenes to a solution encompassing Co^{2+} and Ni^{2+} ions, 2-methylimidazole, and CTAB, followed by stirring (Fig. 6a) [179]. The existence of the CTAB ensured a strong attachment of the surface layers of accordion type $Ti_3C_2T_x$ to numerous CoNi-ZIF-67 particles (Fig. 6b). XRD analysis confirmed that the structure and composition of CoNi-ZIF-67/$Ti_3C_2T_x$

Table 2
Summary of the various preparation strategies of MXene@MOF composites.

Classification	Composite	Preparation strategy	Reaction solvent	Morphological variation	Application	Ref.
MXene@MOF	MXene/Ni-MOF	Stirring (In-situ synthesis)	DI water	Pillared-layer structure	ASCs	[154]
	Fe-MOF/MXene	Hydrothermal (In-situ synthesis)	DMF	Flake type structure	Sensor	[155]
	Ti_3C_2@MIL-NH_2	Hydrothermal (In-situ synthesis)	Methanol, DMF	Hierarchical structure	Photocatalytic	[156]
	Co-MOF/$Ti_3C_2T_x$@Ni-foam (NF)	Stirring (Direct mixing)	DMF	Multilayered microstructure	SCs	[157]
	nMOF-867/MXene	Solvothermal (In-situ synthesis)	DMF	3D hierarchical structure	LIBs	[158]
	MXene-ZIF-8 membrane	EPD and FCDS (Electrochemical synthesis)	DI water	Dual layered membrane	H_2/CO_2 seperation	[159]
	$Ti_3C_2T_x$@Co-BDC	Interdiffusion reaction-assisted (In-situ synthesis)	DMF/CH_3CN	2D/2D structure	OER	[78]
	ZIF-67@Ti_3C_2	Stirring (Direct mixing)	Methanol	–	NRR	[85]
	Ti_3C_2/NiCo-MOF	Sonication (Self-assembly)	Water	3D hierarchical structure	LIBs	[160]
MOF/MXene derivatives	$NiSe_2$-$CoSe_2$@C/ $Ti_3C_2T_x$	Selenization (400 °C, Ar) (In-situ synthesis)	Methanol	Heterogeneous interfacial structure	MA	[161]
	ZnS/MXene	Sulfidation (60 °C, Ar) (In-situ synthesis)	Methanol	0D-2D structure	LIBs	[162]
	MXene-Ni-Co@NiCo-MOF/NF	Hydrothermal, Electrodeposition (Electrochemical synthesis)	DI water/ DMSO	Hexagonal structure	HSCs	[163]
	Co-CNS/MXene foams	Pyrolysis (450 °C, Ar) (In-situ synthesis)	DI water	Hierarchical structure	Solar water desalination	[164]
	alk-Ti_3C_2/N-PC/GCE	Ultrasonic (Self-assembly)	DI water	Heterostructure	Sensor	[165]
	Co_3O_4@NGC/MX	Pyrolysis (600 °C, Ar and 250 °C, Ar) (In-situ synthesis)	Methanol	2D structure	LIBs	[166]
	Ti_3C_2/TiO_2/UiO-66-NH_2	Pyrolysis (600 °C, N_2), hydrothermal (In-situ synthesis)	DMF	–	Photocatalytic	[167]
	Co-CNT/Ti_3C_2	Pyrolysis (800 °C, H_2/N_2) (In-situ synthesis)	Methanol	Nanotubes/Nanosheets	ORR	[168]
	Fe&TiO_2@C	Pyrolysis (700 °C, H_2/Ar) (In-situ synthesis)	DMF	Sandwich structure	MA	[169]
	CoO_x-N-C-TiO_2/C	Pyrolysis (800 °C, N_2) (In-situ synthesis	Methanol	3D porous structure	HER. OER, and ORR	[87]

remained unchanged (Fig. 6c). Moreover, Pang et al. fabricated 3D MXene@Ni-MOFs composites. They dispersed MXene in a solution containing double deprotonated linkers (Bpy and Tdc), and then combined Ni-II with the organic linkers adsorbed on MXenes through stirring [154].

Hydrothermal and solvothermal methods have become essential for MOF synthesis due to their requirement for precise temperature and pressure control [10,12,20,24]. Huang's team successfully synthesized Ti_3C_2@MIL-NH_2 materials through a hydrothermal treatment at 120 °C for 84 h, using a mixture of methanol and DMF as solvents. SEM images demonstrated the uniform attachment of MIL-NH_2 onto the layered MXene surface (Fig. 6d, e). Additionally, XRD analysis revealed that Ti_3C_2 and MIL-NH_2 did not undergo any phase transition during the process (Fig. 6f) [156]. In another study by Xu et al., a one-step hydrothermal technique was used to create Fe-MOF/MXene composites utilizing DMF as a solvent. The octahedral Fe-MOF particles were evenly distributed on the flake type MXenes, as observed through microscopy. XRD analysis further confirmed that the Fe-MOF/MXene diffraction peaks matched those of MXene and Fe-MOF, indicating the successful synthesis of Fe-MOF/MXene [155].

The interdiffusion reaction-assisted technique offers the benefits of not requiring a surfactant and being easy to process. Huang et al. employed this method to in situ hybridize $Ti_3C_2T_x$ and cobalt 1,4-benzoate (Co BDC) through mutual diffusion (Fig. 6g). The reaction tube used in the mutual diffusion process contained 3 layers as shown in Fig. 6h. The top layer consisted of MXene NSs and Co^{2+}, and owing to the MXenes electronegativity, Co^{2+} closely bonded with the MXenes. The middle layer acted as a buffer, while the bottom layer contained the BDC organic linker. As the MXene including Co^{2+} sank, it combined with BDC due to gravity, leading to the formation of the $Ti_3C_2T_x$-Co BDC hybrid material. This method effectively controlled the metal ion rate and ligand binding in the mixed solvent methods, allowing Co BDC to seamlessly coat the $Ti_3C_2T_x$ NSs (Fig. 6i, j) [78]. Zhang et al. [180] positively synthesized advanced battery-type electrode by utilizing the ample electronegative active sites on MXene to facilitate the MOF nucleation and growth, subsequently transforming it in situ into porous NiP (Fig. 7a). Ramachandran's team [157] employed in situ growth to develop unique Co-MOF/$Ti_3C_2T_x$ composites on NF electrodes, which served as binder-free electrodes for SCs. These electrodes presented exceptional energy storage performance in a 3 M KOH electrolyte. Bu et al. [181] synthesized mesoporous $Co_3O_4/Ti_3C_2T_x$ nanocomposites by in-situ growing MOFs on $Ti_3C_2T_x$ sheets for ethanol sensing. These $Co_3O_4/Ti_3C_2T_x$ sensing membranes demonstrated ultra-high responsiveness, excellent selectivity, and stability in ethanol sensing. Du's team [182] conducted in situ growth of a series of bimetallic MOF NSs encompassing Co and Ni on $Ti_3C_2T_x$ MXene NSs and investigated their impact on the oxygen precipitation. Likewise, Shi and his group [183] effectively fabricated composites consist of UiO-66-NH_2(Zr/Ti) carboxy-functionalized MXene (UZT/CFMX) by the carboxylate supported coordination method (Fig. 7b). Through the formation of coordination bonds, strong interactions were established between the two NMs, suppressing electron-hole pair recombination, and offering a versatile approach to construct more effective MOF/MXene composites for the photocatalytic water splitting.

3.1.2. *Ex-situ synthesis*

The ex-situ preparation route involves integrating the separately designed MXene and MOF using methods such as self-assembly, direct mixing, and electrochemical techniques. Unlike the in-situ methods, these approaches are not influenced by the specific conditions of MOF synthesis. As a result, they offer high operability and flexibility.

3.1.2.1. Direct mixing. The direct mixing method involves the combination of prepared MXene and MOF in a solution to create the MOF@MXene composite. For example, Wang and his team built a novel microporous composite, MIL-100(Fe)/Ti_3C_2, by directly mixing MIL-100 with varying amounts of MXenes. This composite was employed as a photocatalyst to enhance nitrogen fixation capabilities [79]. In certain applications where MOFs are used as an electrode for SCs or glassy carbon electrodes (GCE), conductive agents like MXene are often introduced to enhance the conductivity. This is achieved through techniques such as drop casting with MOFs. For instance, Liu and his team sequentially tailored a 3D flower type Cu-MOF and MXene onto a GCE using drop casting, creating a platform for H_2O_2 sensing (Fig. 8a, b)

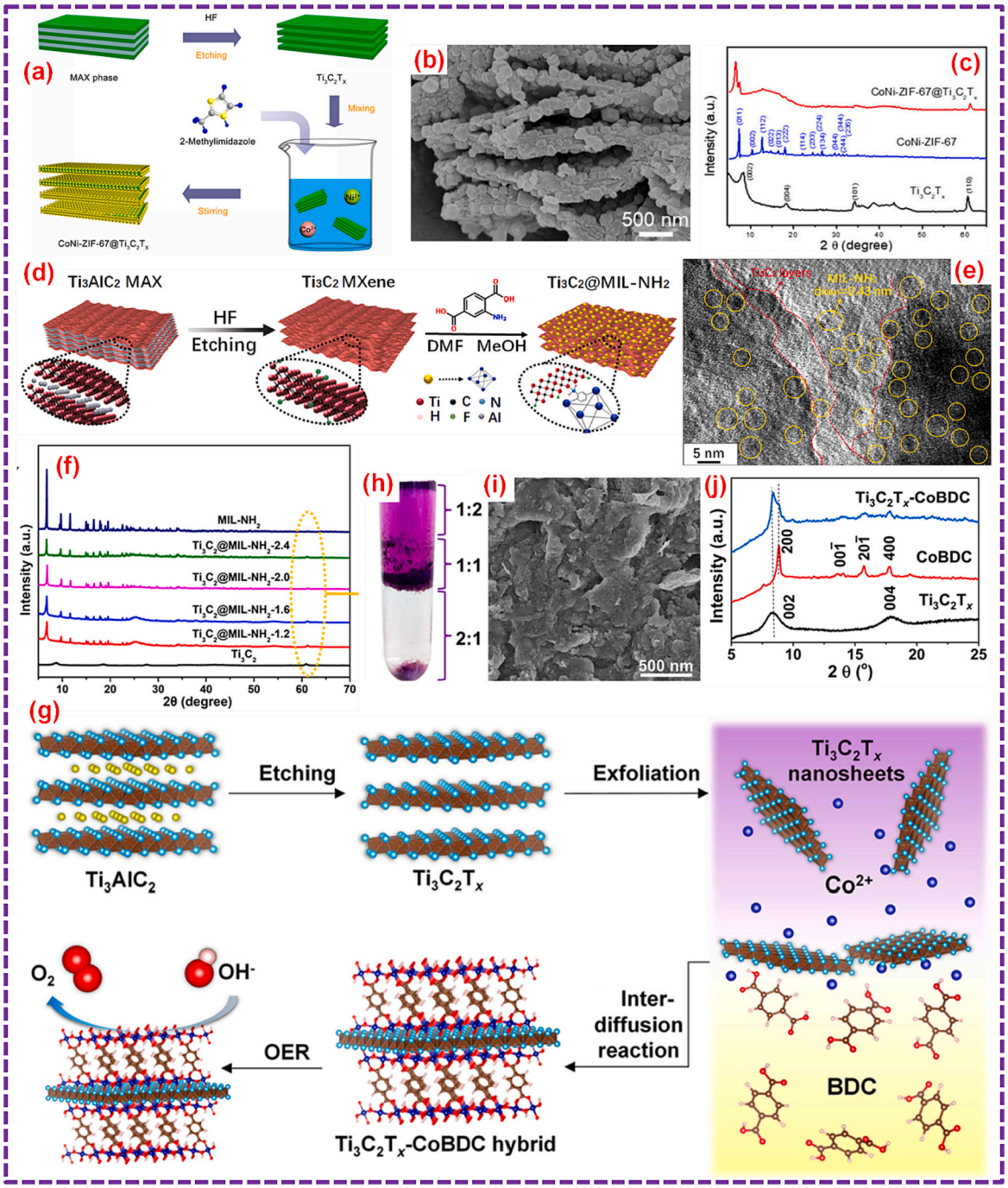

Fig. 6. (a) Preparation scheme of CoNi-ZIF-67@$Ti_3C_2T_x$. (b) SEM of CoNi-ZIF-67@$Ti_3C_2T_x$. (c) XRD. Adopted with permission from Ref. [179], Copyright 2019, MDPI. (d) Schematics of Ti_3C_2@MIL-NH_2. (e) HR-TEM of Ti_3C_2@MIL-NH_2–1.6. (f) XRD. Adopted with permission from Ref. [156], Copyright 2021, Elsevier B.V. (g) Preparation scheme of $Ti_3C_2T_x$-CoBDC for OER. (h) Image of a test tube. (i) Side view of the $Ti_3C_2T_x$-CoBDC. (j) XRD. Adopted with permission from Ref. [78], Copyright 2017, The American Chemical Society.

[184]. Similarly, Sun et al. reported a GCE by direct mixing of Ce-MOF and $Ti_3C_2T_x$ for the L-Tryptophan detection using electrochemical techniques [185].

3.1.2.2. Self-assembly. Self-assembly is a process guided by π-π stacking, electrostatic interactions, hydrogen bonding, and other processes, which leads to the spontaneous formation of well-ordered structures [186]. Cheng and his colleagues employed self-assembly driven by hydrogen bonding to combine NiCo-MOF sheets with 2D Ti_3C_2 (Fig. 8c). This arrangement resulted in a 3D porous structure where the 2D Ti_3C_2 and NiCo-MOF NSs intricately interweaved and tightly interconnected, as depicted in Fig. 8d [160]. In a similar vein, Liu and his team devised a unique Co-ZIF-9/Ti_3C_2 composite using an electrostatic self-assembly approach, which was then employed for the H_2 production [187].

3.1.2.3. Electrochemical preparation technique. The electrochemical preparation process offers the several advantages including gentle reaction conditions, straightforward operation, and controllable parameters [188,189]. For example, Wang's research team achieved the formation of an 800 nm thick 2D MXene layer on a Cu disk through electrophoretic deposition within just 1 min. Subsequently, they initiated the growth of a 450 nm thick ZIF-8 layer atop the MXene layer

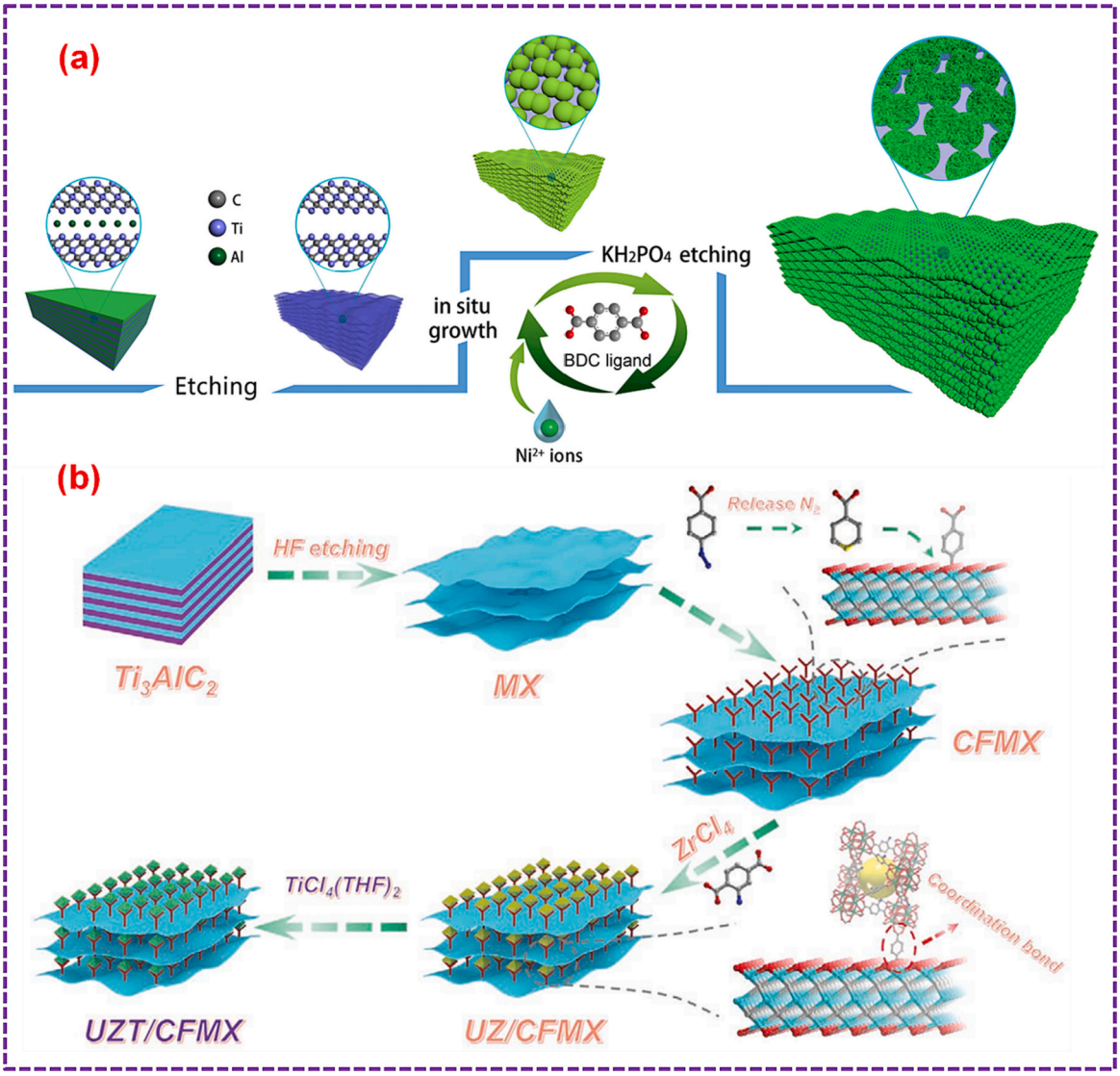

Fig. 7. (a) Schematic presentation of the preparation strategy to the MXene-NPO. Adopted with permission from Ref. [180], Copyright 2021, Elsevier B.V. (b) Pictorial representation for fabricating the UZT/CFMX heterostructure. Adopted with permission from Ref. [183], Copyright 2022, Wiley-VCH.

using rapid current-driven production over a span of 20 min. This innovative approach led to the creation of the MXene-ZIF-8 composite film, as illustrated in Fig. 8e, f [159]. Similarly, Dai and his colleagues prepared Co-MOF via a hydrothermal approach and subsequently utilized it as a substrate for electrodepositing in a mixed solution encompassing Co^{2+}, Ni^{2+}, and MXene. This process resulted in the formation of MXene-Ni-Co@NiCo-MOF/NF NSs [163]. In a broader context, the combination of cationic polymer-functionalized MOFs and negatively charged MXene provides a convenient means of assembly. An excellent example of this synergy is the successful preparation of MXene-encapsulated Ni-naphthalene dicarboxylic acid (Ni-NDC) NSs. This achievement involved the mixing of MXene with poly(diallyldimethylammonium chloride) (PDDA)-modified Ni-NDC at room temperature, as depicted in Fig. 9a [190]. The pre-existing Ni-NDC displayed a distinctive flower-type configuration, comprising numerous small-sized NSs assembled. However, upon the introduction of MXene, a uniform dispersion of Ni-NDC NSs within the MXene framework ensued. This arrangement was facilitated by interlayer hydrogen-bond interactions between the organic linker of Ni-NDC and the MXene surface terminal groups. This interaction successfully expanded the spacing of interlayer, consequently inhibiting the self-stacking of MXene or Ni-NDC. Importantly, the concept of surface charge modification extends beyond MOFs. Another instance involves the utilization of PDDA to induce a positive surface charge on V_2CT_x MXene. This strategic adjustment facilitated the composite formation of V_2CT_x with negatively charged 2D Cu-HHTP (HHTP = 2,3,6,7,10,11-hexahydroxytriphenylene), as illustrated in Fig. 9b [191]. The resulting Cu-HHTP@MXene heterostructures consisted of alternating layers of V_2CT_x MXene NSs and Cu-HHTP. This integration exploited the electrostatic interaction between MXene and MOFs, effectively preventing the restacking of 2D Cu-HHTP and V_2CT_x NSs.

Crucially, certain MOFs exhibit an innate capability to seamlessly integrate with MXene, obviating the need for surface charge modulation. A case in point is the work of Tan et al. [102] who achieved the successful synthesis of a series of 2D/2D Co_2Ni-MOFs/$Ti_3C_2T_x$ composites via a straightforward ultrasound technique depicted in Fig. 9c. Through electrostatic assembly, ultrathin Co_2Ni-MOFs harmoniously amalgamated with MXene, resulting in a heterostructure that maximized existing surface areas and averted the undesired agglomeration of 2D NSs. Additionally, Zhao et al. [192] pioneered the fabrication of MXene/metal-porphyrin framework (MPF) composite using a viable vacuum supported filtration approach depicted in Fig. 9d. The MPF NSs featured an abundance of terminal carboxy groups on their surface, facilitating facile interconnection with MXene via interlayer hydrogen

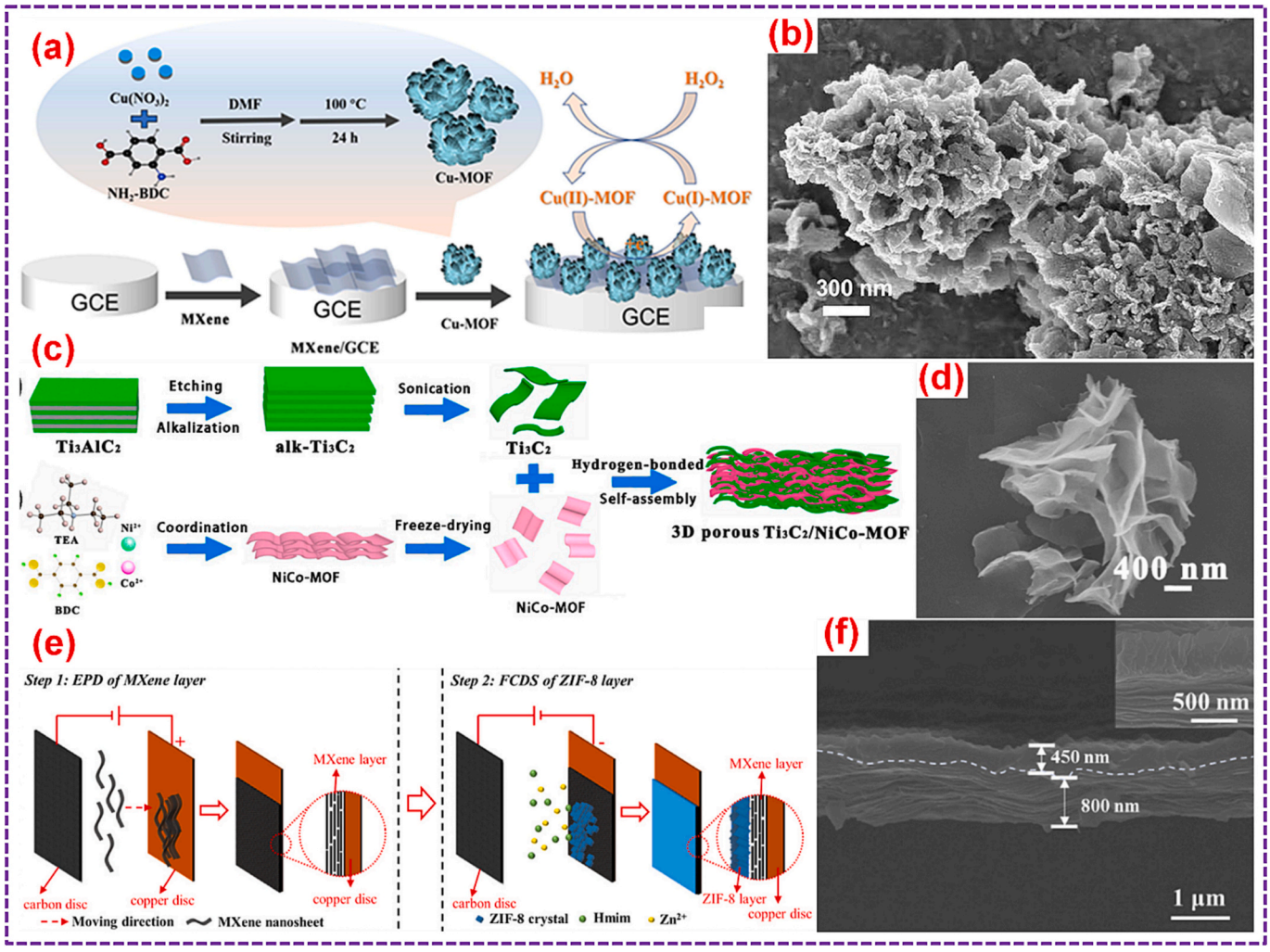

Fig. 8. (a) Schematic illustration of Cu-MOF/MXene/GCE. (b) SEM picture of Cu-MOF/MXene/GCE. Adopted with permission from Ref. [184], Copyright 2021, Wiley-VCH. (c) Pictorial representation of Ti_3C_2/NiCo-MOF. (d) SEM image of Ti_3C_2/NiCo-MOF-0.4. Adopted with permission from Ref. [160], Copyright 2020, MDPI. (e) Fast preparation of MXene-ZIF-8. (f) SEM picture of the MXene-ZIF-8 composite membrane. Adopted with permission from Ref. [159], Copyright 2022, Elsevier B.V.

bonds as illustrated in Fig. 9e, the resultant MXene/MPFs composite film exhibited a meticulously arranged stacking of NSs, guided by the presence of MPFs as effective spacers. This architectural strategy contributed to the creation of a porous interconnected network, enhancing the overall structure. As evidenced in Fig. 9f, a comparison of the peak shifts further substantiates the substantial enlargement of interlayer spacing within the synthesized MXene/MPFs film. In contrast to the more prevalent methods involving hydrogen bonds and van der Waals forces, the utilization of mechanochemical preparation for creating MXene@-MOF composites has been relatively less explored. This discrepancy could be attributed to challenges like inconsistent product uniformity and potential structural degradation of raw materials. Nonetheless, it's undeniable that physical mixing remains an uncomplicated and readily applicable approach for hybrid synthesis. As an illustration, a straightforward ball milling method was introduced to effectively couple $Ti_3C_2T_x$ and UiO-66 [193].

3.2. MXene@MOF derivatives

Two distinct preparation pathways are employed to create MXene@MOF derivatives structures. The first involves the synthesis of MXene@MOF derivative composites through either ex-situ or in-situ techniques, which are subsequently employed as precursor materials for the fabrication of MOF derivatives/MXene. The second route entails the initial synthesis of MOF materials, followed by their transformation into MOF derivatives. These derivatives are then combined with MXenes. This process of derivatization facilitates the conversion of initially low-activity MOFs into high-activity materials, such as carbon NMs or various metallic components (i.e., hydroxides, sulfides, oxides, phosphides, or selenides).

3.2.1. MXene@carbon nanomaterials

Carbon structures offer a range of advantages, including notable flexibility, remarkable chemical stability, cost-effectiveness, excellent electronic conductivity, and low toxicity [194,195]. MOFs have emerged as valuable sacrificial precursors, directly undergoing carbonization to yield carbon structures [196,197]. The metallic constituents within MOFs would be eliminated through processes like high-temperature evaporation or acid treatment [198,199]. For instance, Li et al. achieved the in-situ decoration of ZIF-67 NPs onto 2D ultra-thin Ti_3C_2 NSs. Subsequently, these materials were subjected to calcination in an Ar (90 %)/H_2 (10%) atmosphere for 2 h at 800 °C, followed by the removal of metal ions via acid treatment. During the carbonization mechanism, ZIF-67 served as a source of N_2, resulting in the inclusion of N_2 within Ti_3C_2 MXene. This intricate sequence resulted in the formation of a nitrogen-doped Ti_3C_2/carbon 2D heterostructure (N- Ti_3C_2/C),

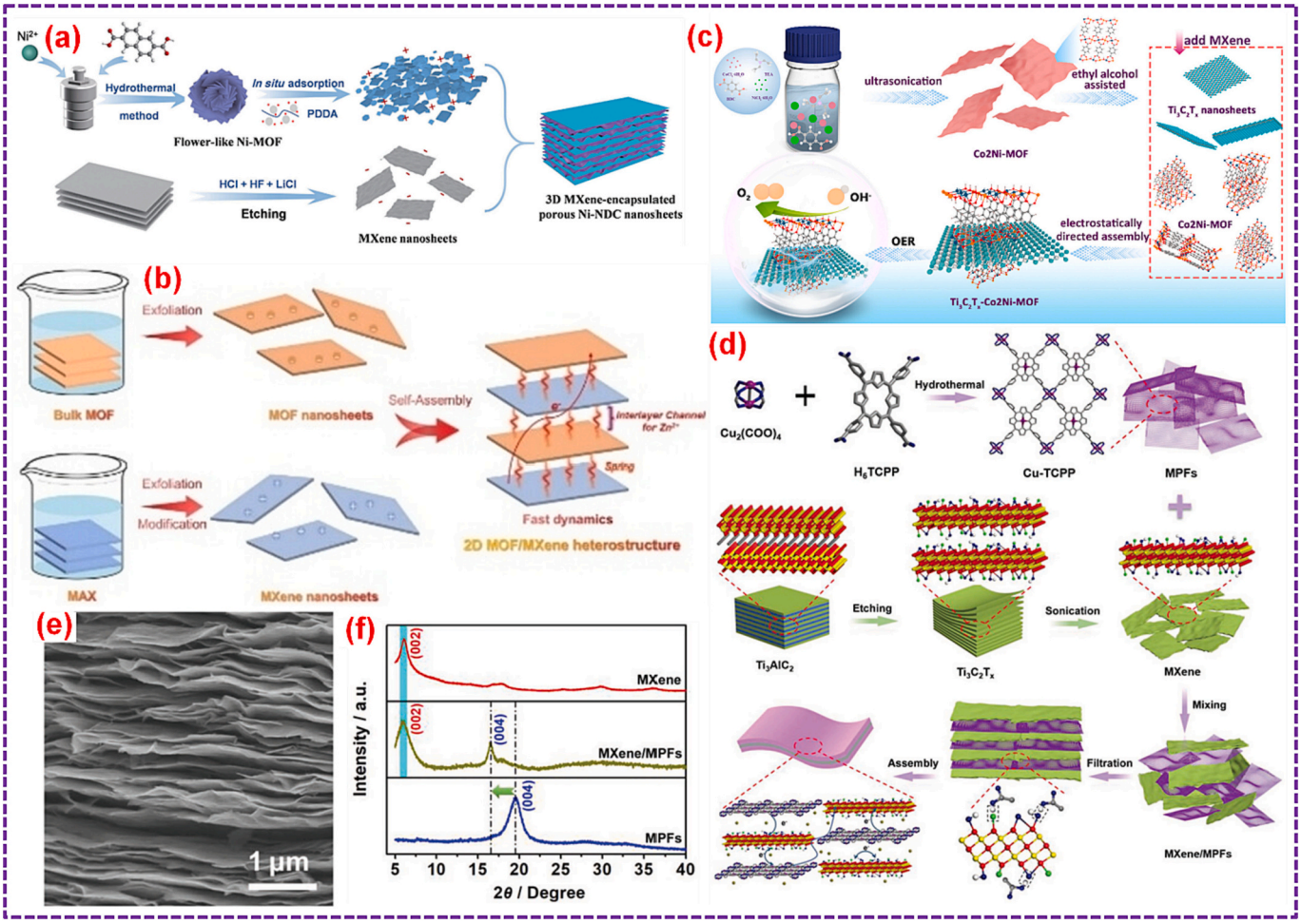

Fig. 9. (a) Pictorial presentation of the Ni-NDC@MXene hybrids preparation. Adopted with permission from Ref. [190], Copyright 2022, Springer. (b) The hybridization of V_2CT_x MXene NSs and Cu-HHTP. Adopted with permission from Ref. [191], Copyright 2022, Wiley-VCH. (c) Schematics representation of the Co_2Ni-MOF@MXene preparation. Adopted with permission from Ref. [102], Copyright 2023, Elsevier B.V. (d) Pictorial representation, and (e) Side view images of MXene/MPFs films. (f) XRD plots of MPFs, MXene, and MXene/MPFs films. Adopted with permission from Ref. [192], Copyright 2019, Wiley-VCH.

which found application in lithium-sulfur battery (LSBs) diaphragms [200]. Similarly, Jiang et al. carbonized MOF-5-NH_2 in an Ar environment for 2 h at 900 °C, followed by acid pickling to extract inorganic components and create nitrogen-doped porous carbon (N-PC). Subsequently, N-PC was self-assembled with Ti_3C_2, yielding alk-Ti_3C_2/N-PC. The presence of abundant surface C—N bond and the $^-$OH groups in alk-Ti_3C_2/N-PC facilitated impressive sensing capabilities for benzenediol [165].

3.2.2. *MXene@metal compounds*

MOFs exhibit the capability to generate double hydroxides [201,202]. The preparation mechanism involves the formation of layered double hydroxides (LDHs) through a sequential process. Initially, metal salts, such as $Co(NO_3)_2$, $Cu(NO_3)_2$, $Ni(NO_3)_2$, and the like, are introduced into the MOF solution. The ensuing hydrolysis of metal salts produces H^+ ions that gradually initiate the MOFs etching and the liberated ions of metal from the MOFs experience partial oxidation through dissolved O_2 and NO^{3-} ions. Subsequently, these metal ions undergo co-precipitation with cations present in the metal salts, ultimately giving rise to the formation of the LDH structure [203,204]. In a notable example, Deng et al. achieved the anchoring of Co-Co-LDH onto MXene via an in-situ etching followed by the co-precipitation methodology [81]. Meanwhile, Pang's research group fabricated hierarchical ZIF-67/$Co(OH)_2$ composites with MXene, featuring diverse structures like core-shell, yolk-shell, and hollow arrangements, through precise in-situ etching. These tailored composites were harnessed as supercapacitor electrode materials, as shown in Fig. 10a-d [205].

Elevated-temperature treatment serves as a crucial step in the transformation of metal ions within MOFs into the constituent metals in their derived materials. By subjecting the MOFs to this process, the organic ligands are eliminated, resulting in the formation of porous oxides, selenides, sulfides, and phosphates of metal [207,208]. Notably, MOF-derived oxides of metal retain the advantageous characteristics of the parent MOFs, including a suitable porous architecture, high surface area, excellent electrical conductivity, and low density [75,209,210]. However, the utilization of metal oxides as electrode materials can be impeded through their propensity for volume expansion during charging and discharging cycles, resulting to rapid capacity decay. These composites would serve as volume buffers, when combined with MXenes, alleviating internal pressure and thereby enhancing the overall electrochemical activity [160,211]. Sun's research team tactically orchestrated the assembly of negatively charged MXene NSs with positively charged ZIF-67 derived CoMo-LDH, yielding a hollow MXene@CoMo-LDH composite. Subsequent calcination at 350 °C in a N_2 environment for 2 h resulted in the MXene@CoO/$Co_2Mo_3O_8$ formation. This composite was effectively utilized as an anode for lithium-ion batteries (LIBs). The synergistic interplay between the constituents endowed the CoO/$Co_2Mo_3O_8$@MXene electrode with remarkable reversibility and rate performance [82]. In a parallel endeavor, Yu's group devised

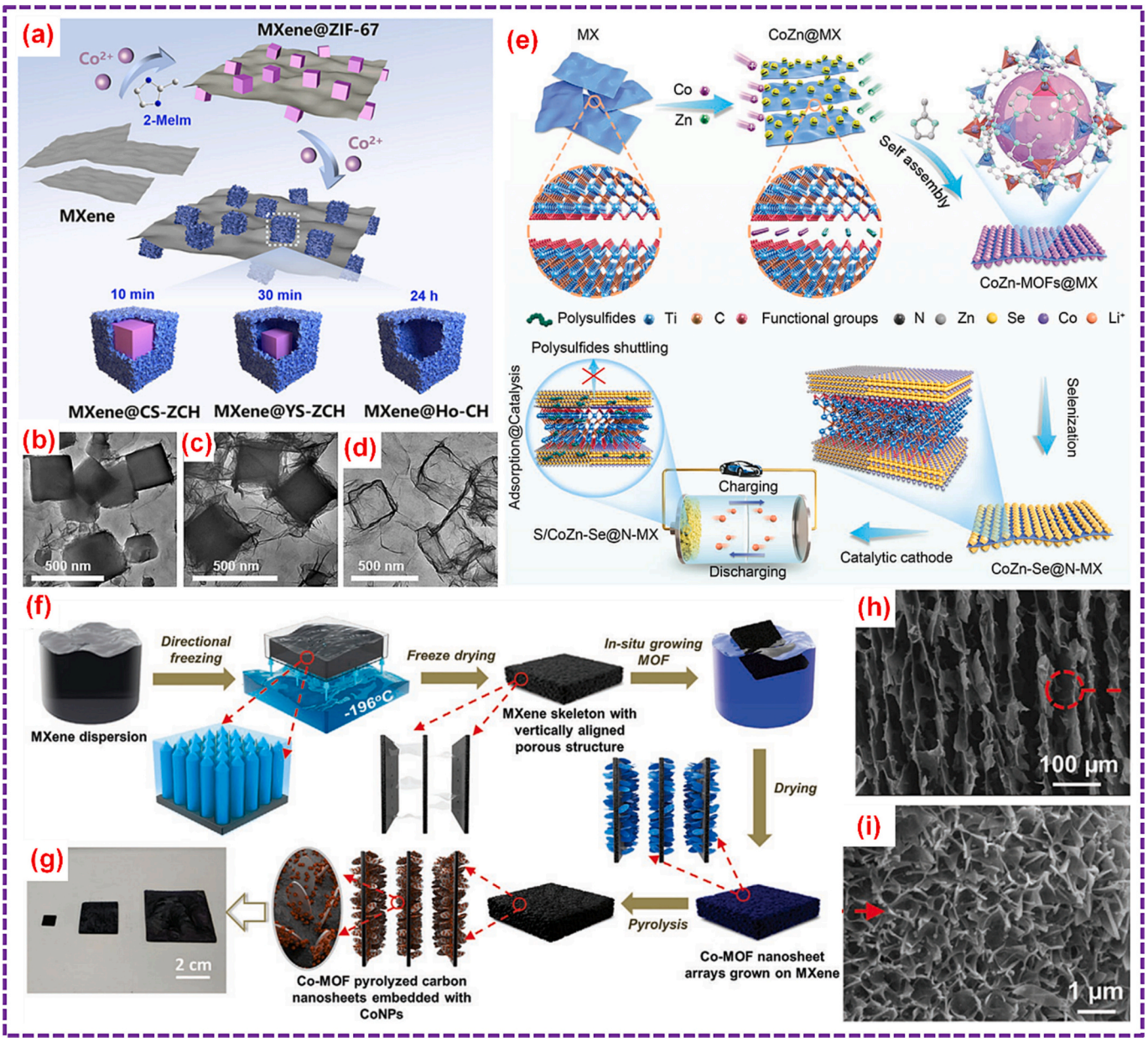

Fig. 10. (a) Pictorial representation of hierarchical ZIF-67/$Co(OH)_2$. (b-d) TEM analysis of MXene@$Co(OH)_2$. Adopted with permission from Ref. [205], Copyright 2022, The Royal Society of Chemistry. (e) Schematics of CoZn-Se@N-MX. Adopted with permission from Ref. [206], Copyright 2021, Wiley-VCH. (f) Preparation route of the Co-CNS/M foam. (g) Photograph of various sizes, and (h,i) SEM images of the as-synthesized Co-CNS/M foams. Adopted with permission from Ref. [164], Copyright 2020, Wiley-VCH.

$Ti_3C_2T_x$/CuO composites via integrating CuO derived from MOF, obtained through calcination for 5 h at 500 °C, with acid etched MXene in air. These composites were then harnessed as sensitive materials for the fabrication of a gas sensor, driven by Teflon-based friction nanogenerator (TENG), to detect indoor NH_3 [212].

Metal sulfides derived from MOF have garnered substantial interest owing to its promising attributes, including high energy density and theoretical capacity, particularly within the realm of batteries [213,214]. Nevertheless, the inherent challenges posed by the volume fluctuations and limited electron conductivity during charge and discharge mechanism result in suboptimal cycle stability and rate capability. Consequently, the amalgamation of MXenes with MOF-derived metal sulfides emerges as a strategic approach, not only effectively mitigating the aforementioned cyclic transformations but also significantly enhancing interconnectivity among metal sulfides. This augmentation curtails ion transmission pathways within the electrolyte, consequently elevating the performance of electrochemical activity. For instance, Fan and colleagues orchestrated the in-situ synthesis of $Ti_3C_2T_x$@MOF derived NiCoLDH composite via a process encompassing coprecipitation and corrosion. Through subsequent carbonization, a novel porous $Ti_3C_2T_x$@NiCoS layered structure was realized. Deployed as cathodes within zinc-air batteries, this configuration harnessed the robust coordination interaction between NiCoS and $Ti_3C_2T_x$, thereby manifesting reduced charge/discharge overpotentials and prolonged stability [215]. In a parallel endeavor, Xu's team orchestrated the coordination of ZIF-8 derived 0D ZnS nanodots with 2D MXene. This strategic combination facilitated accommodating volume alterations, ultimately yielding superior lithium storage performance characterized by remarkable stability in cycling [162].

Metal phosphides offer notable advantages, including efficient electron transfer rates, substantial surface areas, and abbreviated charge diffusion pathways [216,217]. Consequently, the amalgamation of

MXene with MOF-derived phosphides of metal presents a favorable avenue for diverse applications. In a pioneering endeavor, Yu's research team employed a molten salt route to etch the Ti_2AlN, followed by HCl strip off to produce monolayer Ti_2NT_x. This MXene was subsequently self-assembled with ZIF-67, culminating in the formation of a Ti_2NT_x@MOF CoP hybrid. The fabrication process involved decarburization in an air environment for 1 h at 450 °C, succeeded by phosphidation in an Ar atmosphere for 1.5 h at 350 °C. This composite structure synergistically optimized the electronic configuration, augmenting the overall stability [218]. Meanwhile, Sun's research group introduced a novel MXene-NPO battery type electrode. Initially, functional groups on the MXene surface were deprotonated and connected with organic linkers. Subsequent bottom-up preparation led to the creation of MXene-MOFs composites by combining metal ions with the organic linkers attached on the MXene surface. A subsequent "top-to-bottom" hydrothermal reaction with aqueous KH_2PO_4 facilitated the in-situ phosphorylation, involving the etching of amorphous Ni-MOF spheres. This process culminated in the development of an innovative electrode material with enhanced properties [180].

Further, metal selenides are highly regarded as promising anodes for LIBs/SIBs due to its remarkable specific capacity and exceptional electrochemical performance [219,220]. Nevertheless, the fluctuations in volume during the sodium (or lithium) insertion and extraction process can compromise their conductivity and stability. To surmount this challenge, the incorporation of metal selenides with MXenes, known for their robust mechanical characteristics, offers a solution [221]. In a pioneering effort, Chen's research group harnessed electrostatic interactions to combine negatively charged MXenes with positively charged Zn^{2+} and Co^{2+} ions. The introduction of 2-methylimidazole, an organic ligand, into this system resulted in the self-assembly of CoZn-MOF on the MXenes' surface. Subsequent vulcanization transformed CoZn-MOF into CoZn-Se NPs. Leveraging the organic linker, N-doping was facilitated in MXenes. This innovative process yielded CoZn-Se@N-MXene, which served as a cathode in Li—S batteries, as depicted in Fig. 10e [206].

3.2.3. Additional MXene@MOF derived compounds

Metal ions within MOFs would undergo reduction to yield metal NPs, phosphides, and oxides of metal, and more. Simultaneously, the organic linkers which serve as carbon sources would be converted to porous structures, forming composites of carbon with metal, metal oxides, and metal phosphides [222–224]. In a study led by Liang and colleagues, a MXene dispersion solution was achieved through selective etching and delamination. Consequently, MXenes featuring vertically aligned porous materials were fabricated using directional freeze-drying. In situ growth of Co-MOF on MXene was followed by the calcination in an Ar environment for 2 h at 450 °C to yield MXene foam/cobalt NPs-carbon NSs (Co CNS/MXene) as illustrated in Fig. 10f-g. The Co^{2+} within Co-MOF reduced to cobalt NPs, while organic linkers underwent transformation into amorphous carbon throughout the carbonization. SEM analysis revealed the uniform coverage of blade-like nanoplates over the MXene foam [164]. Yang research group adopted a distinct approach, initially subjecting ZIF-8 to calcination for 1 h in N_2 atmosphere at 1100 °C to produce Fe-N-C, which was then combined with MXene to generate MXene@Fe-N-C [225]. In a separate investigation, Fan's group synthesized a sandwich-type structure of $Ti_3C_2T_x$@CoP-NC through phosphidation. As depicted in Fig. 10h-i, CoP NPs were cultivated on the $Ti_3C_2T_x$ interlayer, forming a layered arrangement. The in-situ intercalation of CoP-NC into MXene layers successfully increased the spacing between $Ti_3C_2T_x$ layers, thereby creating insertion sites for Li^+ and Na^+ ions and additional diffusion paths [226].

3.3. MXene derivatives@MOF derivatives

The high conductivity and unique structure of MXenes have garnered significant interest [227,228]. However, the MXenes oxidation stability is compromised due to the exposure of numerous metal atoms [149]. Consequently, partial conversion of MXenes into metal oxides becomes a viable approach, wherein these metal oxides grow in situ on the MXene surface developing the formation of hybrid materials known as MXene/MXene-derived materials [229,230]. Swami and his group employed MXene@Co-MOF composites as precursor materials, subjecting to calcination in the N_2 atmosphere at various temperatures for 2 h. This process led to the creation of Co NC/Ti_3C_2-T hybrids, specifically Co NC/Ti_3C_2-700, Co NC/Ti_3C_2-800, and Co NC/Ti_3C_2-900 as depicted in Fig. 11a. Throughout the carbonization process, Co NPs derived from Co-MOF were deposited onto MXenes within a matrix of N-doped carbon materials as shown in Fig. 11b. Additionally, the surface of MXenes yielded TiO_2 particles as byproducts, which were confirmed via XRD analysis (Fig. 11c) [86].

As oxidation progressed, the distinct phases of MXene gradually vanished, culminating in the complete transformation into MXene derivatives [150,231]. To illustrate, Lu and colleagues harnessed microwave-assisted heating to seamlessly integrate Fe-MOFs with $Ti_3C_2T_x$ in situ, followed by high-temperature carbonization in H_2/Ar environment for 2 h at 600, 700, and 800 °C. This process yielded sandwich-structured Fe&TiO_2@C composites depicted in Fig. 11d. Fe-MOFs underwent conversion into carbon-coated Fe NPs throughout the carbonization, while MXenes underwent a transformation to TiO_2 NPs and carbon nanolayers as depicted in Fig. 11e. XRD analysis revealed a temperature-dependent evolution, with anatase TiO_2 diminishing as temperature increased, ultimately leaving behind only Fe phases and rutile TiO_2 within the composites as illustrated in Fig. 11f [169].

4. Functionalities

Undoubtedly, pure-phase MOFs exhibit certain drawbacks, notably inadequate stability, and low electronic conductivity, which substantially curtail its extensive practical application. On the other hand, MXenes present themselves as exceptional candidates for amalgamation with MOFs, capitalizing on their inherent benefits like abundant surface functional groups, expansive surface area, and impressive electronic conductivity. Astonishingly, these composite structures not only mitigate these inherent limitations such as the stability and low electronic conductivity concerns of MOFs but also introduce an array of innovative functionalities, including but not limited to the intriguing template effect. In the forthcoming chapter, an exhaustive exploration of the functionalities stemming from the synergistic interplay between these two components will be systematically elucidated and discussed.

4.1. Enhanced electron/ion transport

MXene NSs play a pivotal role in constructing a robust conductive network, profoundly enhancing the MOFs electronic conductivity [232,233]. The strategic MOFs integration within the intermediary MXenes layer serves to adeptly thwart self-stacking, thereby engendering expanded electrolyte accessibility, heightened exposure of electroactive sites, and a more extensive electron/ion transport conduit. In a study by Chen et al., they employed self-assembly to engineer a 0D—2D heterostructure named bimetallic selenides@N-doped MXene (CoZn-Se@N-MX). This ingenious architecture harnesses 0D CoZn-Se NPs to function as spacers, skillfully averting the reaggregation of N-MX NSs, thereby conserving augmented active domains for electron/ion migration [206]. Furthermore, the profusion of functional groups on MXene surfaces augments the chemical interplay between MXenes and MOFs, resulting in the reduction of electron/ion transmission pathways. Yang et al. demonstrated this effect in the construction of MXene/NiCo LDH, where Ni-ion-exchanged ZIF-67 was anchored onto MXene NSs. The robust chemical bonding between MXene's and MOFs surface functional groups accelerates the diffusion of ions and heightens the transfer of charge rates [234]. The augmentation of transfer of electron/ion rates in

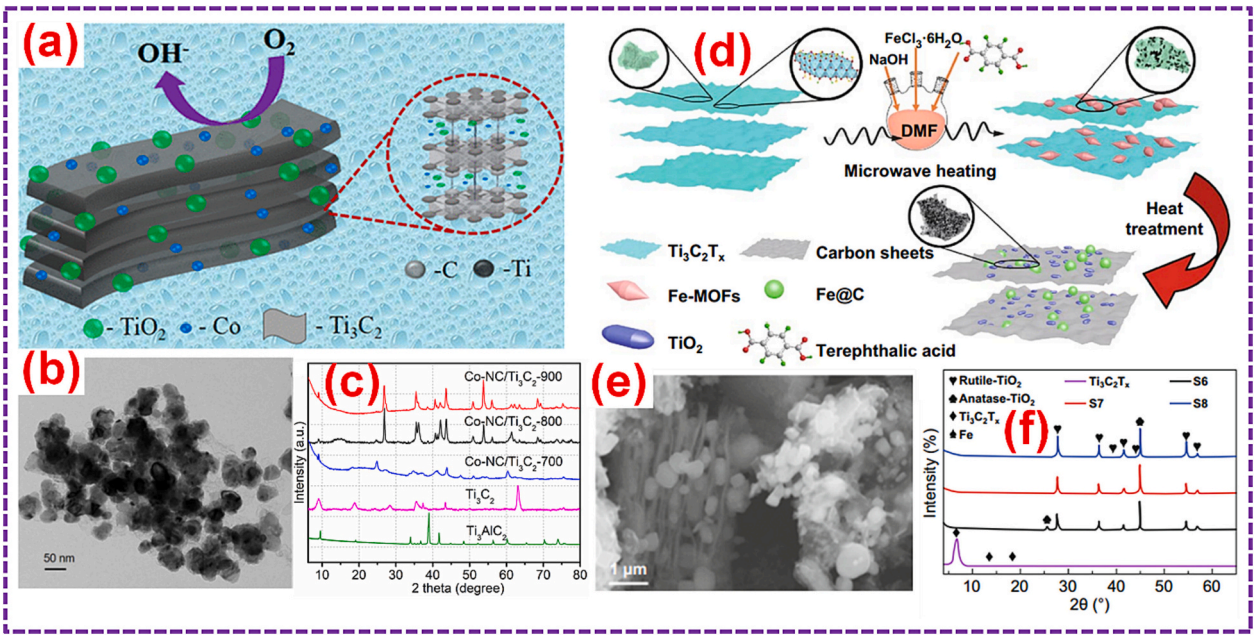

Fig. 11. (a) Pictorial representation of Ti_3C_2@Co-NC. (b) TEM analysis of the Co-NC/Ti_3C_2-800. (c) XRD analysis. Adopted with permission from Ref. [86], Copyright 2021, The American Chemical Society. (d) Schematics of the Fe&TiO_2@C. (e) SEM analysis of $Ti_3C_2T_x$-Fe-MOF. (f) XRD analysis. Adopted with permission from Ref. [169], Copyright 2020, Springer.

MXene@MOF based composites finds validation through rigorous DFT analog computational analyses. This methodology, as exemplified by Xu and colleagues, involved the construction of four distinct models to comprehensively elucidate the MXene's role (Fig. 12a). The interaction at the MXene and ZnS interface exhibited robust bonding (Fig. 12b), facilitating the transfer of electrons from the electron-abundant region of $Ti_3C_2T_x$ to the electron-deficient zone of ZnS. Moreover, the heterogeneous ZnS/MXene interface demonstrated a notably low diffusion barrier, enabling swift lithium migration and favorable diffusion dynamics compared to ZnS alone (Fig. 12c-e) [162]. In another instance, Zhu et al. prepared layered MXene structure integrated with MOF-derived CoFe-LDH (Fig. 12f, g) displaying remarkable oxygen evolution reaction (OER) activity. DFT analysis revealed electron migration from the layer of CoFe-LDH to the layer of O-terminal $Ti_3C_2O_2$ MXene. This interface, CoFe-LDH/$Ti_3C_2O_2$, exhibited a diminished energy barrier in contrast to CoFe-LDH, attributed to the weak adsorption of intermediates. The existence of Ti_3C_2 MXene effectively modified the electronic structure, thereby enhancing OER performance (Fig. 12h-k) [235].

4.2. Improve stabilities

Certain MOFs are best by inherent instability, a constraint that hampers their practical utility [236,237]. However, the judicious amalgamation of MOFs and MXenes through strategic design can give rise to a synergistic effect that enhances overall stability. An illustrative example is provided by Cheng and co-researchers, who devised a method to engineer hierarchical 3D interconnected porous Ti_3C_2/NiCo-MOF composites via vacuum based filtration, thereby bolstering Li-ion storage through robust hydrogen bonds between Ti_3C_2 and NiCo-MOF for heightened structural durability [160]. In a similar vein, Wang and colleagues engineered a 2D $Ti_3C_2T_x$/NiCo-MOF composite structure fortified with lignin's. In this innovative preparation, antioxidant-rich lignin particles were ingeniously leveraged to bind the carboxyl group within the organic linker, the terminal group on the $Ti_3C_2T_x$ surface and the hydroxyl group in lignin, thereby establishing a steadfast heterojunction interface. This strategy effectively curtailed MXene oxidation and engendered enhanced structural stability (Fig. 13a, b) [238]. The optimized 2D/2D $Ti_3C_2T_x$/NiCo-MOF heterostructure anode demonstrates a high capacity of 637 mAh g^{-1} at 0.2 A g^{-1} after 200 cycles. Furthermore, the Li^+ intercalation/extraction mechanism of the $Ti_3C_2T_x$/NiCo-MOF heterostructure electrode is explored in detail.

The augmented structural stability exhibited by MXene@MOF based composites serves to effectively avert deformations in the structure of electrode during the absorption/desorption of Li- ions, thus significantly elevating cycle stability. An exemplar of this concept is elucidated by Wong and collaborators, who introduced a 2D sandwiched Cu-HHTP/MX heterojunction as a cathode for ZIBs. Characterized by their varying stacked configuration, this material boasted ample active sites and exceptional structural integrity. Electrochemical assessments underscored the remarkable rate performance characteristics of Cu-HHTP/MX (260.1 mA h g^{-1} at 0.1 A g^{-1} and 173.1 mA h g^{-1} at 4 A g^{-1}) alongside its enduring cycle stability of 92.5 % at 4 A g^{-1} over 1000 cycles [191]. Another illustrative case is presented by Sun et al., who embarked on the electrostatic assembly of MXene and LDH NSs derived from ZIF, followed by annealing to yield MXene@metal oxide (MXene@CoO/$Co_2Mo_3O_8$) composites (Fig. 13c). This unique configuration endowed the metal oxides with a 3D robust conductive network through the coating of MXenes on their surface. This network efficiently mitigated the structural deformation during the absorption/desorption of Li ions, thereby substantially heightening cycle stability (Fig. 13d-e) [82]. Similarly, Li and colleagues orchestrated the fabrication of porous $ZnCo_2O_4$@Ti_3C_2 core-shell heterostructures, arising from MXene/ZIF-8@ZIF-67 composites, for utilization as a immobilizer of sulfur in LSBs. The introduction of Ti_3C_2 conferred accelerated electron/ion transport rates and proficiently immobilized intermediate LiPSs products via physicochemical adsorption, thus addressing volume fluctuation concerns and ensuring stable high-capacity Li-ion storage. Notably, Ti_3C_2@$ZnCo_2O_4$/S displayed an impressive discharge capacity of 1283.9 mA h g^{-1}, coupled with a coulombic efficiency of 98.7 % at 0.1C rate [239].

4.3. Effect of template

The term “effect of template” pertains to the phenomenon where the coordination of ligands and templates induces changes in electronic

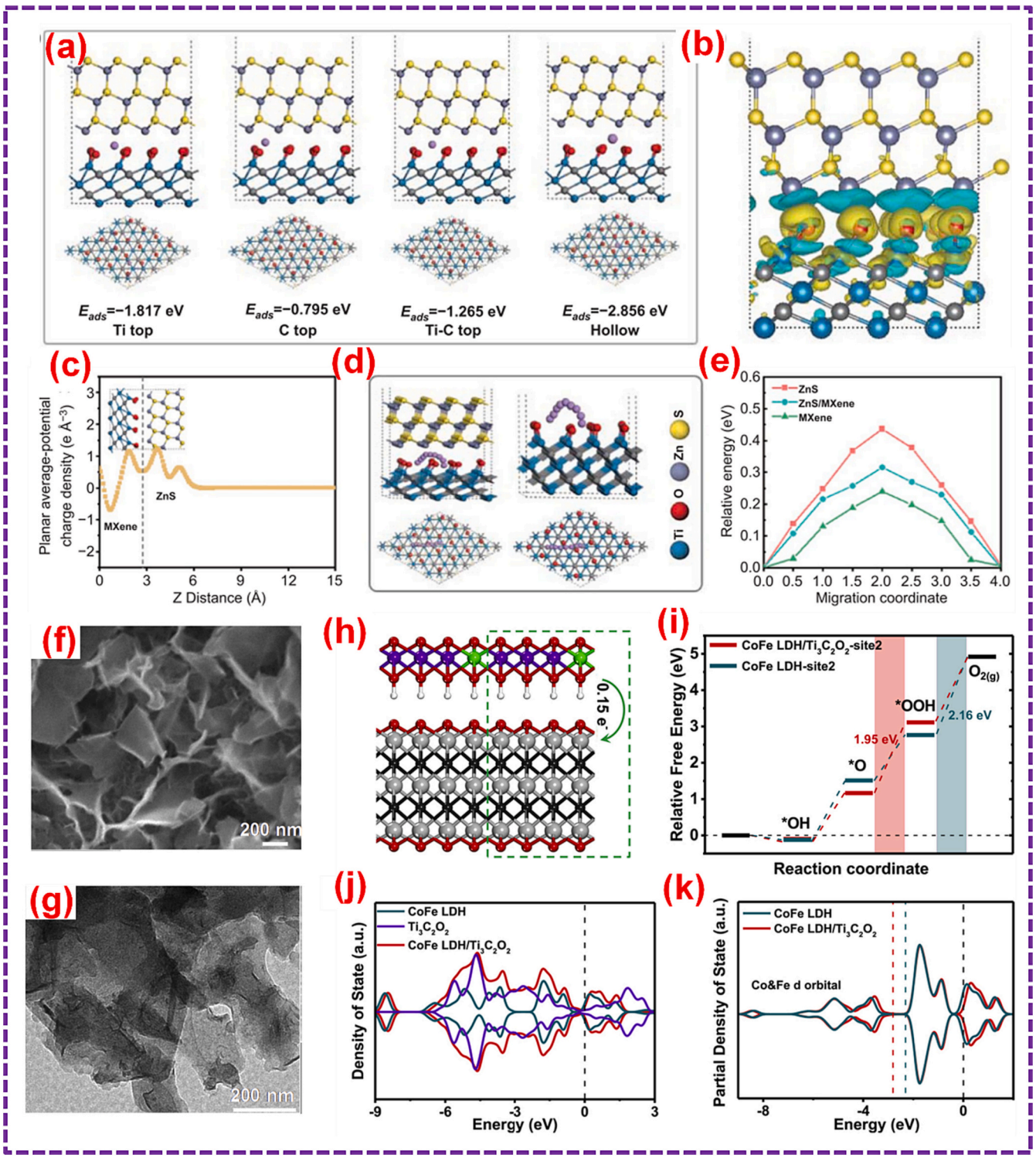

Fig. 12. Theoretical simulation of $Ti_3C_2T_x$-ZnS. (a) adsorption energy of Li^+ and (b) differences in charge density. (c) Planar average potential charge density. (d) diffusion pathway of Li^+ and (e) the difference in diffusion energy. Adopted with permission from Ref. [162], Copyright 2021, Springer. (f) SEM image of Ti_3C_2@CoFe MLDH and (g) TEM analysis of Ti_3C_2@CoFe MLDH. (h) Cross sectional image of the optimized $Ti_3C_2O_2$@CoFe LDH. (i) Diagrams of free energy at 0 V for the OER activities. (j) DOS. (k) PDOS. Adopted with permission from Ref. [235], Copyright 2021, Elsevier B.V.

states and imparts specific spatial configurations. Templates can encompass a spectrum of entities, including surfactants, organic-inorganic hybrids, organic molecules, polymers, inorganic molecules, and more [240]. In this context, the focus is on MXenes as the subject of study. Following HF treatment, MXenes exhibit a profusion of terminal functional groups like OH^-, O^-, F^-, enabling interactions with MOF precursors via weak forces such as hydrogen bonding, electrostatic attraction, etc., leading to the formation of distinctive structural fragments. Throughout this synthetic method, MXenes would serve as agents guiding structural formation or controlling size. By modulating the quantity of MXenes, MOF structures with diverse dimensions and morphologies would be achieved. This captivating interplay has captivated

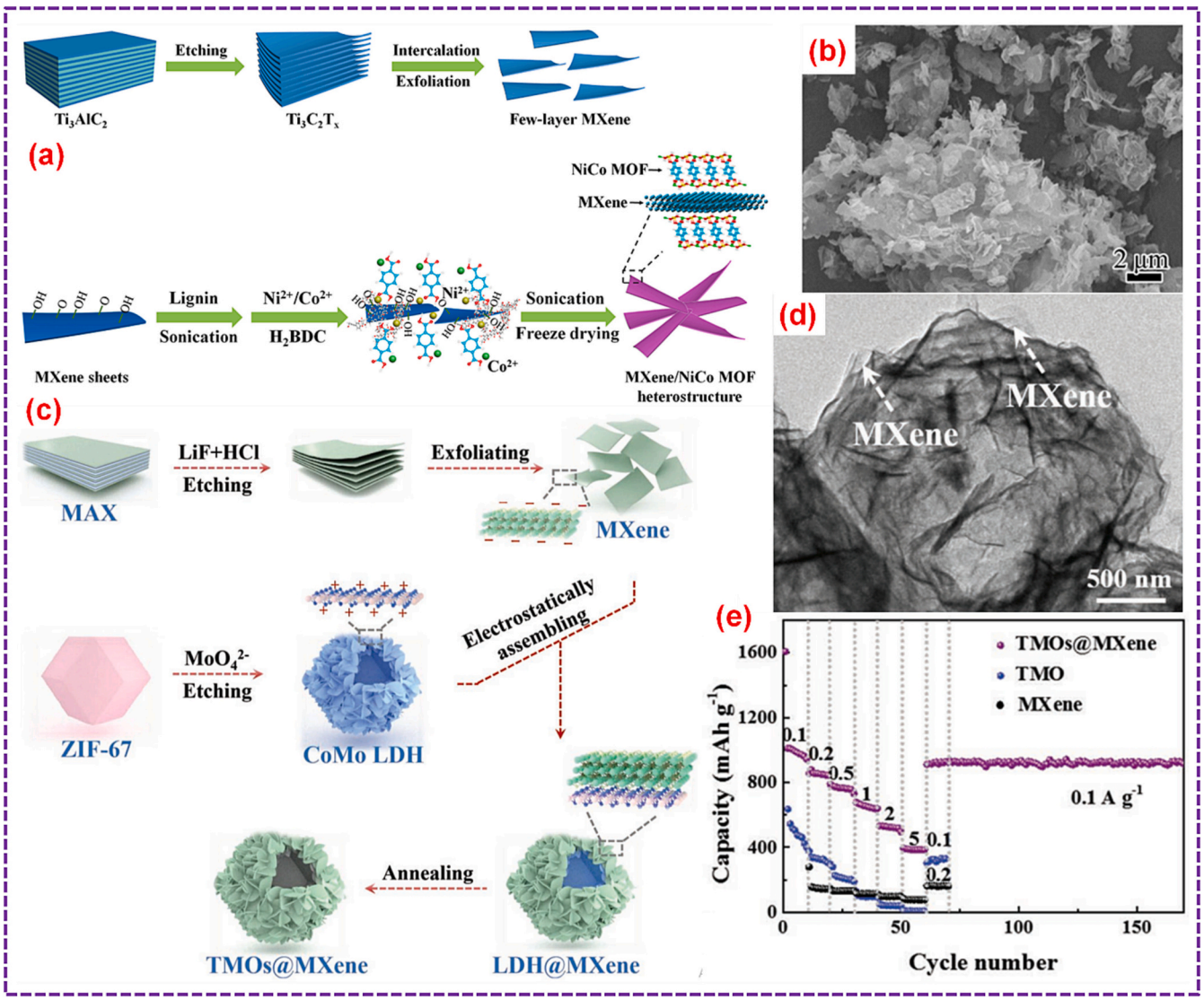

Fig. 13. (a) Pictorial representation of MXene@NiCo-MOF, (b) SEM image of MXene@NiCo-MOF. Adopted with permission from Ref. [238], Copyright 2022, Elsevier B.V. (c) Preparation of CoO/$Co_2Mo_3O_8$@MXene. (d) TEM analysis of CoO/$Co_2Mo_3O_8$@MXene, (e) Rate capabilities. Adopted with permission from Ref. [82], Copyright 2019, Wiley-VCH.

researchers due to its potential to profoundly influence the performance and downstream applications of MOFs [241,242]. Consequently, there exists the prospect of harnessing these effects to tailor and fabricate advanced MXene@MOF composites, thereby expanding their utility across various domains [243,244].

4.3.1. Change in morphology

MXenes exhibits the capability to alter the MOFs morphology. Zhang and colleagues achieved the synthesis of $CoNi_2S_4$ dendrites under the influence of Ti_3C_2 via solvothermal approach (Fig. 14a). When the MXene solution was omitted and the vulcanization process extended till 6 h, Ni-Co-S/NF manifested a coarse NSs-like morphology, with numerous NPs accumulating on its surface (Fig. 14b). The introduction of MXene suspension brought about remarkable morphological transformations. As depicted in Fig. 14c, a distinctive dendritic architecture emerged, with each dendrite resembling a tree composed of a central trunk and delicate branches. Furthermore, the MXene NSs were observed to envelop the upper portions of these branches. The formation of this dendritic structure was accredited to the MXenes presence, which facilitated the hydrolysis and subsequent recombination [245]. Mi and his collaborators documented that MXene played a pivotal function in steering the Ni-MOF micro stripes assembly (Fig. 14d). In the MXene absence, Ni-MOF developed into an independent 2D nanosheet structure (Fig. 14e). The inclusion of MXenes led to a significant reduction in agglomeration and facilitated the formation of a layered microstrip structure (Fig. 14f) [246].

Additionally, the incorporation of Ti_3C_2 NSs could potentially result in the formation of supplementary TiO_2 at the interface of MXenes and MOFs [88]. This "MXene-TiO_2" interface structure notably enhanced electron transfer at the interfaces, thereby improving overall performance [247,248]. Li and his team synthesized Ti_3C_2-modulated MIL-125-NH_2-based dual-heterojunction materials through a hydrothermal approach (Fig. 15a) [88]. Upon the introduction of MXenes at varying concentrations ranging from 0, 0.1, 1, and 5 wt% denoted as MT0, MT0.1, MT1, and MT5, distinct morphological transitions were observed in the resulting samples. TEM analysis of MT0 showcased plate-type NSs, while MT0.1 exhibited primarily rod-type NPs. In contrast, MT1 and MT5 displayed improved particle sizes, featuring uniform coatings of TiO_2 NSs and NPs, respectively. This phenomenon further directed the influence of Ti_3C_2 addition on the crystallization of NH_2-MIL-125(Ti) composites (Fig. 15b-f) [88]. The optimized NH_2-MIL-125(Ti)(TiO_2)/Ti_3C_2 nanohybrids yielded 1.65 times higher H_2O_2 production rate and

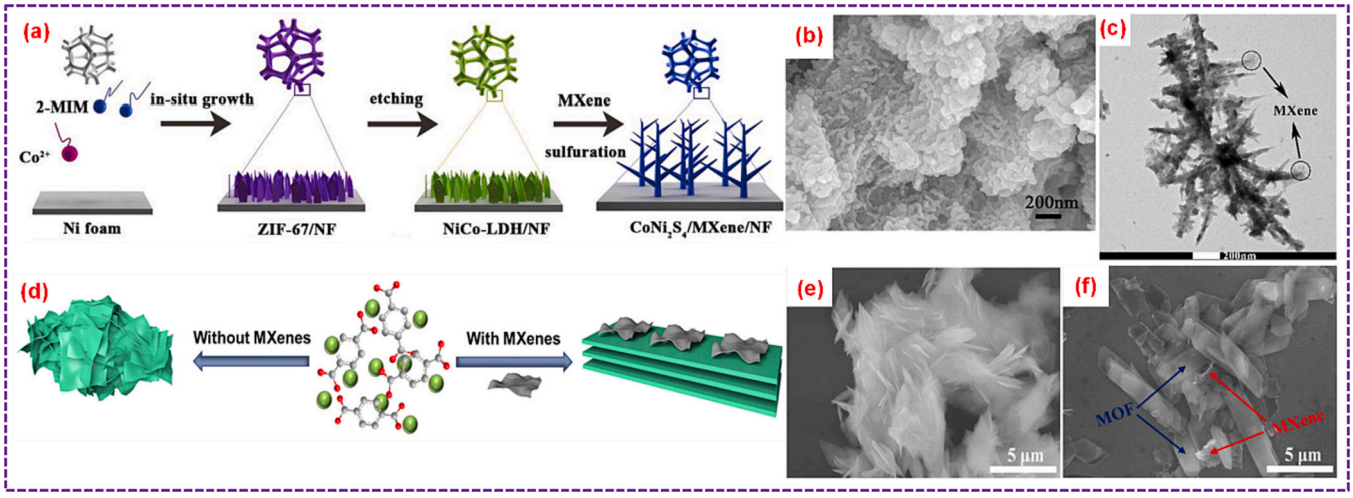

Fig. 14. (a) Pictorial representation of MXene@$CoNi_2S_4$/NF. (b) SEM analysis of Ni-Co-S/NF. (c) TEM image of MXene@$CoNi_2S_4$/NF. Adopted with permission from Ref. [245], Copyright 2021, Elsevier B.V. (d) Scheme for the formulation of Ni-MOFs and $Ti_3C_2T_x$/Ni-MOFs. (e) SEM analysis of Ni-MOFs, (f) SEM image of $Ti_3C_2T_x$/Ni-MOFs. Adopted with permission from Ref. [246], Copyright 2021, Elsevier B.V.

11.5 times higher tetracycline hydrochloride (TC-HCl) degradation efficiency than that of the pristine MIL-125-NH_2 under visible light irradiation ($\lambda > 420$ nm).

4.3.2. Change of size

The constrained interlayer distances of MXenes portray a major role in restricting the uncontrolled expansion of MOFs between these layers, thereby enabling effective control over the size of MOFs. As an illustration, Sun and colleagues developed MXene@NiP composite through the in-situ transition of MXene@Ni-MOF (Fig. 15g). In Fig. 15(h, i), the NPO spheres derived from MOFs acted as pillars, intercalating into the MXene interlayers. Simultaneously, the confined MXene interlayer spacing restricted the growth of these MOF spheres, resulting in NPO spheres with a diameter of approximately 20 nm. In contrast, the MOF-derived NPO spheres in the absence of MXenes shown in Fig. 15j, k displayed a larger sphere diameter of about 200 nm, highlighting that the "confinement effect" induced significant reduction in the size of MOF precursors. Notably, this effect also contributed to the enlargement of surface area and pore volume of MOFs [180]. The MXene@NiP composite material displays a high specific capacity of 639C g^{-1} at 0.5 A g^{-1} and outstanding cycling stability of 85 % capacity retention after 10,000 cycles.

4.4. Prevention of agglomeration

Agglomeration directs the depletion of active sites, significantly impairing electrochemical performance. Consequently, the synergistic effect between MXenes and MOFs, when combined, becomes pivotal as it effectively prevents agglomeration and substantially enhances material conductivity. An exemplary instance of this synergy is demonstrated in the work of Pang's research group, who engineered a distinctive Ti_3C_2@[Ni(thiophene-2,5-dicarboxylate) (4,4′-bipyridine)] $_n$ (MXene@Ni-MOF) layered column structure (Fig. 16a, b). Notably, the unique architecture of Ni-Bpy linear chains induced the growth of Ni-MOF crystals along the (202) crystal plane, while the Ni-Tdc network structure facilitated the growth of Ni MOF crystals along the (024) crystal plane. This design effectively averted MOF and MXene agglomeration (Fig. 16c-e) [154]. In a similar vein, Wang and colleagues achieved the in-situ synthesis of MXene/ZIF-67 nanoboxes derived hierarchical MXene/$CoSe_2$/Ni_3Se_4 composites, tailored for supercapacitor applications. This unique nanostructure ensured vertical anchoring of $CoSe_2$/Ni_3Se_4 onto MXene NSs, effectively mitigating the undesired MOF-derived $CoSe_2$/Ni_3Se_4 self-polymerization and impeding the MXene NSs re-stacking [103].

4.5. Additional functionalities

4.5.1. Supports embedded pseudocapacitance

Intercalated pseudo capacitance achieved through rapid ion diffusion and redox reactions within bulk materials, is a distinctive characteristic [249,250]. MXenes with their high conductivity, and robust current charge leverage a stacked layered configuration that facilitates swift electrolyte ion traversal and an active surface primed for reversible redox reactions, thereby fostering intercalated pseudocapacitance [251]. In a study by Yang and his group, NiCo-ZIF-67 was anchored through chemical bonds onto the MXene surfaces, augmenting the availability of effective active sites. Notably, among the assessed materials, MXene/NiCoZDH exhibited the highest capacitance, underscoring the capacity-enhancing role of MXene introduction [234]. Meanwhile, Wang et al. explored the influence of a $Ti_3C_2T_x$ intercalated pseudocapacitor on a Co-MOF binder-less electrode. The fusion of Co-MOF with MXene established an expedited and efficient pathway for redox activities (Fig. 16f). Moreover, the inherent multilayer porous structure of MXenes promoted ion intercalation. The Co-MOF/$Ti_3C_2T_x$@NF showcased a superior maximum current density and total area compared to bare Co-MOF@NF. Additionally, the discharge duration of Co-MOF/$Ti_3C_2T_x$@NF surpassed that of bare Co-MOF@Ni, attributed in part to the embedded pseudocapacitance from $Ti_3C_2T_x$ (Fig. 16g-j) [157].

4.5.2. Encourage the photogenerated electrons and holes separation

The fast electron-hole pairs recombination produced via photocatalysts can severely undermine the performance of photocatalytic activity. MXenes facilitate the spontaneous migration of photogenerated electrons due to low fermi level, thereby achieving Fermi level equilibrium [252,253]. Furthermore, MXenes robust electron interaction enhances the efficiency of photogenerated electron-hole separation. Consequently, MXenes emerge as exceptional photocatalysts for enhancing the MOF-modified photocatalysis activity. Deng and colleagues effectively synthesized Co—Co LDH/$Ti_3C_2T_x$ composites using an in-situ derivatization approach (Fig. 17a). The incorporation of $Ti_3C_2T_x$ markedly expedited the holes and electrons separation and transfer, leveraging the swift dissociation rate of electron-hole pairs within the layered nanoarray connections (Fig. 17b-d) [254]. Similarly, Liu et al. designed 2D/2D Ti_3C_2/Co-ZIF-9 composites through electrostatic self-assembly, harnessed for photocatalytic water splitting. In this context, excited electrons from Co-ZIF-9's highest occupied molecular

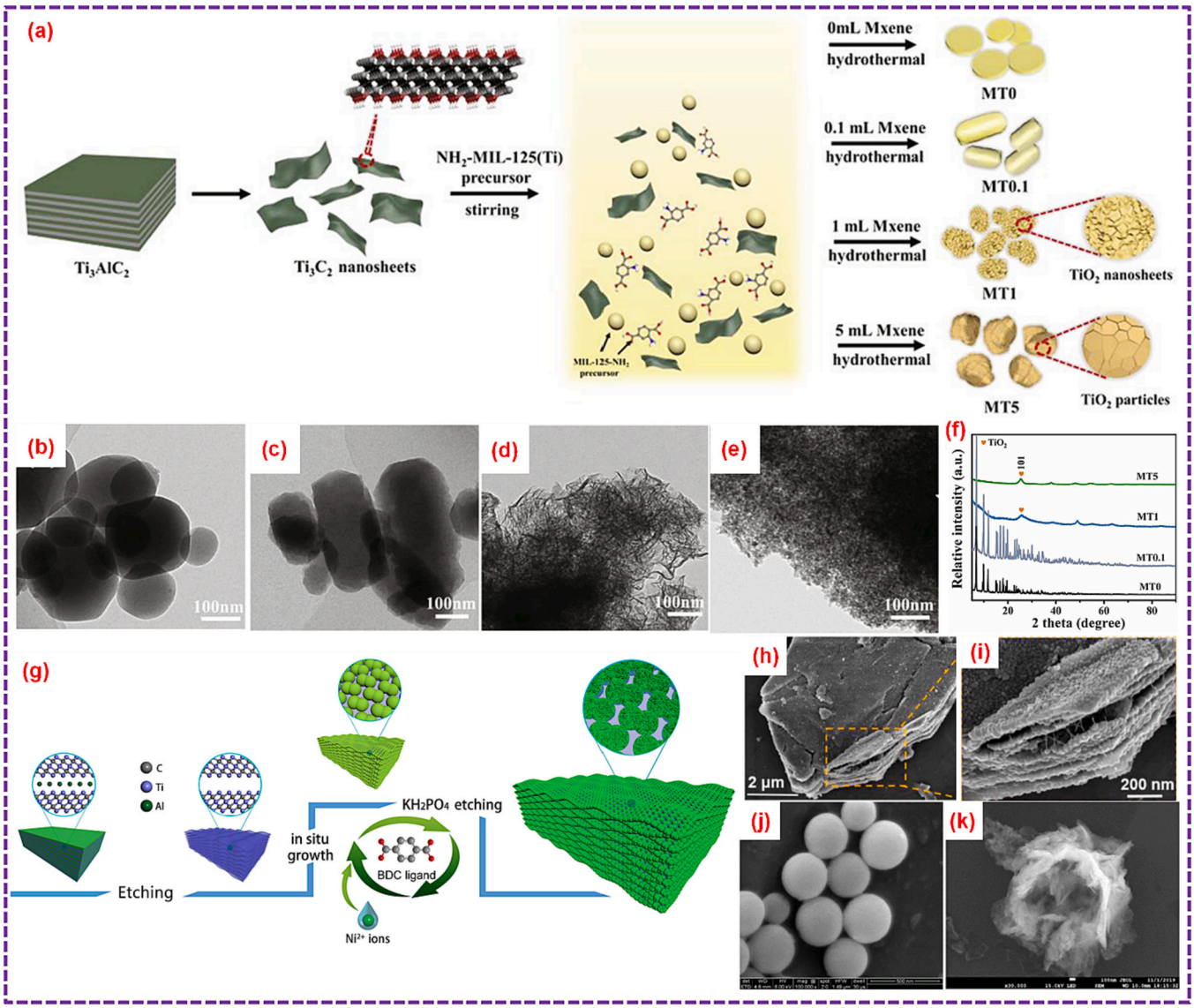

Fig. 15. (a) Scheme for the preparation of Ti_3C_2 and MOFs related architectures. TEM analysis of (b) MT0, (c) MT0.1, (d) MT1 and (e) MT5. (f) XRD pattern. Adopted with permission from Ref. [88], Copyright 2020, Elsevier B.V. (g) Pictorial interpretation of MXene-NPO. SEM images of (h,i) MXene-NPO, (j) Ni MOF and (k) NPO, respectively. Adopted with permission from Ref. [180], Copyright 2021, Elsevier B.V.

orbital (HOMO, 1.51 V) transitioned to its lowest unoccupied molecular orbital (LUMO, −0.47 V). Given that the Fermi energy level of metal Ti_3C_2 (0.71 V vs. NHE, pH = 7) was considerably lower than that of Co-ZIF-9, photoexcited electrons readily flowed from Co-ZIF-9 LUMO to Ti_3C_2. Subsequently, they reacted with H^+ to yield H_2. Photoluminescence, photocurrent, and electrochemical impedance spectroscopy (EIS) analyses corroborated the high capacity of the composites to separate and transfer photogenerated electrons and holes, translating to elevated photocatalytic efficiency (Fig. 17e-h) [187].

5. Electrochemical applications

As mentioned earlier, the combination of MXene and MOF brings forth a range of advantages, including notable porosity, enhanced electro-conductivity, multiple active sites, and improved structural stability. These attributes make them promising contenders for advancing energy storage and conversion devices with tailored characteristics. Moreover, the controlled chemical composition, hierarchical architectures, and synergistic effects of MXene@MOF-derived hybrids can further enhance their performance. In the subsequent section, our focus primarily centers on the utilization of MXene@MOF hybrids and their derived materials in the realms of SCs, rechargeable batteries, and electrocatalysis.

5.1. Supercapacitors

Among the array of energy storage devices, SCs stand out as particularly promising, thanks to their exceptional attributes like high power density, swift charge/discharge kinetics, and sustained cycle life [255]. The recent advancements of MXene@MOF hybrids and their derived materials for SCs are summarized in Table 3. The subsequent sections will delve into specific cases to elaborate on these developments.

5.1.1. MXene@MOF composites

The growing demand for portability has raised stringent expectations for prolonged stability and mechanical adaptability in various electronic devices. Among these, the fiber-shaped electrochemical supercapacitor (FESC) has emerged as a highly promising solution, characterized by its lightweight construction, remarkable flexibility, and exceptional stability [273]. However, their widespread application has been curtailed

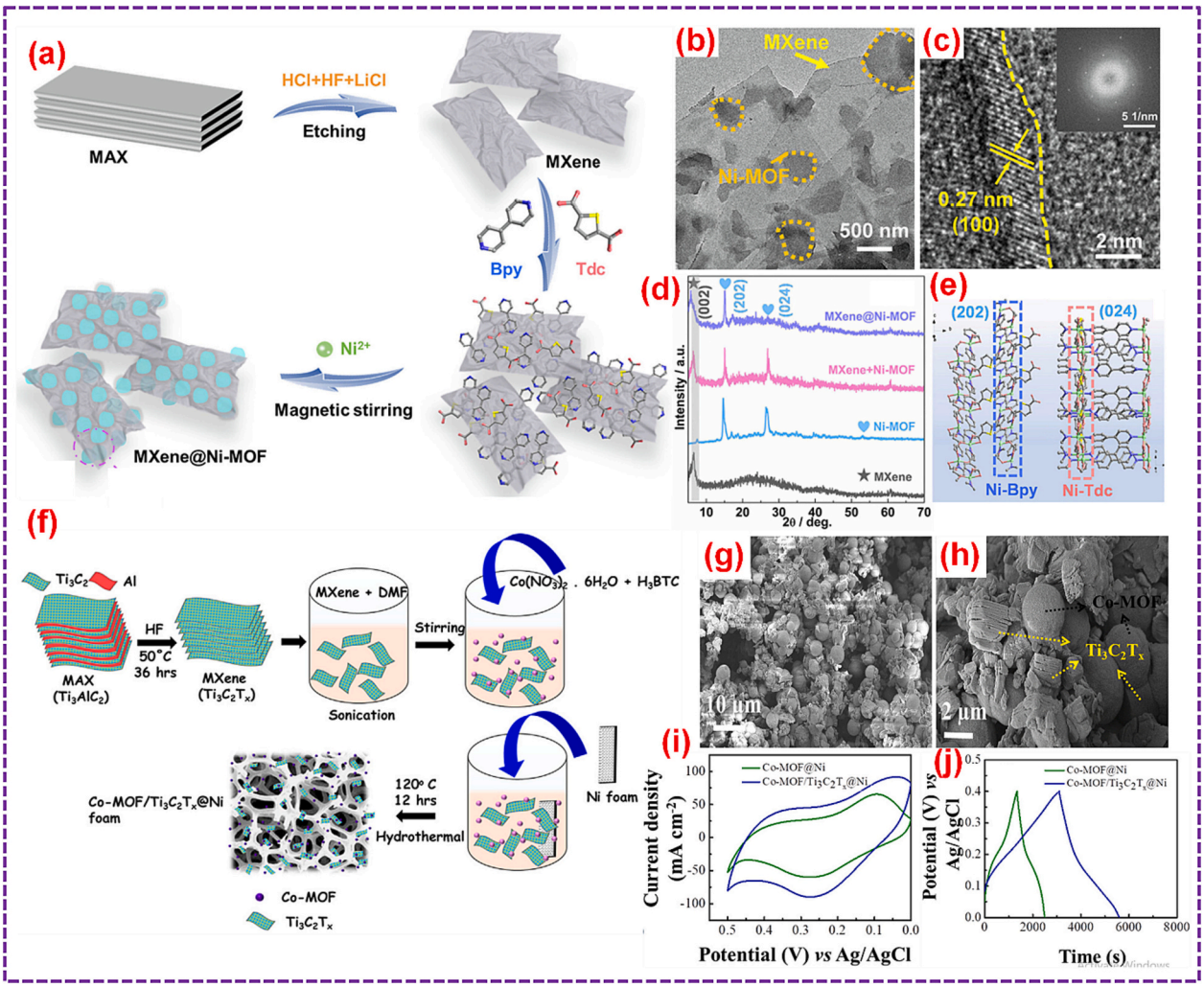

Fig. 16. (a) Scheme for the preparation of MXene@Ni-MOF. (b) TEM image, (c) HR-TEM image, and (d) XRD pattern of MXene@Ni-MOF. (e) The growth of Ni-MOF viewed along the (202) and (024) direction. Adopted with permission from Ref. [154], Copyright 2022, Elsevier B.V. (f) Pictorial representation, and (g, h) SEM images of Co-MOF/$Ti_3C_2T_x$@Ni composite. (i) CV plots, and (j) GCD analysis of Co-MOF@Ni and Co-MOF/$Ti_3C_2T_x$@Ni composite. Adopted with permission from Ref. [157], Copyright 2018, Elsevier B.V.

by their relatively low energy densities. To address this limitation, the development of advanced fiber electrodes with well-defined transport pathways, elevated electrical conductivity, and abundant active sites becomes paramount, enabling swift ion/electron movement and storage dynamics. Notably, the intermolecular forces or bonds inherent in MXene-MOF interactions play a pivotal role in enhancing charge transfer rates and reaction kinetics. In this context, Wu, and colleagues [259] pioneered the hierarchical-ordered ZIF-L(Zn)@$Ti_3C_2T_x$ MXene fibers fabrication for fiber-shaped electrochemical SCs (FESCs), showcasing exceptional specific capacitance and energy density. The process involved microfluidic techniques, resulting in MXene fibers characterized by precise alignment and anisotropic microstructure, as depicted in Fig. 18a. Importantly, the incorporation of CNTs and Mg^{2+} significantly bolstered the interlayer bonding among the NSs, enhancing mechanical robustness and electrical conductivity of the extruded fibers. These compact MXene fibers were then utilized as conductive substrates for the in-situ growth of ZIF-L(Zn) nanoarrays. The resultant ZIF-L (Zn) @$Ti_3C_2T_x$ hybrid exhibited interconnected frameworks, as shown in Fig. 18b, c offering abundant porous surfaces and efficient ionic pathways. The formation of Ti-O-Zn/Ti-F-Zn bonds at the interface between ZIF-L (Zn) and $Ti_3C_2T_x$ facilitated seamless electron and ion transfer, as depicted in Fig. 18d. The amalgamation of well-considered structure, abundant ion-accessible conduits, high conductivity, and robust interfacial chemical bonds endowed the ZIF-L (Zn)@$Ti_3C_2T_x$ fiber with significantly elevated capacitance compared to the $Ti_3C_2T_x$ fiber alone, as demonstrated in Fig. 18e. Remarkably, this engineered FESC exhibited an ultralong cyclic stability, maintaining its performance over an impressive 20,000 cycles, as illustrated in Fig. 18f.

In the realm of wearable and portable energy storage devices, flexible all-solid-state supercapacitors have garnered considerable interest [274]. A notable advancement in this domain is the development of a flexible freestanding electrode, formed through an alternating stacking of "MPFs-to-MXene-to-MPFs" conductive network. This electrode configuration was explored for flexible solid-state symmetric SCs [192]. The engineered MXene/MPFs heterostructure exhibited enhanced interlayer spacing among MXene and MPFs, facilitating the efficient transport of ions and electrolytes. Moreover, the hydrogen bond linkage among MXene and MPFs imparted chemical stability and mitigated volume variations during rapid charge/discharge cycles. This novel design was then translated into ultrathin MXene/MPF films, characterized by remarkable flexibility, which were integrated into an all-solid-state symmetric supercapacitor. Impressively, this supercapacitor showcased a remarkable energy density of 20.4 µWh cm^{-2} at a power density of 152.2 µW cm^{-2}, coupled with exceptional retention in capacity over 7000 cycles. Conventional asymmetric SCs (ASCs) have also contributed significantly to the advancement of energy storage

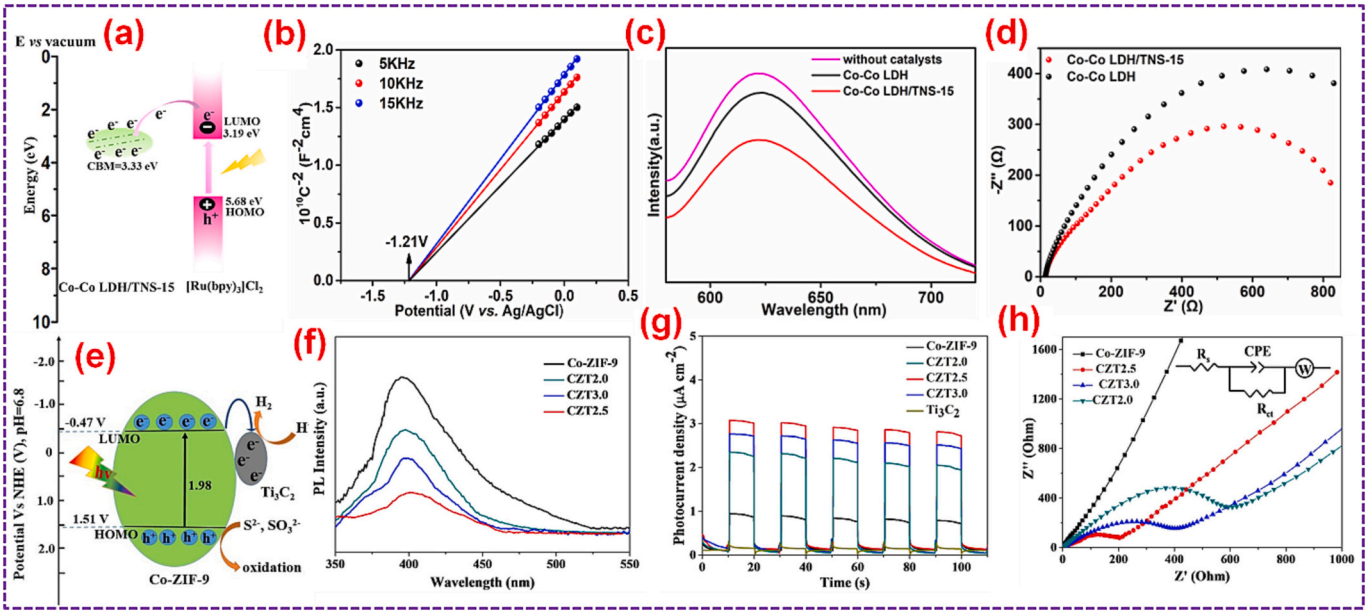

Fig. 17. (a) Proposed energy-level diagram. (b) Mott-Schottky image of Co—Co LDH/TNS-15. (c) PL spectra (d) Nyquist plot. Adopted with permission from Ref. [81], Copyright 2020, Elsevier B.V. (e) Mechanism of photocatalytic evolution of H_2 for the Co-ZIF-9/Ti_3C_2. (f) PL spectrum, (g) transient photocurrents and (h) EIS. Adopted with permission from Ref. [187], Copyright 2022, Wiley-VCH.

[275,276]. To enhance the performance of ASCs, a porous Ni-based MOF $[Ni(Tdc)(Bpy)]_n$, known for its structural stability, was synergistically combined with MXene to create a 3D porous architecture [154]. Through this integration, the interlayer spacing within MXene was substantially expanded, resulting in accelerated ion transport. The charge/discharge mechanism of MXene@Ni-MOF, as depicted in Fig. 19a, showcased impressive cycling stability, attributed in part to the existence of stable Ni-Bpy linear chain. Furthermore, the electrochemical activity of MXene@Ni-MOF significantly outperformed pristine MOF, MXene, and MXene+Ni-MOF, as demonstrated in Fig. 19b. The ASC device assembled using the MXene@Ni-MOF electrode exhibited extraordinary cycle life, retaining 98 % of its capacitance after 5000 cycles (Fig. 19c).

Another notable advancement involved the incorporation of 2D Ni-MOF belt, utilizing BDC as organic linkers, with MXene. The resulting $Ti_3C_2T_x$/Ni-MOFs hybrid demonstrated enhanced electrochemical performance in comparison to as synthesized Ni-MOFs [246]. Utilizing bimetallic MOFs possessing robust redox activity, which promotes swift Faradaic capacitance redox reactions, a composite material was developed by incorporating aminated MXene, leading to the formation of Ni/Co-MOF@$Ti_3C_2T_x$-NH_2. This composite material was engineered for the creation of SCs characterized by exceptional stability [257]. The synthesis activity of the Ni/Co-MOF@$Ti_3C_2T_x$-NH_2 is depicted in Fig. 20a, wherein Ni^{2+} and Co^{2+} ions were interconnected with $Ti_3C_2T_x$-NH_2 NSs, followed by coordination with 1,4-dicarboxybenzene (PTA) during a hydrothermal procedure. The presence of TCT-NH_2 offered numerous nucleation sites, facilitating the uniform MOF NPs growth. Leveraging the conductive MXene network ensured an ample supply of Ni and Co redox-active species, resulting in swift redox reaction kinetics, as demonstrated in Fig. 20b. Notably, the Ni/Co-MOF@TCT-NH_2 electrode showcased exceptional cyclic stability, and the assembled ASC device based on this electrode achieved an impressive coulombic efficiency (CE) retention rate of 99.3 % even after 15,000 cycles. To mitigate potential drawbacks arising from the existence of $^{-}$OH, $^{=}$O, and F functional groups on MXene surfaces, which can adversely affect structural stability and diminish electronic and electrochemical properties, Jia et al. [258] devised an innovative approach. Instead of employing acid etching methods, they opted for the molten-salt etching technique to create a Ti_3FeC_2 phase. This phase was subsequently transformed into a MIL-100(Fe)/Ti_3C_2 hybrid, intended for use as a high-energy-density supercapacitor electrode (Fig. 20c). By incorporating numerous MOF NPs onto the MXene, they maximized the exposure of redox reaction sites, facilitating swift charge and discharge cycles. In comparison to the individual MIL-100(Fe) and Ti_3C_2 components, the MIL-100(Fe)/Ti_3C_2 electrode demonstrated a notably energy density of 85.53 Wh kg^{-1} at 200 W kg^{-1}. Furthermore, the resulting electrode exhibited an exceptional capacity of 962.17 F g^{-1} at 0.5 A g^{-1} and high-capacity retention rate of 93 % even after undergoing 10,000 cycles (Fig. 20d).

5.1.2. *MXene@MOF derived composites*

To enhance the electrochemical performance of MXene@MOF composites, numerous strategies have been explored to prepare these composites. For instance, a composite of Nickel-Benzenedicarboxylate and V_2CT_x (Vanadium Carbide MXene) was fabricated on a nickel foam substrate and subjected to low-temperature annealing (150 to 380 °C) for the development of high-energy-density SCs (Fig. 21a) [211]. The elevated Ni-BDC/MXene/NF-300 exhibited a uniform NR structure characterized by high porosity (Fig. 21b). The establishment of Ni-O-V bonds at the interfaces of Ni-MOF and V_2CT_x facilitated a desired electronic structure, thereby enhancing electrical conductivity and electrochemical activity. Notably, the Ni-BDC/MXene/NF-300 electrode showcased a remarkable capacity of 1103.9C g^{-1} at 1 A g^{-1}. When assembled into a Ni-BDC/V_2CT_x/NF-300//AC device, it attained an impressive energy density of 46.3 Wh kg^{-1} at 746.8 W kg^{-1}, alongside an exceptional retention in capacity till 118.1 % even after undergoing 15,000 cycles (Fig. 21c). Moreover, a hybrid consisting of porous NiO microspheres and $Ti_3C_2T_x$ was synthesized by air calcination of Ni-MOF/$Ti_3C_2T_x$, intended for battery-type supercapacitor electrodes. This hybrid demonstrated a superior specific capacitance of 630.9C g^{-1}, as compared to that of pure NiO (376.8C g^{-1}), thereby highlighting its potential for enhancing electrochemical performance [261]. Not only oxidation but also phosphorylation processes have been explored for enhancing the properties of MXene-based materials. In a notable example, a Ni-BDC/MXene composite was subjected to phosphorylation using an aqueous KH_2PO_4 solution to create NiP-MXene (MXene/NPO) electrode [180]. The resulting MXene/NPO electrode displayed a remarkable specific capacity of 639C g^{-1} and exhibited exceptional cycle stability over 10,000 cycles. Similarly, utilizing a similar

Table 3
MXene@MOF composites and their derived materials for SCs.

Sample	Precursor	Specific capacity	Cycling stability (%, cycles)	Energy density/ power density	Ref.
Ni-MOF/MXene	–	867.3 F g^{-1}, 1 A g^{-1}	87.1, 5000, (5 A g^{-1})	–	[178]
ZIF-67@$Ti_3C_2T_x$ fiber	–	972 F cm^{-3}, 1 A cm^{-3}	90.8, 20,000	9.2 mWh cm^{-3}/ 73.5 mW cm^{-3}	[256]
$Ti_3C_2T_x$/Ni-MOFs	–	1124 F g^{-1}, 1 A g^{-1}	83.2, 4000, (10 A g^{-1})	46 Wh kg^{-1}/ 800 W kg^{-1}	[246]
MXene/MPFs	–	408 mF cm^{-2}, 0.5 mA cm^{-2}	95.9, 7000, (50 mV s^{-1})	20.4 μWh cm^{-2}/ 152.2 μW cm^{-2}	[192]
MXene/Ni-MOF	–	979 F g^{-1}, 0.5 A g^{-1}	98, 5000, (3 mA cm^{-2})	–	[154]
Ni/Co-MOF@$Ti_3C_2T_x$-NH_2	–	1924 F g^{-1}, 0.5 A g^{-1}	58.1, 10,000, (10 A g^{-1})	98.1 Wh kg^{-1}/ 600 W kg^{-1}	[257]
Co-MOF/ $Ti_3C_2T_x$@NF	–	3741 F g^{-1}, –	92.1, 3000, (6 mA cm^{-1})	–	[157]
MIL-100 (Fe)/ Ti_3C_2	–	962.1 F g^{-1}, 0.5 A g^{-1}	93, 10,000, (5 A g^{-1})	85.5 Wh kg^{-1}/ 200 W kg^{-1}	[258]
ZIF-L (Zn)@ $Ti_3C_2T_x$ fiber	–	1700 F cm^{-3}, 1 A cm^{-3}	90.2, 20,000, (3 A cm^{-3})	19 mWh cm^{-3}/ 309 mW cm^{-3}	[259]
V_2CT_x@C	V_2CT_x derived MOF	551 F g^{-1}, 2 A g^{-1}	88.2, 5000, (10 A g^{-1})	48.6 Wh kg^{-1}/ 552 W kg^{-1}	[260]
NiO/ $Ti_3C_2T_x$	Ni-MOF/ $Ti_3C_2T_x$	630.9C g^{-1}, 1 A g^{-1}	92.9, 5000, (1 A g^{-1})	–	[261]
Ni-ZIF-67-200/ MXene	Ni-ZIF-67	557C g^{-1}, 0.5 A g^{-1}	66, 5000, (2 A g^{-1})	27.5 Wh kg^{-1}/ 400 W kg^{-1}	[262]
Co-BDC/ $Ti_3C_2T_x$-300	Co-BDC/ $Ti_3C_2T_x$	1453C m^{-2}, 2 A m^{-2}	92, 2500, (5 A m^{-2})	176.3 Wh l^{-1}/ 337.5 W l^{-1}	[263]
N-doped carbon-$Ti_3C_2T_x$	ZIF-8/ $Ti_3C_2T_x$	82.8 F g^{-1}, 1 A g^{-1}	~100, 5000, (2 A g^{-1})	–	[264]
Co-Fe oxide/ $Ti_3C_2T_x$	Co-Fe MOF	356.4 mF cm^{-2}, 0.2 mA cm^{-2}	88.2, 10,000, (1.5 mA cm^{-2})	79.2 mWh cm^{-3}/ 0.4 mW cm^{-3}	[265]
$CoNi_2S_4$/MXene/ NF	ZIF-67/NF	933C g^{-1}, 1 A g^{-1}	80.5, 10,000, (10 A g^{-1})	30.5 Wh kg^{-1}/ 1587 W kg^{-1}	[245]
$CoNi_2S_4$/MXene	ZIF-67/ MXene	751C g^{-1}, 1 A g^{-1}	72.1, 5000, (10 A g^{-1})	33.8 Wh kg^{-1}/ 800 W kg^{-1}	[266]
MXene/NiCoZDH	MXene/ NiCo-ZIF-67	877 F g^{-1}, 1 A g^{-1}	90.9, 30,000, (15 A g^{-1})	34 Wh kg^{-1}/ 748 W kg^{-1}	[234]
V_2CT_x@NiCoMn-OH	V_2CT_x@ZIF-67	827.5C g^{-1}, 1 A g^{-1}	88.4, 10,000, (20 A g^{-1})	88.3 Wh kg^{-1}/ 7500 W kg^{-1}	[267]
ZSC-LDH@MXene	ZIF-67	2059 F g^{-1}, 1 A g^{-1}	92, 10,000, (10 A g^{-1})	43.7 Wh kg^{-1}/ 789 W kg^{-1}	[268]
$Ti_3C_2T_x$/ZIF-67/ CoV_2O_6	$Ti_3C_2T_x$/ZIF-67	264.5 F g^{-1}, 1 A g^{-1}	94.4, 4000, (3 A g^{-1})	36.3 μWh cm^{-2}/ 0.8 μW cm^{-2}	[170]
$Co_3S_4/Ti_3C_2T_x$	ZIF-67/ $Ti_3C_2T_x$	602 F g^{-1}, 1 A g^{-1}	88.3, 5000, (5 A g^{-1})	44.9 Wh kg^{-1}/ 800.3 W kg^{-1}	[269]
$NH_4CoPO_4.H_2O$/ $Ti_3C_2T_x$	ZIF-67/ $Ti_3C_2T_x$	601 F g^{-1}, 1 A g^{-1}	87, 5000, (5 A g^{-1})	47 Wh kg^{-1}/ 1350 W kg^{-1}	[270]
p-MXene@Ni_3S_4/ CuS	p-MXene@Ni-MOF	1917 F g^{-1}, 1 A g^{-1}	91.2, 30,000, (5 A g^{-1})	87.6 Wh kg^{-1}/ 7750 W kg^{-1}	[271]
MXene@$CoSe_2$/ Ni_3Se_4	MXene/ZIF-67	2038 F g^{-1}, 1 A g^{-1}	75, 10,000, (5 A g^{-1})	41.2 Wh kg^{-1}/ 3100 W kg^{-1}	[103]
N-$Ti_3C_2T_x$/C/CuS	$Ti_3C_2T_x$/ZIF-67	1205.8 F g^{-1}, 1 A g^{-1}	90, 3000, (5 A g^{-1})	77.2 Wh kg^{-1}/ 649.5 W kg^{-1}	[272]

phosphorylation approach, the ZIF-67/$Ti_3C_2T_x$ composite underwent etching through an $(NH_4)_2HPO_4$ solution to yield NH_4CoPO_4• H_2O/ $Ti_3C_2T_x$ materials for high-performance asymmetric devices. These devices demonstrated impressive energy densities of 47 Wh kg^{-1} at 1350 W kg^{-1} and 18 Wh kg^{-1} at 5000 W kg^{-1} [270]. Moreover, the allure of metal sulfides, renowned for their notable electrochemical activity and capacity, has captivated substantial attention. In a creative approach, a sandwich-like porous architecture, denoted as p-MXene@Ni_3S_4/CuS (p-MXene@Ni_3S_4/CuS), was fabricated through the sulfurization of p-MXene@Ni-MOF alongside supplementary Cu^{2+} with the aid of TAA (Fig. 21d) [271]. The amalgamation of Ni_3S_4 and CuS within the p-MXene@Ni_3S_4/CuS composite brought forth a reservoir of redox potentials and an enlarged theoretical specific capacitance, as depicted in Fig. 21e. The p-MXene@Ni_3S_4/CuS//AC ASC device showcased an exemplary capacitance retention rate of 92.4 % even after an extensive 30,000 cycles (Fig. 21f). Utilizing a comparable sulfide-based strategy, $Co_3S_4/Ti_3C_2T_x$ emerged via the hydrothermal sulfidation of ZIF-67/ $Ti_3C_2T_x$ composites (Fig. 21g) [269]. The resulting $Co_3S_4/Ti_3C_2T_x$ electrode demonstrated notable capacity of 602 F g^{-1} at 1 A g^{-1}, surpassing that of the parent ZIF-67/$Ti_3C_2T_x$ counterpart (Fig. 21h). Remarkably, the resultant asymmetric devices showed a notable energy density of 44.9 Wh kg^{-1} at a power density of 800.3 W kg^{-1}, coupled with enduring cycling performance spanning over 5000 cycles (Fig. 21i).

Substituting the metal ions or organic linkers of MOFs with functional ions has emerged as a convenient and cost-effective approach to fine-tune the original MOFs energy storage activity. Notably, a study highlighted the creation of hollow $Ti_3C_2T_x$/ZIF-67/CoV_2O_6 composites achieved by replacing 2-methylimidazole ligands with polyvanadate ions derived from NH_4VO_3 [170]. This innovative strategy yielded the $Ti_3C_2T_x$/ZIF-67/CoV_2O_6 electrode, boasting an enhanced capacity of 253.8 F g^{-1} at 5 A g^{-1}, surpassing its precursors. Intriguingly, the energy density of the $Ti_3C_2T_x$/ZIF-67/CoV_2O_6//AC device outperformed that of

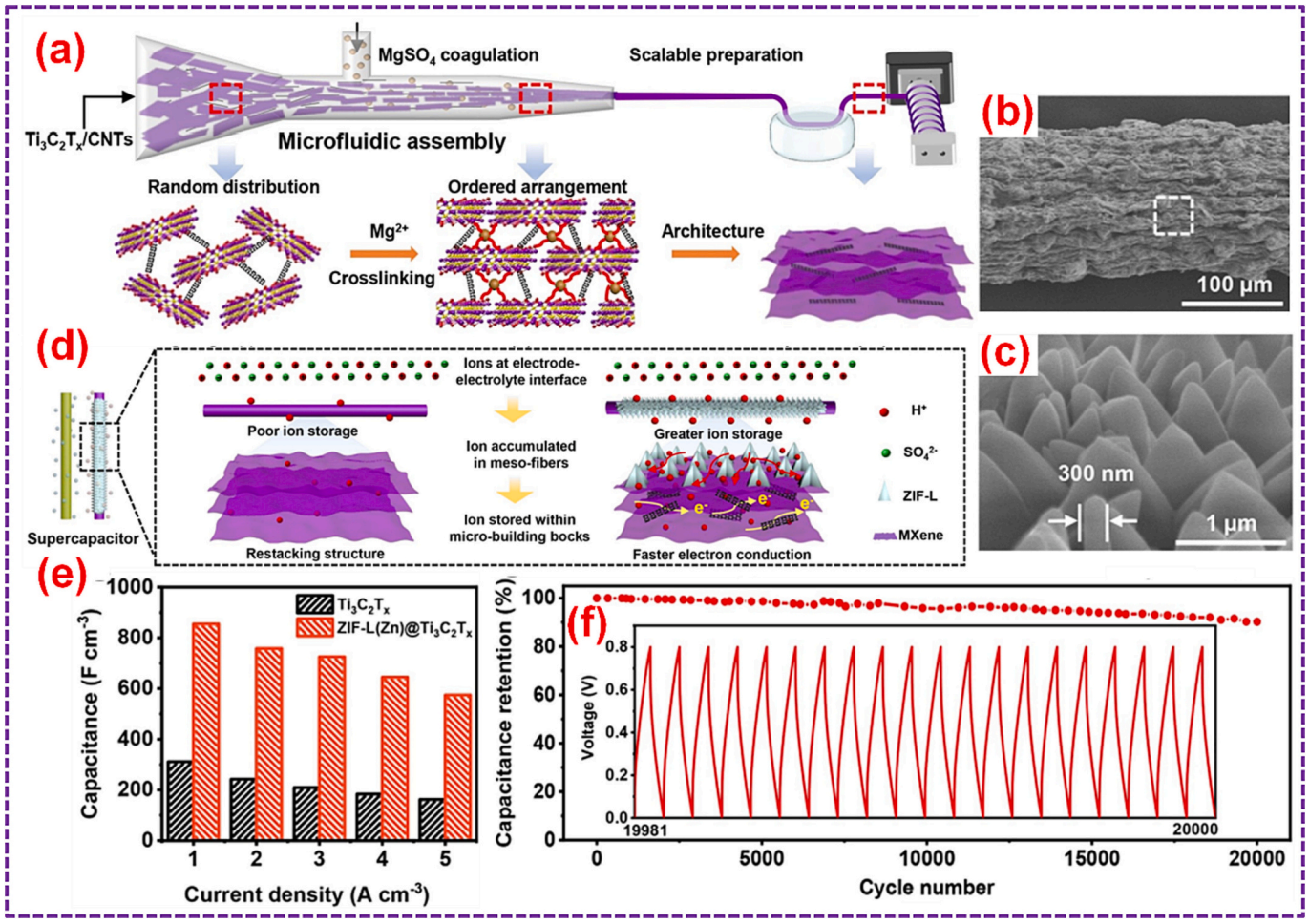

Fig. 18. (a) Microfluidic assembly of MXene fibers. (b, c) SEM analysis of the ZIF-L (Zn)@$Ti_3C_2T_x$ fiber. (d) Pictorial representation of mechanism of energy storage performances of ZIF-L(Zn)@$Ti_3C_2T_x$ FESC. (e) Volumetric capacitances of the ZIF-L (Zn)@$Ti_3C_2T_x$ fiber. (f) Cycle stability of ZIF-L (Zn)@$Ti_3C_2T_x$ FESC (inset: GCD analysis for the last 20 cycles). Adopted with permission from Ref. [259], Copyright 2021, Wiley-VCH.

the $Ti_3C_2T_x$/ZIF-67//AC device, further confirming the capacity improvement post the ion exchange activity. Furthermore, the transformation of MOFs into LDHs holds the potential to elevate the pristine materials performance owing to the expansive theoretical specific capacitance, abundant surface area, and heightened redox capability associated with LDHs. A notable example involves the fabrication of MXene-wrapped ZIF skeleton-cavity LDHs (ZSC-LDH@MXene) as high-performance electrodes [268]. The distinctive architecture of ZSC-LDH@MXene is illustrated in Fig. 22a. This design encompasses a rich conductive network and a cavity composed of NSs that facilitate rapid electron/ion transport, amplify electrolyte accessibility, expose ample active sites, and even mitigate volume fluctuations during charge/discharge cycles. The resulting electrode showcased an enhanced capacity of 1029.6C g^{-1} at 1 A g^{-1} and an impressive capacity retention of 92 % over 10,000 cycles, as depicted in Fig. 22b. Similarly, a range of MXene@ZIF-67/$Co(OH)_2$ (ZCH) composites featuring a core-shell/yolk-shell/hollow (CS/YS/Ho) structure was devised by meticulously controlling the alcoholysis of Co^{2+} ions [205]. The morphological evolution of MXene@Ho-CH is captured in Fig. 22c, d, where ZIF-67 transforms entirely into hollow LDH cubes. MXene@Ho-CH demonstrated a commendable capacity of 348.55 F g^{-1} at 1 A g^{-1}, surpassing the performance of individual components such as MXene, ZIF-67, MXene@-ZIF-67, LDH, MXene@CS-ZCH, and MXene@YS-ZCH, as demonstrated in Fig. 22e. Furthermore, diverse metal species within LDHs were explored to create highly stable electrode materials. Notably, a process involving the anchoring of NiCo-ZIF-67 onto MXene, followed by its conversion into LDHs (MXene/NiCoZDH) through alkali treatment, was developed [234]. The resulting MXene/NiCoZDH electrode exhibited remarkable cyclic stability over an impressive 30,000 cycles. In comparison to mono- or bi-metal hydroxides, tri-metal hydroxides displayed superior synergistic effects, featuring a greater array of mixed-valence states and redox-active centers. For instance, the transformation of V_2CT_x@ZIF-67 into the V_2CT_x@NiCoMn-OH composite was achieved through a straightforward anion exchange route, yielding high-performance electrode materials, as depicted in Fig. 22f [267]. The resultant structure combined interconnecting NiCoMn-OH hollow nanospheres with V_2CT_x, thus furnishing ample active surface area while effectively constraining volume variations during charge/discharge cycles. Notably, the optimized V_2CT_x@NiCoMn-OH-20 electrode demonstrated a commendable specific capacitance of 706C g^{-1}, alongside a capacity retention of 85.32 %, as illustrated in Fig. 22g. Moreover, upon assembly, the V_2CT_x@NiCoMn-OH-20//AC configuration exhibited an exceptional energy density of 88.35 Wh g^{-1} at 750 W g^{-1}, accompanied by an excellent cycle stability, boasting a capacitance retention of 91.83 % after 5000 cycles, as shown in Fig. 22h.

Significantly, the performance of MXene/MOF-derived LDH composites can be further elevated through additional selenization or sulfidation processes. Yang et al. [103] demonstrated the enhancement of electrochemical activity in the MXene@ZIF-67-derived MXene@NiCo-LDH composite through its transformation into MXene@$CoSe_2$/Ni_3Se_4. The synergistic effect and distinctive honeycomb type structure of MXene@$CoSe_2$/Ni_3Se_4 contributed to a commendable specific

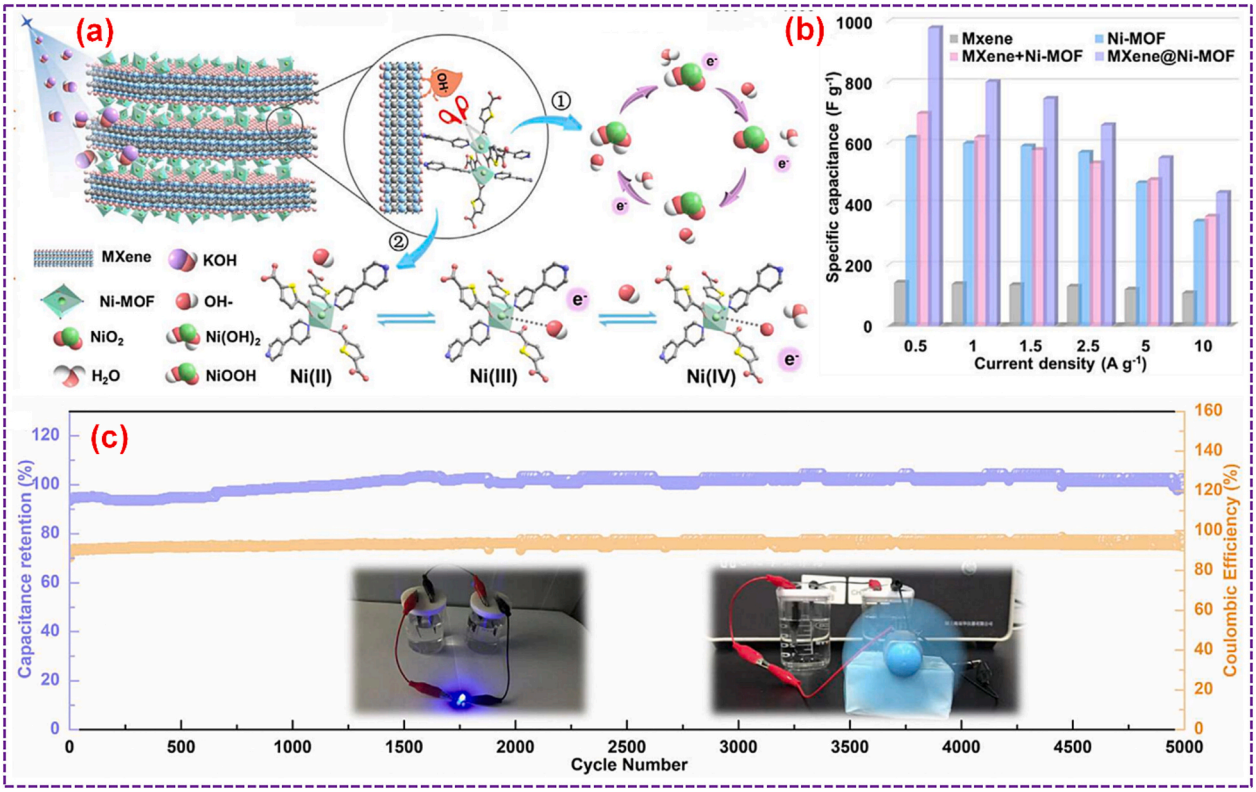

Fig. 19. (a) Pictorial representation of charge/discharge mechanism of MXene@Ni-MOF electrode. (b) Specific capacitance of Ni-MOF, MXene, MXene+Ni-MOF, and MXene@Ni-MOF electrodes. (c) Cycling stability of the MXene@Ni-MOF//AC device (inset: Images of the assembled device linked with blue LED and power a rotating motor). Adopted with permission from Ref. [154], Copyright 2022, Elsevier B.V. (For interpretation of the references to colour in this figure legend, the reader is referred to the web version of this article.)

capacitance of 283 mAh g^{-1}, surpassing that of MXene/NiCo-LDH (as depicted in Fig. 22i). Notably, the MXene@$CoSe_2$/Ni_3Se_4 electrode displayed an increased capacity retention of 75 % after 10,000 cycles, outperforming the 56 % capacity retention of MXene@NiCo-LDH. Additionally, Qi et al. [266] revealed the capacity improvement achieved by sulfidating ZIF-67/MXene-derived NiCo-LDH/MXene into $CoNi_2S_4$/MXene. As shown in Fig. 22j, the $CoNi_2S_4$/MXene electrode showcased the highest capacity (751C g^{-1} at 1 A g^{-1}) among all tested electrodes. Moreover, the strategic placement of MXene@MOF derivatives on functional substrates can significantly enhance the electrochemical activity. The mechanism of forming MXene-modulated $CoNi_2S_4$ dendrites on a conductive NF is depicted in Fig. 22k. Initially, ZIF-67 was etched into NiCo-LDH, followed by sulfurization into MXene-wrapped $CoNi_2S_4$ nanotrees with the addition of MXene suspension [245]. This unique dendritic morphology exposed numerous electroactive sites, resulting in an excellent capacity of 933C g^{-1} at 1 A g^{-1} for the obtained electrode. Furthermore, the assembled $CoNi_2S_4$/MXene/NF//reduced graphene oxide (rGO) asymmetric device demonstrated an outstanding energy density of 30.5 Wh kg^{-1} at 1587 W kg^{-1}.

5.2. Batteries

5.2.1. Alkali metal-ion batteries

Alkali metal-ion batteries, encompassing lithium-ion batteries (LIBs), sodium-ion batteries (SIBs), and potassium-ion batteries (PIBs), stand as pivotal environmentally friendly and sustainable technologies aimed at mitigating the energy and environmental challenges stemming from the combustion of fossil fuels [277]. Within this domain, LIBs have undergone extensive research owing to its favorable reaction kinetics and relatively high energy density. While Li^+ holds a prime position, Na^+ and K^+ ions retain larger radius, resulting in SIBs and PIBs exhibiting slower reaction kinetics and more pronounced volumetric changes. Nonetheless, SIBs and PIBs remain highly promising alternatives to LIBs, driven by the necessity to manage the finite reserves of lithium resources. In this context, our focus revolves around MXene@MOF composites and their derived materials as functional electrodes for metal-ion batteries. The recent achievements of these materials in metal-ion batteries are summarized in Table 4.

Based on the charge/discharge mechanism inherent to LIBs, the reversible intercalation and deintercalation of Li ions primarily occur within the organic constituents of MOFs [291,293,294]. In the context of enhancing lithium storage performance, the incorporation of Ni-NDC, featuring a stable porous structure with excellent electrolyte accessibility and high Li^+ diffusion rate, with MXene has been explored [295]. The optimized Ni-NDC/MXene configuration, depicted in Fig. 23a, showcases a uniform distribution of Ni-NDC across the MXene framework. This hierarchical architecture significantly enhances the stability of both Ni-NDC and MXene, facilitating accelerated Li^+ diffusion and transmission. Comparative rate analysis, as illustrated in Fig. 23b, demonstrates the superior rate capability of the optimized Ni-NDC/MXene over pure Ni-NDC. The resulting electrode exhibits a reversible discharge capacity of 579.8 mAh g^{-1} at 0.1 A g^{-1} and showcases robust cycling performance, retaining a capacity of 310 mAh g^{-1} at 1 A g^{-1} even after 500 cycles. The Li^+ storage mechanism within Ni-NDC/MXene involves a combination of pseudocapacitive- and diffusion-controlled reaction activities, with the pseudocapacitance contribution increasing as current density rises, as depicted in Fig. 23c. Furthermore, the combination of electroconductive ferrocene-based MOFs possessing alluring redox activities and exceptional structural robustness with MXene has led to the creation of heterostructures for lithium-storage capacity, exemplified by Ni-ferrocene dicarboxylic MOF (NF-MOF)/$Ti_3C_2T_x$ MXene (NF-MOF@MXene) hybrids [279]. The synthesized NF-MOF@MXene exhibits a morphology where NF-MOF nanosheet arrays uniformly extend over MXene NSs, as depicted in Fig. 23d. The resulting

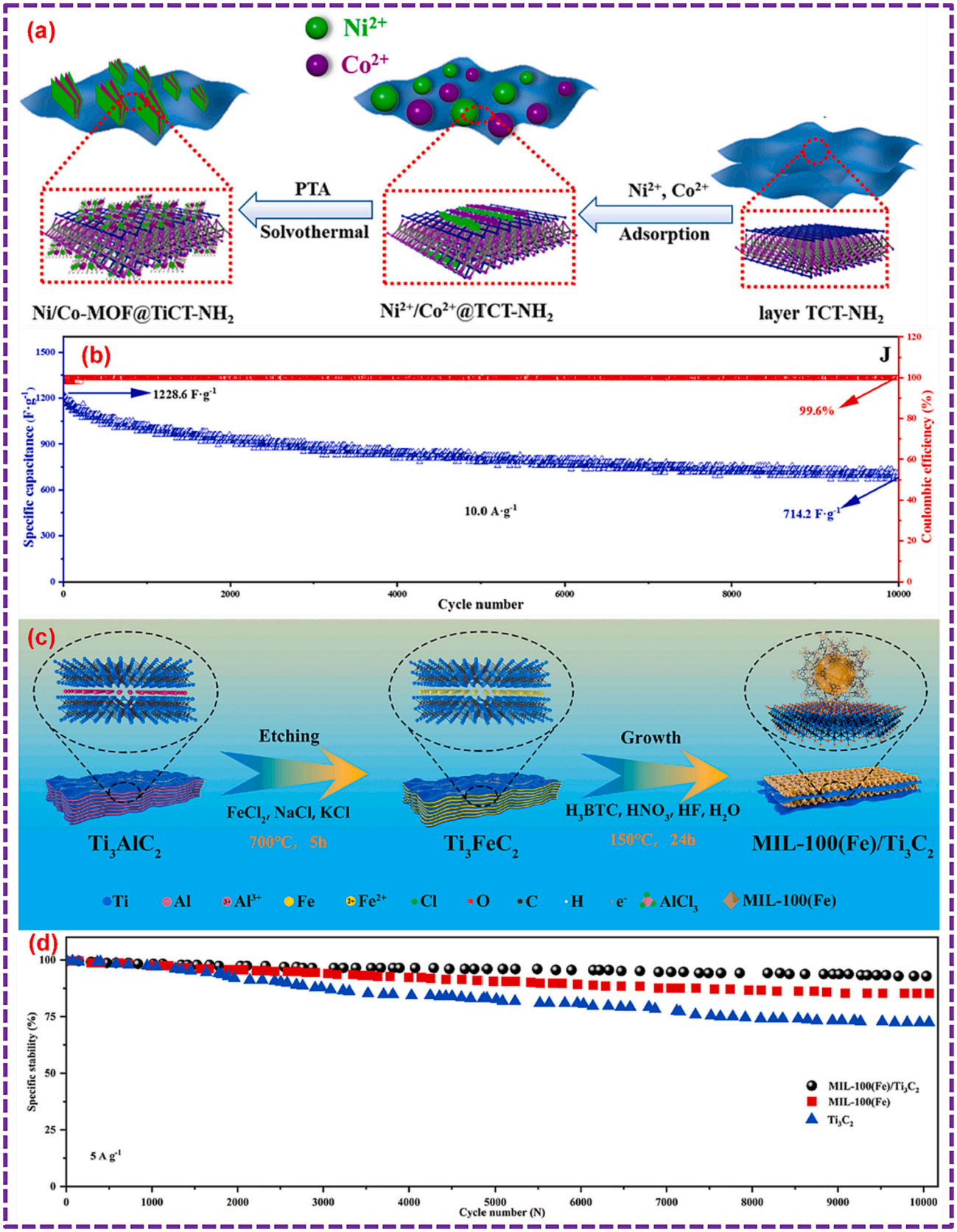

Fig. 20. (a) Scheme for the preparation of the Ni/Co-MOF@TCT-NH_2 hybrid. (b) Cycling stability of the Ni/Co-MOF@TCT-NH_2 electrode. Adopted with permission from Ref. [257], Copyright 2022, Elsevier B.V. (c) Pictorial representation of the preparation activity of MIL-100(Fe)/Ti_3C_2 hybrid. (d) Cyclic stability of Ti_3C_2, MIL-100(Fe) and MIL-100(Fe)/Ti_3C_2 electrodes. Adopted with permission from Ref. [258], Copyright 2022, Elsevier B.V.

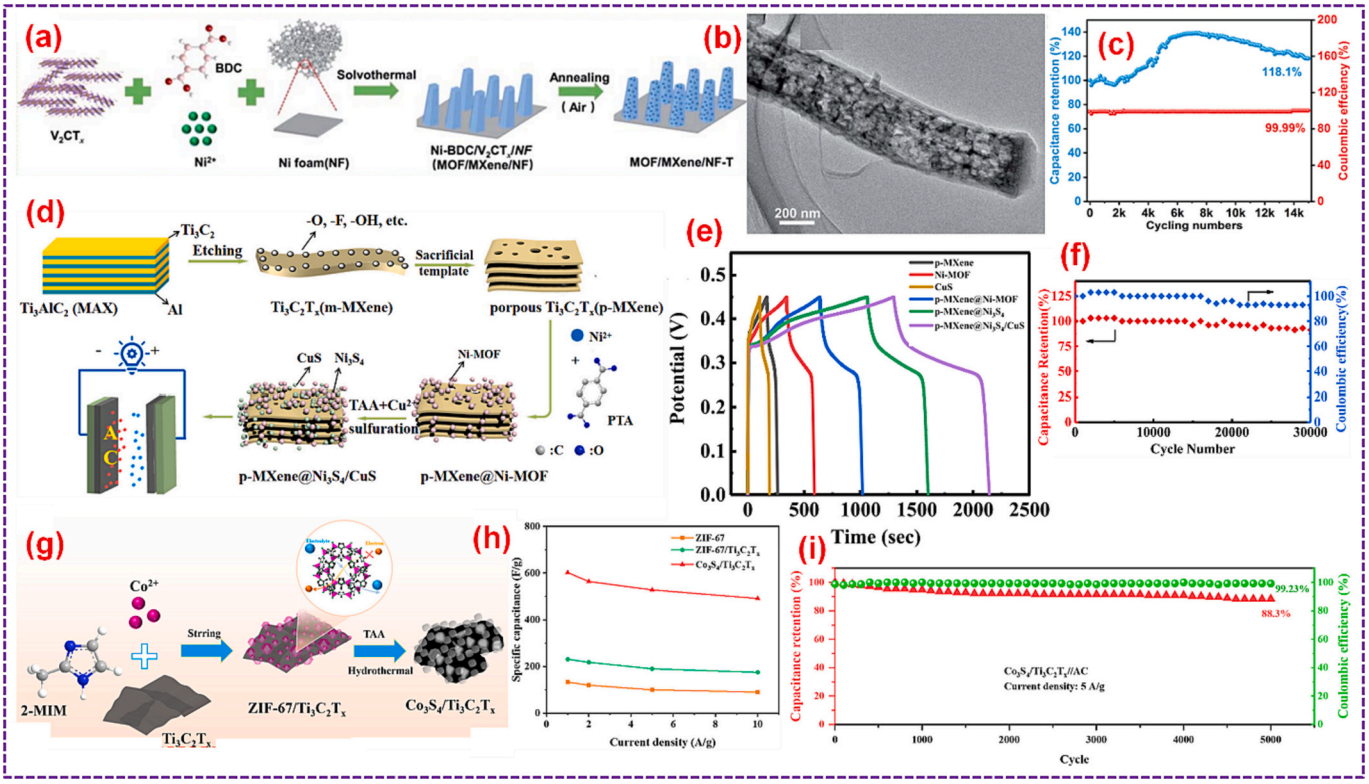

Fig. 21. (a) Pictorial representation of Ni-BDC/MXene/NF based electrodes. (b) TEM analysis of Ni-BDC/MXene/NF-300. (c) Cycling performance of the Ni-BDC/V_2CT_x/NF-300//AC device. Adopted with permission from Ref. [211], Copyright 2022, The Royal Society of Chemistry. (d) Synthetic procedures of p-MXene@Ni_3S_4/CuS. (e) GCD plots of p-MXene, Ni-MOF, CuS, p-MXene@Ni-MOF, p-MXene@Ni_3S_4, and p-MXene@Ni_3S_4/CuS. (f) Cycling stability of p-MXene@Ni_3S_4/CuS//AC. Adopted with permission from Ref. [271], Copyright 2022, Elsevier B.V. (g) Synthesis steps of ZIF-67/$Ti_3C_2T_x$ and Co_3S_4/$Ti_3C_2T_x$. (h) Specific capacitances of ZIF-67, ZIF-67/$Ti_3C_2T_x$, and Co_3S_4/$Ti_3C_2T_x$ samples with respect to distinct current densities. (i) Cycle stability of Co_3S_4/$Ti_3C_2T_x$//AC ASC. Adopted with permission from Ref. [269], Copyright 2022, Elsevier B.V.

anode showcases a significant capacity retention of 80 % even after 5000 cycles. Fast Li^+ insertion/extraction kinetics within NF-MOF@MXene, illustrated in Fig. 23e, f, are attributed to enhanced Li^+ adsorption energy due to interfacial interactions within the NF-MOF@MXene heterostructure. Furthermore, a series of PBA/MXene composites were explored for Li^+ storage applications [296]. As illustrated in Fig. 23g, the incorporation of MXene substrate effectively reduces the PBAs particle size, mitigating the significant capacity decline and inferior cycle stability observed in PBAs. The optimized $Ni_{0.8}Mn_{0.2}$-PBA/MX electrode demonstrates improved rate capacity and notable cycle stability, delivering 259.9 mAh g^{-1} at 1 A g^{-1} after 650 cycles (Fig. 23h, i).

Novel anodes for LIBs have emerged in the form of MXene/MOF-derived hybrids. In a striking example, spherical Co-MOFs were combined with selenium (Se) powder and subjected to thermal treatment to yield $CoSe_2$ hollow spheres. These spheres were further integrated with MXene through an electrostatic self-assembly process [285]. The resultant $CoSe_2$@MXene hybrids benefited from the distinct porous structure of hollow-shell $CoSe_2$@MXene, and the robust Co-O-Ti covalent bonds formed at the MXene and $CoSe_2$ interfaces, optimizing both electron/ion transport and structural stability (depicted in Fig. 24a, b). Remarkably, $CoSe_2$@MXene displayed exceptional rate capacity, reaching 465 mAh g^{-1} at 5 A g^{-1} (illustrated in Fig. 24c), along with a cycle stability of over 1000 cycles. Additionally, Fig. 24d underscores the superior reaction kinetics of $CoSe_2$@MXene compared to $CoSe_2$ sphere and pure $CoSe_2$, as evidenced by the steeper slope observed for $CoSe_2$@MXene. Cao et al. [162] introduced a noteworthy advancement in high-performance LSBs with their 0D—2D ZIF-8-derived ZnS nanodots/$Ti_3C_2T_x$ MXene hybrids. The interaction between ZnS nanodots and MXene NSs, as depicted in Fig. 24e, synergistically enhanced electron transfer and lithium adsorption/diffusion. This synergy contributed to the remarkable performance of ZnS/MXene hybrids, showcasing an impressive capacity of 726.8 mAh g^{-1} and exceptional cycle stability with 462.8 mAh g^{-1} after 1000 cycles at 500 mA g^{-1} depicted in Fig. 24f. Similarly, Yao et al. [89] presented a superior approach for alkali-ion batteries by anchoring ZIF-67 derived carbon-confined CoS NPs within the MXene aerogel framework, creating a composite denoted as (CoS NP@NHC)@MXene. The microstructure of (CoS NP@NHC)@MXene, depicted in Fig. 24g, revealed a well-designed composition with a closely interconnected MXene framework and a porous structure embedded with abundant CoS NPs. This ingenious design facilitated effective electron/ion transport. Impressively, the achieved (CoS NP@NHC)@MXene anode demonstrated exceptional cycle stability, maintaining a capacity of 1145.9 mAh g^{-1} even after 800 cycles illustrated in Fig. 24h.

The exploration of LIB anode materials has extended to combining MXene with MOF-derived LDHs, offering a promising avenue for enhancing performance [282]. In this context, ZIF-67 has been employed as a sacrificial template to construct well-ordered LDH nanosheet arrays atop MXene. This strategy not only furnishes ample accessible surface areas but also curtails Li^+ diffusion pathways. Comparatively, the resultant Co-LDH/MXene presented a significantly elevated reversible capacity of 398 mAh g^{-1}, surpassing the precursor ZIF-67/MXene composite. To further amplify the electrochemical prowess of MOF-derived LDH/MXene composites, Zhao et al. [82] ingeniously transformed ZIF-67 derived CoMo LDH@MXene structures into CoO/$Co_2Mo_3O_8$@MXene hollow frameworks via controlled thermal annealing. The morphology depicted in Fig. 25a, b underscores the creation of intricate hollow hierarchical architectures, replete with an abundance of metal oxide NFs that engender open pathways. This distinctive architecture expedites rapid charge transport at interfaces

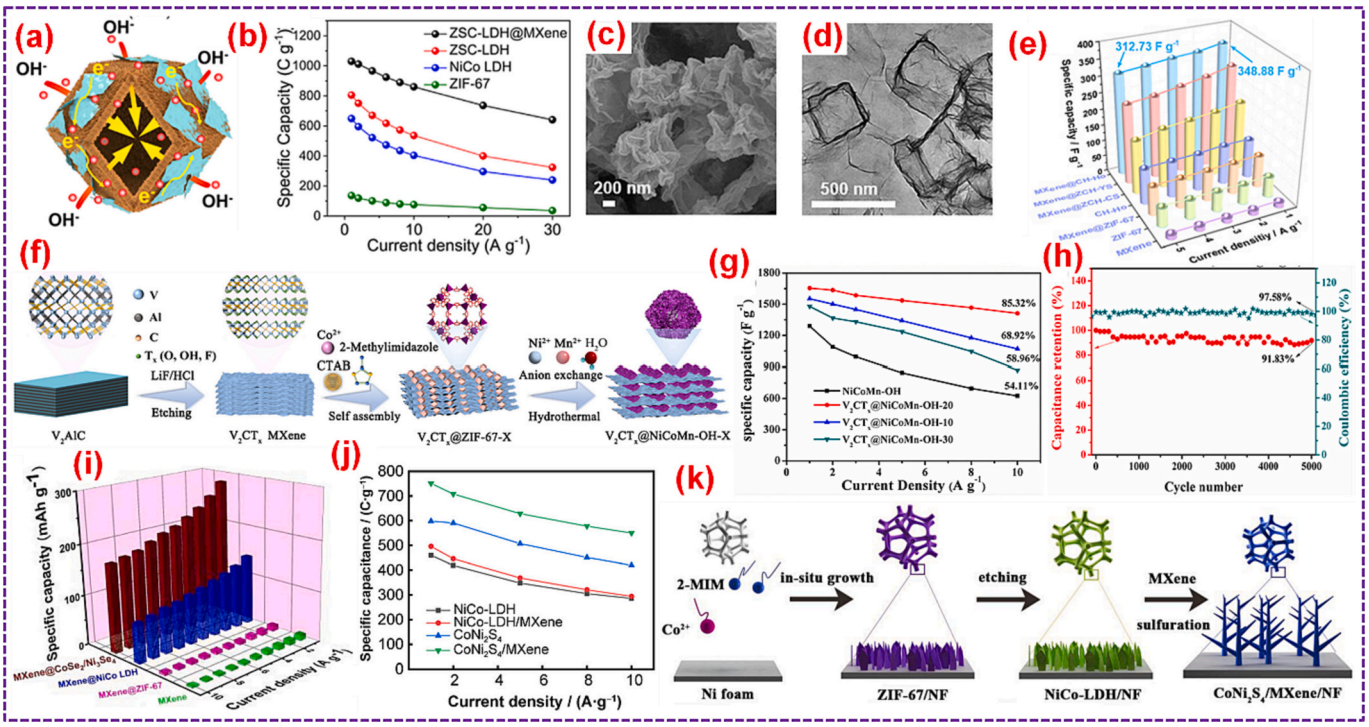

Fig. 22. (a) Pictorial representation of the ion/electron transport in ZSC-LDH@MXene. (b) Specific capacity of various samples with respect to different current densities. Adopted with permission from Ref. [268], Copyright 2023, The American Chemical Society. (c) SEM image, and (d) TEM image of MXene@Ho-CH. (e) specific capacitance of various samples with respect to different current densities. Adopted with permission from Ref. [205], Copyright 2022, The Royal Society of Chemistry. (f) Pictorial representation of the fabrication of V_2CT_x@NiCoMn-OH-x. (g) Specific capacity of various samples with respect to different current densities. (h) Cycle performance of the V_2CT_x@NiCoMn-OH-20//AC device. Adopted with permission from Ref. [267], Copyright 2022, Elsevier B.V. (i) specific capacitance of various samples with respect to different current densities. Adopted with permission from Ref. [103], Copyright 2022, Elsevier B.V. (j) specific capacitance of various samples with respect to different current densities. Adopted with permission from Ref. [266], Copyright 2022, Springer. (k) Scheme for the synthesis of the dendrite $CoNi_2S_4$/MXene/NF. Adopted with permission from Ref. [245], Copyright 2021, Elsevier B.V.

Table 4
MXene@MOF composites and their derived materials for alkali metal-ion batteries.

Anode	MOF template	Application	ICE (%)	Reversible capacity (mAh g^{-1}, A g^{-1})	Cycling performance (mAh g^{-1}, A g^{-1}, cycles)	Ref.
Ni-NDC/MXene	–	LIBs	48	579.8, 0.5	310, 1, 500	[190]
CoP-NC@$Ti_3C_2T_x$	ZIF-67@ $Ti_3C_2T_x$	LIBs	–	245.6, 0.1	212.9, 1, 2000	[226]
CoO/$Co_2Mo_3O_8$@MXene	ZIF-67	LIBs	41.2	947.4, 0.1	545, 2, 1200	[82]
$Ti_3C_2T_x$/NiCo-BDC	–	LIBs	–	583, 0.1	637, 0.2, 200	[238]
MOFs-CoP@MXene	ZIF-67@ MXene	LIBs	69.6	706.5, 0.2	585.8, 0.5, 1000	[278]
NF-MOF@MXene	–	LIBs	52	715, 0.5	105, 5, 5000	[279]
Co_3O_4@NGC/MXene	ZIF-67@ MXene	LIBs	67.6	327, 50	830, 1, 500	[166]
$Co_2V_2O_7$@$Ti_3C_2T_x$	ZIF-67	LIBs	58.5	1098.6, 0.1	490.3, 2, 450	[280]
ZnS/MXene	ZIF-8/MXene	LIBs	54.8	650.6, 0.1	462.8, 0.5, 1000	[162]
Ti_3C_2@Co_3O_4/ZnO	Co/Zn MOF	LIBs	64	401.4, 0.1	229, 2, 1000	[281]
Co-LDH/MXene	ZIF-67@ MXene	LIBs	54.7	854.9, 0.1	398, 1, 400	[282]
$Ti_3C_2T_x$@$MoSe_2$	Ti_3C_2@Mo-MOF	LIBs	76.7	245.6, 0.03	230, 0.3, 800	[283]
(CoS NP@NHC)@MXene	ZIF-67@MXene	LIBs	76	1563.2, 0.1	1145.9, 1, 800	[89]
Si/MXene@C	Si/MXene@ZIF-8	LIBs	65.7	1006.1, 0.1	862.9, 0.1, 150	[284]
$CoSe_2$@MXene	Co-MOF	LIBs	71.9	1051, 0.2	1279, 1, 1000	[285]
MXene@CoS_2/NC	PMMA@MXene@ZIF-67	SIBs	74	620, 0.2	355, 5, 5000	[286]
$CoSe_2$@CNTs-MXene	ZIF-67@MXene	SIBs	81.7	450.5, 1	400, 2, 200	[287]
CoP-NC@$Ti_3C_2T_x$	ZIF-67@$Ti_3C_2T_x$	SIBs	–	151, 0.05	101.6, 0.5, 500	[226]
(CoS NP@NHC)@MXene	ZIF-67@MXene	SIBs	65	577.9, 0.1	420, 2, 650	[89]
MXene@Co_9S_8/$CoMo_2S_4$	MXene@ZIF-67	SIBs	88.6	312, 0.1	196, 1, 350	[288]
MXene@CoP@NPC	MXene@ZIF-L	SIBs	–	242, 0.2	155, 1, 1000	[289]
Co_3C/MXene@C	ZIF-67@MXene	SIBs	44.6	282.4, 0.2	172, 0.5, 500	[290]
ZnTe@C/$Ti_3C_2T_x$	ZIF-8	PIBs	51.6	408, 0.1	230.2, 1, 3500	[291]
V_2CT_x derived MOF	V_2CT_x	PIBs	50	250, 0.05	-, 1, 800	[292]
Co_3C/MXene@C	ZIF-67@MXene	PIBs	36.7	236, 0.2	129.3, 0.5, 500	[290]
(CoS NP@NHC)@MXene	ZIF-67@MXene	PIBs	58	284.4, 0.1	210, 2, 500	[89]

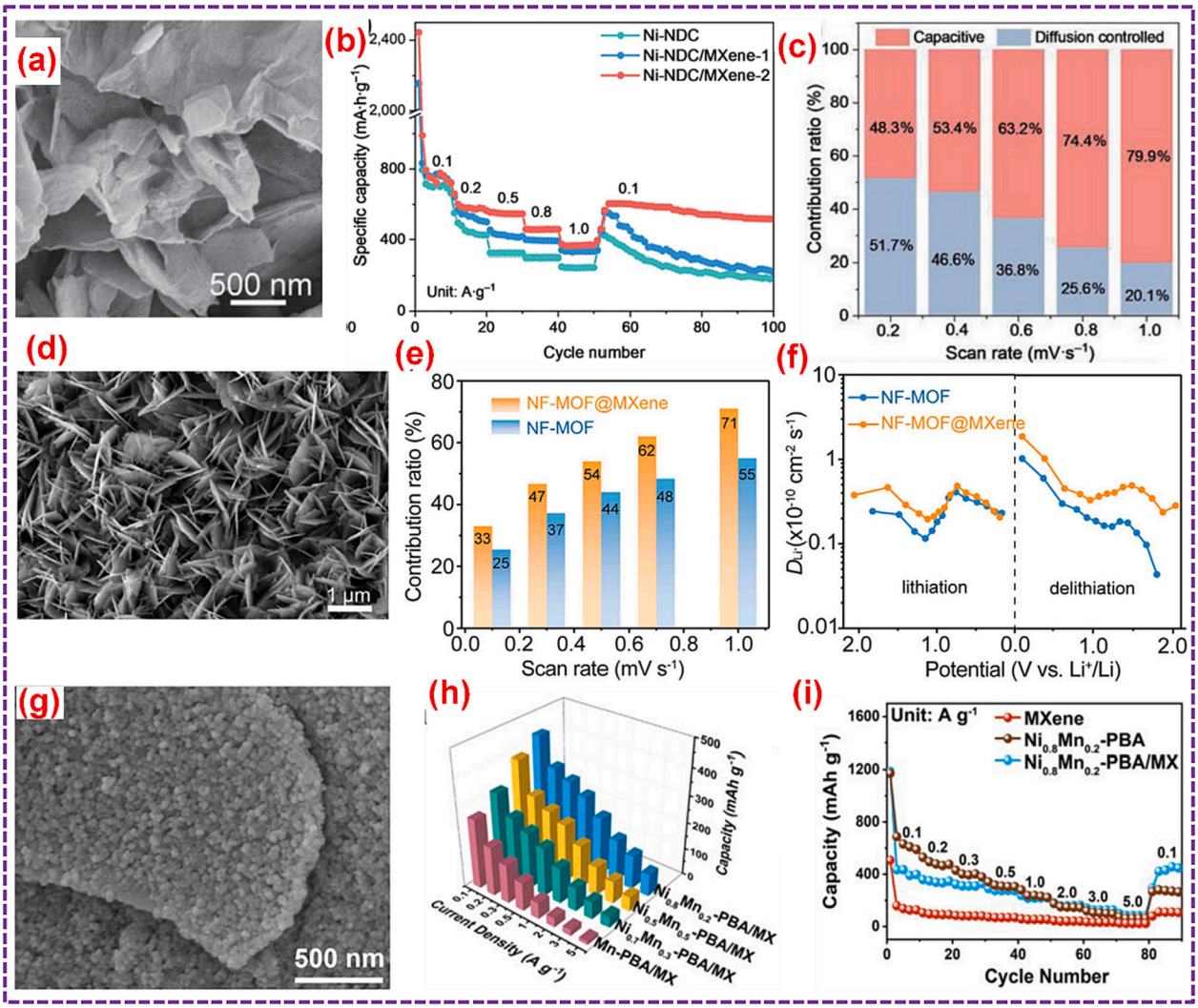

Fig. 23. (a) SEM analysis of Ni-NDC/MXene. (b) Rate performance of Ni-NDC and Ni-NDC/MXene composite. (c) Plot of capacitive and diffusion contributions of the optimized Ni-NDC/MXene composite. Adopted with permission from Ref. [190], Copyright 2023, Springer. (d) SEM analysis of NF-MOF@MXene. (e) Capacitive contribution of NF-MOF@MXene. (f) Li^+ diffusion coefficient of NF-MOF@MXene. Adopted with permission from Ref. [279], Copyright 2023, Elsevier B.V. (g) SEM analysis of $Ni_{0.8}Mn_{0.2}$-PBA/MX. (h) Specific capacities of PBA/MX samples. (i) Rate capabilities of MXene, $Ni_{0.8}Mn_{0.2}$-PBA, and $Ni_{0.8}Mn_{0.2}$-PBA/MX. Adopted with permission from Ref. [296], Copyright 2022, The American Chemical Society.

and accommodates the volume fluctuations inherent in $CoO/Co_2Mo_3O_8$. This arrangement ultimately ensures commendable rate performance and cyclic stability, as evidenced in Fig. 25c, d. Furthermore, Fig. 25e provides compelling evidence that the inclusion of MXene successfully mitigates the charge transfer impedance of $CoO/Co_2Mo_3O_8$. Altogether, the coupling of TMOs, with their alluring theoretical capacities, with MXene demonstrates its potential as a compelling strategy for augmenting LIB anodes. In their study, Zheng et al. [280] devised a method to fabricate hollow polyhedrons of MOF-derived $Co_2V_2O_7$@$Ti_3C_2T_x$ MXene (CVO@MXene) for efficient Li^+ storage. The incorporation of MXene as a shell served a dual purpose: it not only introduced abundant ion storage sites through valence changes in Ti centers and surface group redox activities, but also provided a robust framework to safeguard the inner $Co_2V_2O_7$ from structural collapse during lithiation and delithiation processes. The cooperative effects of $Co_2V_2O_7$ and $Ti_3C_2T_x$ in Li^+ storage is depicted in Fig. 25f, g. The prepared CVO@MXene hybrids demonstrated an impressive capacitance of 949.7 mAh g^{-1} at 0.1 A g^{-1} and exhibited enhanced stability over 450 cycles, as highlighted in Fig. 25h, i.

In recent times, there has been a growing interest in SIBs as favorable alternatives within the energy storage domain. However, the limited performance in terms of cycle stability and rate capability has hindered the broader adoption of SIBs [297]. Consequently, there's a need to explore electrode materials with optimal capacitance and favorable electrochemical reaction kinetics. The utilization of oxides/chalcogenides/phosphides of metal derived from MOFs has garnered significant attention owing to their impressive theoretical specific capacitance [298]. Notably, the incorporation of the conductive MXene network holds the potential to substantially enhance the structural integrity of active materials during Na insertion and extraction processes. Addressing this, Xu et al. [287] put forward a novel anode material named $CoSe_2$@CNTs-MXene, characterized by a distinctive “sheet-tube-dots” hierarchical architecture tailored for high-capacity and stable Na storage. The fabrication of the $CoSe_2$@CNTs-MXene composite involved a sequential process of carbonization and selenization of ZIF-67@MXene. The resulting structure is depicted in Fig. 26a, b, wherein numerous $CoSe_2$ NPs encapsulated within CNTs are neatly arranged atop the MXene substrate. When evaluated in an ether-based electrolyte, the $CoSe_2$@CNTs-MXene anode demonstrated a commendable initial Coulombic efficiency of up to 81.7 %, coupled with an exceptional cycle stability of 400 mAh g^{-1} at 2 A g^{-1} after 200 charge-discharge cycles. Furthermore, the anode displayed a noteworthy rate stability, delivering

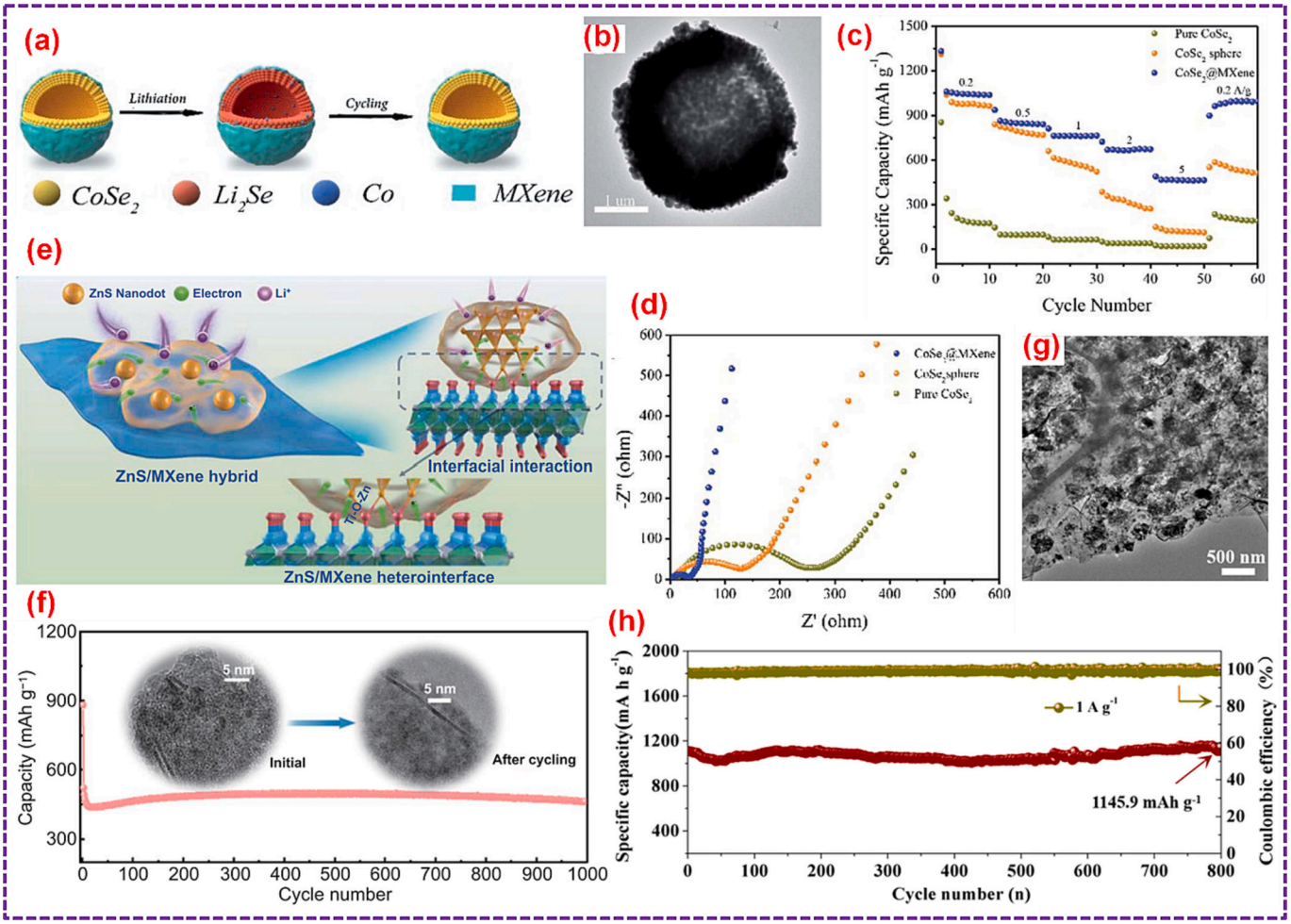

Fig. 24. (a) Pictorial representation of the stability of $CoSe_2$@MXene during the cycle performance. (b) SEM analysis of $CoSe_2$@MXene. (c) Rate capacity of the $CoSe_2$@MXene. (d) EIS analysis of various samples. Adopted with permission from Ref. [285], Copyright 2020, The Royal Society of Chemistry. (e) Pictorial representation of the electron transfer and Li-diffusion at the ZnS-MXene heterointerface. (f) Long-term cycle performance of ZnSMX64 (inset: ex-situ HRTEM analysis). Adopted with permission from Ref. [162], Copyright 2021, Springer. (g) TEM analysis of (CoS NP@NHC)@MXene. (h) Cycle performance of (CoS NP@NHC)@MXene. Adopted with permission from Ref. [89], Copyright 2021, The American Chemical Society.

a capacity retention of 347.5 mAh g^{-1} at 5 A g^{-1} (Fig. 26c, d). In a study accompanied by Wang et al. [288], a novel 2D/2D heterostructure named MXene@Co_9S_8/$CoMo_2S_4$ referred to as MXene@Co-Mo-S was proposed as an advanced solution for enhanced sodium storage. This distinctive heterostructure showcased interconnected nanosheet arrays with a porous configuration. The synthesis process of MXene@Co_9S_8/$CoMo_2S_4$ involved ion exchange followed by sulfidation of the MXene@ZIF-67 precursor, as visually depicted in Fig. 26e. The resulting morphology of the fabricated composite is presented in Fig. 26f. This unique structural design facilitated ample reaction sites and open spaces, allowing for efficient accommodation of volume variations. As a result, the MXene@Co_9S_8/$CoMo_2S_4$ heterostructure demonstrated impressive electrochemical performance, characterized by a high initial coulombic efficiency of 88.6 % and remarkable long-term cycling stability, retaining a capacity of 196 mAh g^{-1} after 350 charge-discharge cycles, as demonstrated in Fig. 26g. Li et al. [286] put forward a compelling idea that the hetero-interface effect, achieved through the integration of MOF-derived CoS_2/N-doped carbon enveloping a MXene hollow sphere referred to as MXene@CoS_2/NC, could substantially enhance the kinetics of Na^+ storage and cycle stability by adjusting the energy of Co—S bonds. The synthesis route of MXene@CoS_2/NC is shown in Fig. 26h. It involved the utilization of poly (methyl methacrylate) (PMMA) spheres as sacrificial precursors to create MXene hollow spheres, followed by the carbonization and sulfurization of PMMA@MXene@ZIF-67 to yield the final product. The resulting MXene@CoS_2/NC hollow spheres are presented in Fig. 26i. This distinct architecture not only significantly improved electrolyte penetration but also mitigated volume expansion, thereby preserving structural integrity. The MXene@CoS_2/NC composite, characterized by weakened Co—S bonds, demonstrated an exceptional capacity of 620 mAh g^{-1} at 0.2 A g^{-1} and exhibited remarkably sustained cycle capability, maintaining a capacity of 355 mAh g^{-1} even after 5000 charge-discharge cycles, as depicted in Fig. 26j.

In addition to oxides/chalcogenides, metal phosphides have also captured the attention of numerous researchers. Liu et al. [289] devised a method to synthesize sandwich-like hybrids termed MXene@CoP@N, P co-doped carbon referred to as MXene@CoP@NPC. This involved a process of low-temperature annealing and phosphorization of MXene@ZIF-L precursors, as depicted in Fig. 27a. The resulting structure, as illustrated in Fig. 27b, featured a uniform distribution of abundant CoP@NPC NPs on the MXene substrate. This arrangement served a dual purpose: preventing the agglomeration of active materials during the Na^+ insertion/extraction process and offering ample electroactive sites for redox reactions. The elevated MXene@CoP@NPC anode demonstrated a remarkable capacitance of 198 mAh g^{-1} at 5 A g^{-1} and exhibited robust cycle performance, retaining a capacity of 155 mAh g^{-1} over 1000 charge-discharge cycles as showcased in Fig. 27c.

The development of PIBs as a viable alternative to LIBs has gained

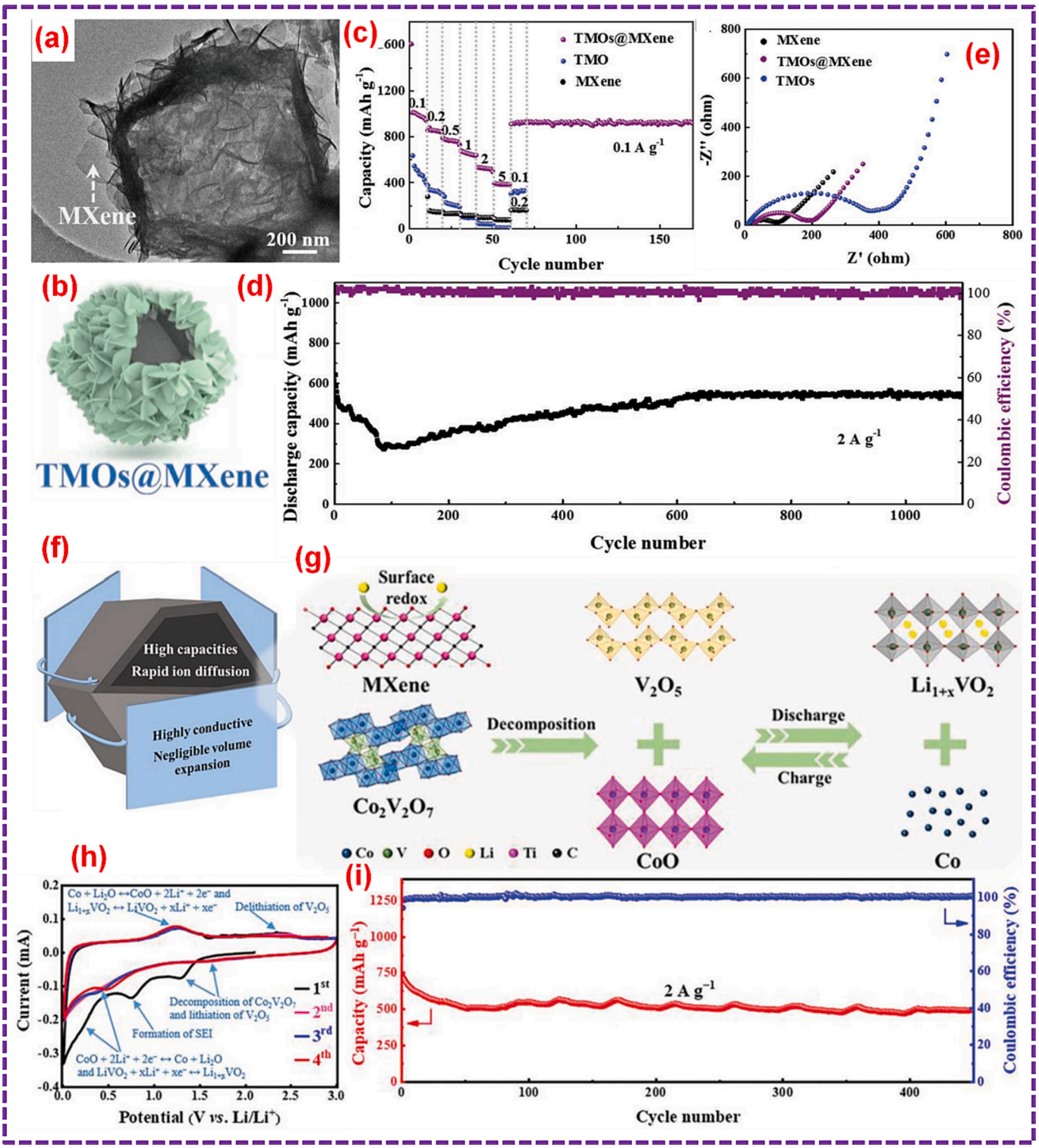

Fig. 25. (a) TEM analysis, and (b) Pictorial representation of hollow 3D CoMo LDH@MXene polyhedrons. (c) Rate capabilities and (d) Cycling behaviors of CoO/$Co_2Mo_3O_8$ @MXene electrode. (e) EIS analysis of various samples. Adopted with permission from Ref. [82], Copyright 2019, Wiley-VCH. (f, g) Schematic of the synergistic contribution of $Co_2V_2O_7$ and $Ti_3C_2T_x$ MXene. (h) The first 4 CV cycles and (i) cycling performance of CVO@MXene. Adopted with permission from Ref. [280], Copyright 2022, Wiley-VCH.

significant attention, but the search for high-performance electrodes with both high specific capacity and instant K^+ storage kinetics remains a pivotal focus in advancing PIB technology [299,300]. Within the realm of oxides/chalcogenides/phosphides of metals, metal chalcogenides stand out due to their higher conductivity, larger lattice spacing, greater density, and enhanced thermal conductivity. These properties enable swift electron mobility, improved K^+ diffusion, augmented volumetric capacities, and efficient joule heat transport. However, chalcogenides-based anodes often grapple with substantial volume changes during charge/discharge cycles, leading to the formation of a persistent solid-electrolyte interphase, electrode pulverization, and rapid capacity degradation. Addressing these challenges, Hu et al. [291] projected a

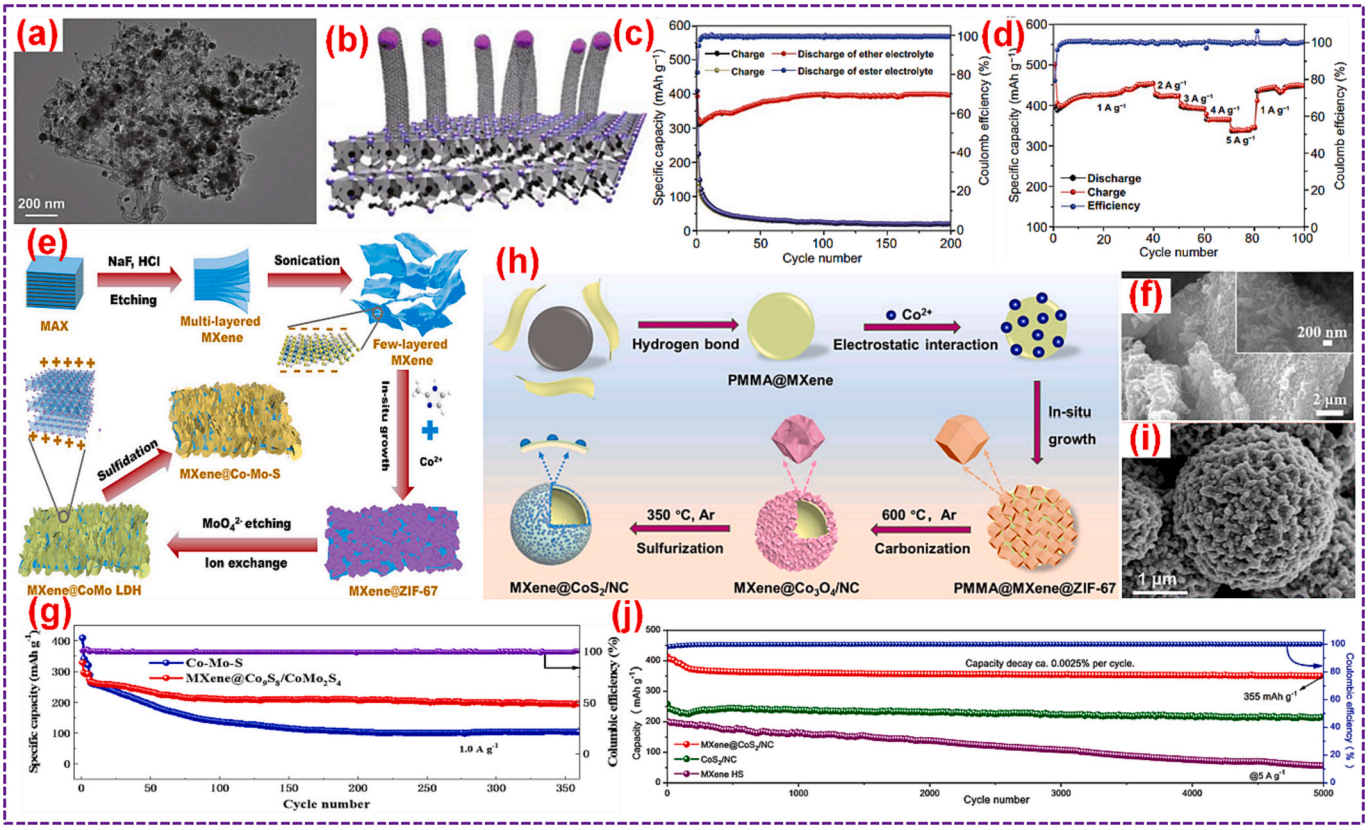

Fig. 26. (a) TEM plot and (b) Preparation protocol of $CoSe_2$@CNTs-MXene. (c) Cycle stability, and (d) rate capability of $CoSe_2$@CNTs-MXene. Adopted with permission from Ref. [287], Copyright 2021, Springer. (e) Schematic synthesis of the MXene@Co-Mo-S architecture. (f) SEM analysis and (g) cycle stability of MXene@Co-Mo-S. Adopted with permission from Ref. [288], Copyright 2022, Elsevier B.V. (h) Schematic preparation of MXene@CoS_2/NC. (i) SEM analysis and (j) long-term cycle stability of MXene@CoS_2/NC. Adopted with permission from Ref. [286], Copyright 2022, Elsevier B.V.

solution by integrating ZIF-8 derived ZnTe@C particles onto MXene to create a ZnTe@C/$Ti_3C_2T_x$ (ZCT) nanohybrid designed for exceptionally stable PIBs. The synthesis process of ZCT is depicted in Fig. 27d, while the prepared sample's morphology is shown in Fig. 27e. This structure confines ZnTe NPs within a carbon matrix derived from a MOF and interconnects them through a conductive MXene network. This unique 0D/2D dual-confinement architecture effectively mitigates the volume variation of ZnTe NPs during cycling. The elevated ZCT anode material demonstrated a notable capacity of 408 mA h g^{-1} at 0.1 A g^{-1} and exhibited prolonged cycle life with a capacity retention of 82 % after 3500 charge-discharge cycles, as illustrated in Fig. 27f.

5.2.2. Additional batteries

Rechargeable LSBs and batteries employing multivalent ions, including metals like magnesium (Mg), zinc (Zn), and aluminum (Al), have risen to prominence as highly favorable options for electrochemical energy storage systems that transcend conventional alkali metal-ion batteries. The insights presented in Table 5 provide a comprehensive overview of the recent advancements in MXene@MOF composites and their various derived materials, showcasing its remarkable progress in the realm of LSBs and multivalent ion batteries.

Rechargeable LSBs offer a capable alternate to conventional LIBs due to its remarkable theoretical capacity and environmentally friendly characteristics [307]. However, the presence of challenges such as the "shuttle effect" caused by soluble polysulfide intermediates and the formation of dendrites on Li-metal anodes presents formidable obstacles for LSBs. These challenges manifest as issues like sluggish reaction kinetics, a limited cycle lifespan, and restricted rate performance. To address these challenges, the development of functional materials with enduring durability and high electroactivity becomes imperative for facilitating the transformation of Li-polysulfides (LiPS) and ensuring optimal performance in LSBs. A novel 0D—2D heterostructure approach has emerged, exemplified by the integration of MOF-derived bimetallic selenides uniformly onto N-doped MXene (CoZn-Se@N-MX). This innovative configuration has demonstrated a significant enhancement in the conversion reaction of lithium polysulfides, showcasing promising advancements for the field [206]. Fig. 28a visually explains the fabrication and application of CoZn-Se@N-MX, while Fig. 28b portrays the characteristics of the resulting sample. This distinctive structure provides an abundance of electroactive sites for efficient LiPS transport and conversion, with the bimetallic selenides expediting the redox reactions of polysulfides and enhancing sulfur exploitation. Further validation as shown in Fig. 28c confirms the improved kinetics of polysulfide transformation in CoZn-Se@N-MX, demonstrated by its high current response, low onset potential, and minimal Tafel slope. The LSBs incorporating a S/CoZn-Se@N-MX cathode exhibit favorable rate capabilities and an extraordinary lifespan exceeding 2000 cycles (Fig. 28d). Even when subjected to a high sulfur loading of 7.8 mg cm^{-2} and a low electrolyte/sulfur (E/S) ratio of 5 μl mg^{-1}, the constructed battery demonstrates an impressive areal capacity of 6.6 mAh cm^{-2} at 0.01C (Fig. 28e).

Furthermore, an alternative approach involves the modification of polymeric separators to effectively impede the diffusion of free polysulfides between the cathode and anode. An innovative strategy was demonstrated using a $Ti_3C_2T_x$/Ni-Co MOF@PP separator, which exhibited exceptional catalytic conversion capabilities for lithium polysulfides (LiPSs) [301]. Fig. 29a visually depicts the fabrication process of the 2D/2D $Ti_3C_2T_x$/Ni-Co MOF hybrid, along with the fabricated LSB featuring the $Ti_3C_2T_x$/Ni-Co MOF@PP separator. The collaborative effect of the $Ti_3C_2T_x$/Ni-Co MOF hybrid led to the exposure of numerous

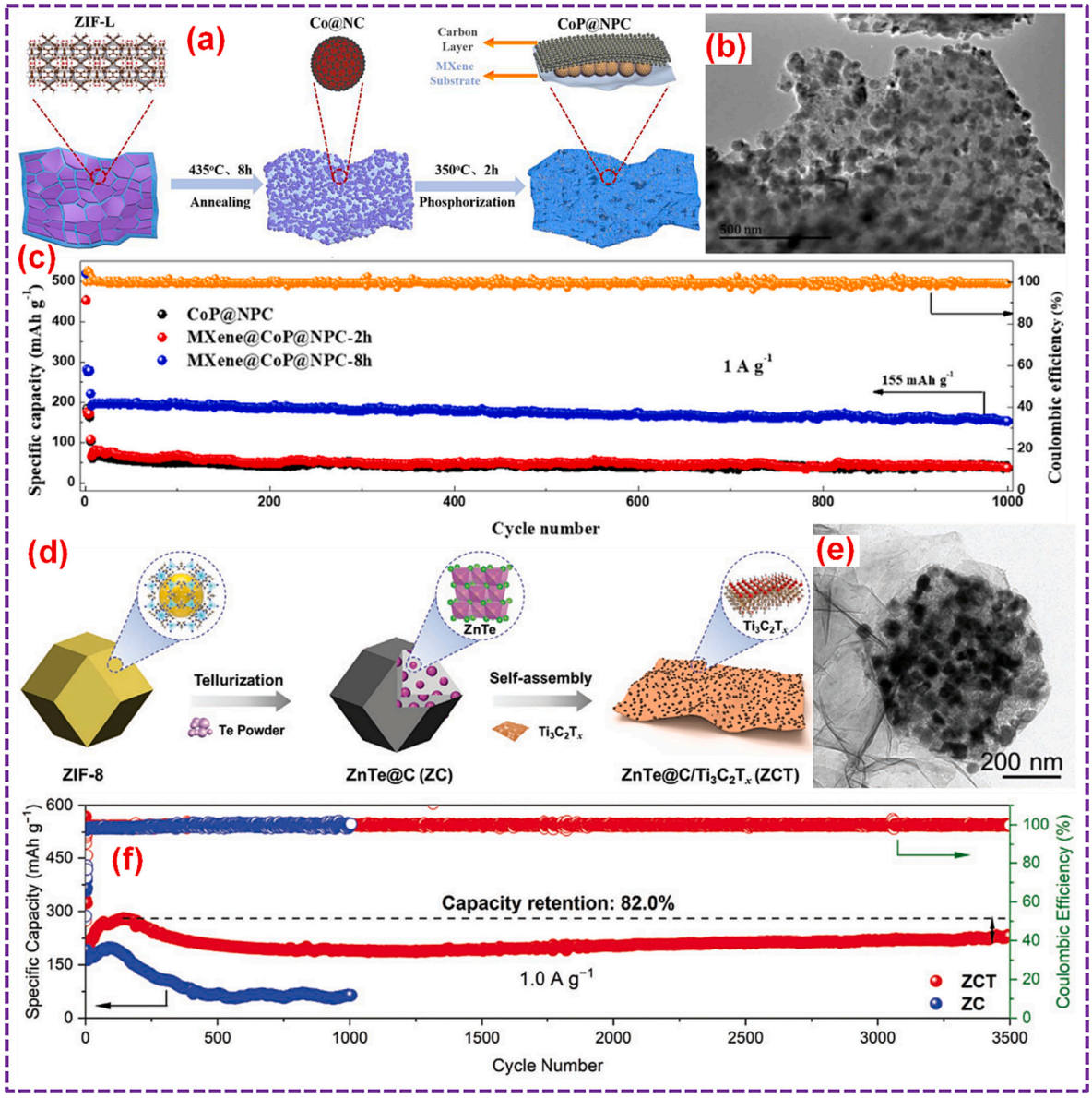

Fig. 27. (a) Pictorial representation of the MXene@CoP@NPC composite. (b) TEM analysis and (c) long term cycle stability of MXene@CoP@NPC. Adopted with permission from Ref. [289], Copyright 2022, Elsevier B.V. (d) Scheme for the preparation of ZCT nanohybrids. (e) TEM analysis and (f) cycle stability of ZCT nanohybrids. Adopted with permission from Ref. [291], Copyright 2022, Wiley-VCH.

active sites, facilitating accelerated electron/ion transfer. Consequently, this arrangement lowered the barriers to the reduction of LiPSs reduction and enhanced the Li_2S deposition. Confirmation of the improved kinetics in LiPSs conversion reactions is evident in Fig. 29b, which illustrates that the reaction free energies from S_8 to Li_2S on the $Ti_3C_2T_x$/Ni-Co MOF surface were notably lower than those observed for pure Ni—Co MOF and $Ti_3C_2T_x$ materials. The assembled LSB exhibited an impressive high-rate capacity of 1260 mAh g^{-1} (Fig. 29c) and showcased exceptional cycle stability, retaining 91.1 % of its capacity after 350 cycles. Of particular note, the practical applicability of the $Ti_3C_2T_x$/Ni-Co MOF@PP separator in LSBs was estimated using a sulfur loading of 5.8 mg cm^{-2} and an electrolyte/sulfur (E/S) ratio of 4 μl mg^{-1}. Remarkably, the constructed cell delivered an outstanding capacity of 730 mAh g^{-1} while concurrently powering multiple light-emitting diode (LED) bulbs (Fig. 29d).

The growing interest in magnesium-ion batteries (MIBs) arises from their appealing characteristics of low reduction potential, high theoretical capacity, and cost-effectiveness [308]. However, the primary challenge that MIBs face is the sluggish reaction kinetics of Mg^{2+} ions, largely attributed to the strong interaction between the highly polar magnesium ions and the cathode material. Numerous studies have proposed that metallic selenides exhibit a weak attraction to Mg due to the Mg—Se bonds formation, which facilitates rapid Mg ion reaction kinetics [309]. A significant advancement in this domain has been prepared by Zhang et al. [305], who introduced a hybridized structure by combining MOF-derived selenides with MXene to form $NiSe_2$-$CoSe_2$@$TiVCT_x$ (NCSe@TiVC), creating a high-performance and stable cycling cathode for MIBs. In their work, a disk-like bimetallic NiCo MOF morphology was co-assembled with NiCo LDH and MXene, leading to the creation of a 2D/2D heterostructure. Subsequently, a gas-phase selenization treatment was applied to the porous spherical NiCo LDH@TiVC heterostructure, resulting in the formation of NCSe@TiVC. The morphology of the resulting sample is illustrated in Fig. 30a. This distinctive structure significantly enhanced the mesopore size distribution and specific surface area, facilitating the generation of abundant active sites and promoting effective contact between the electrode

Table 5
MXene@MOF composites and their derived materials for alkali metal-ion batteries.

Material	MOF template	Application	Specific capacity	Cycle stability	Ref.
$Ti_3C_2T_x$/NiCo-BDC@PP	–	LSBs-Separator	1260 mAh g^{-1} at 0.2C	Initial discharge capacity of 1010 mAh g^{-1} and capacity decay rate of 0.025 % per cycle after 350 cycles at 0.5C	[301]
N-Ti_3C_2/C@PP	Ti_3C_2/ZIF-67	LSBs-Separator	1332 mAh g^{-1} at 0.1C	716 mAh g^{-1} after 500 cycles at 0.5C	[200]
MOFs-CoP@MXene	ZIF-67@MXene	LSBs-Cathode	854.4 mAh g^{-1} at 0.5C	796.9 mAh g^{-1} after 300 cycles at 0.2C	[278]
$Ti_3C_2T_x$/CNTs-Co_9S_8	Co-ZIF/ $Ti_3C_2T_x$	LSBs-Cathode	1389.8 mAh g^{-1} at 0.1C	730.7 mAh g^{-1} after 100 cycles at 0.2C	[302]
Fe_3Se_4/FeSe@MXene-PP	Fe-MOFs@MXene	LSBs-Separator	862.6 mAh g^{-1} at 0.2C	940.2 mAh g^{-1} after 100 cycles at 0.5C	[303]
CoZn-Se@N-MX	CoZn-MOFs@MX	LSBs-Cathode	844 mAh g^{-1} at 3C	Initial discharge capacity of 1128 mAh g^{-1} and capacity decay rate of 0.034 % per cycle after 2000 cycles at 2C	[206]
Ti_3C_2/$CoSe_2$	Ti_3C_2/ZIF-67	MIBs-Cathode	125.8 mAh g^{-1} at 0.02 A g^{-1}	96 mAh g^{-1} after 500 cycles at 0.05 A g^{-1}	[304]
$NiSe_2$-$CoSe_2$@$TiVCT_x$	NiCo-BDC	MIBs-Cathode	136 mAh g^{-1} at 0.05 A g^{-1}	96 mAh g^{-1} after 500 cycles at 0.05 A g^{-1}	[305]
Cu-HHTP/V_2CT_x	–	ZIBs-Cathode	260.1 mAh g^{-1} at 0.1 A g^{-1}	166.9 mAh g^{-1} after 1000 cycles at 4 A g^{-1}	[191]
$CoSe_2$-NPCS	MXene@ZnCo-ZIFs@PVP	AIBs-Cathode	350 mAh g^{-1} at 1.5 A g^{-1}	111 mAh g^{-1} after 5000 cycles at 2 A g^{-1}	[306]

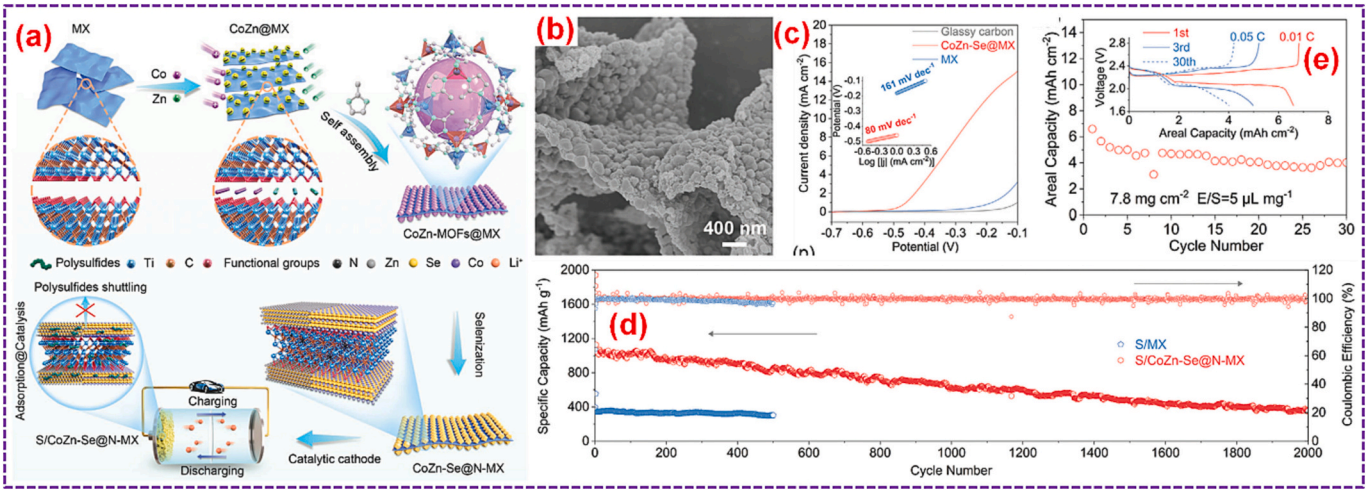

Fig. 28. (a) Synthesis of CoZn-Se@N-MX and its utilization in LSB configuration. (b) SEM analysis of CoZn-Se@N-MX. (c) LSV analysis and subsequent Tafel curves of CoZn-Se@N-MX and MX. (d) Long-term cycling stability of S/CoZn-Se@N-MX and S/MX cathodes. (e) Cycle stability of the S/CoZn-Se@N-MX cathode (inset corresponding GCD profiles). Adopted with permission from. Ref. [206], Copyright 2021, Wiley-VCH.

materials and the electrolyte. The diffusion of Mg^{2+} ions within the NCSe@TiVC cathode is depicted in Fig. 30b. Notably, the inclusion of $TiVCT_x$ MXene contributed to the enhanced stability of the crystal structure within the heterostructure, while also providing efficient pathways for ion transportation during the Mg^{2+} de-/insertion mechanism. The performance of the NCSe@TiVC cathode was exceptional, as evidenced by its significant rate capacity (Fig. 30c) and impressive cycle stability, retaining 73 mAh g^{-1} after 500 cycles. Moreover, the combination of this cathode with a magnesium foil anode was further integrated into a flexible pouch-cell device (Fig. 30d), effectively illuminating 42 red LED bulbs concurrently. This successful demonstration underscores the significant potential of the MOF-derived selenides/MXene heterostructure in flexible energy storage devices.

Zinc-ion batteries (ZIBs), centered on the insertion/extraction of Zn^{2+} ions, have garnered considerable attention as a highly promising solution for energy storage on grids. This is due to their considerable theoretical capacity, cost-effectiveness, and elevated safety levels [310,311]. While 2D MOFs featuring well-engineered porous structures and stable frameworks have emerged as top candidates for facilitating Zn^{2+} ion transport, the establishment of a more efficient mass and charge transport arrangement remains a challenge, stemming from the inherent poor conductivity associated with 2D MOFs. To address this concern, a strategy was employed wherein conductive MXene NSs were integrated into 2D Cu-HHTP MOFs, forming an alternatively stacked heterostructure that enhanced the interlayer space. This structural modification expedited the rapid insertion and extraction of Zn^{2+} ions [191]. Fig. 30e visually presents the morphology of Cu-HHTP/MX, showcasing the creation of enhanced surface areas that promote the diffusion and penetration kinetics of Zn^{2+} ions. The improved Zn^{2+} ion diffusion kinetics in Cu-HHTP/MX is validated in Fig. 30f, where Cu-HHTP/MX exhibited a lower Zn^{2+} adsorption energy compared to the unmodified Cu-HHTP. The operational mechanism of the Zn//Cu-HHTP/MX battery is elucidated in Fig. 30g. Leveraging the remarkable Zn^{2+} adsorption capability of the Cu-HHTP/MX anode, the resultant ZIB demonstrated exceptional rate capabilities (Fig. 30h) alongside an impressive cyclic performance exceeding 1000 cycles. Aluminum-ion batteries (AIBs) have emerged as a promising avenue for high-energy rechargeable battery systems, primarily attributed to their exceptional theoretical volumetric capacity and impressive electrical characteristics [312]. Nonetheless, the research progress of AIBs has been impeded by the sluggish redox reaction kinetics arising from the larger size of $Al_xCl_y^-$ species. To overcome this challenge, the exploration of cathode

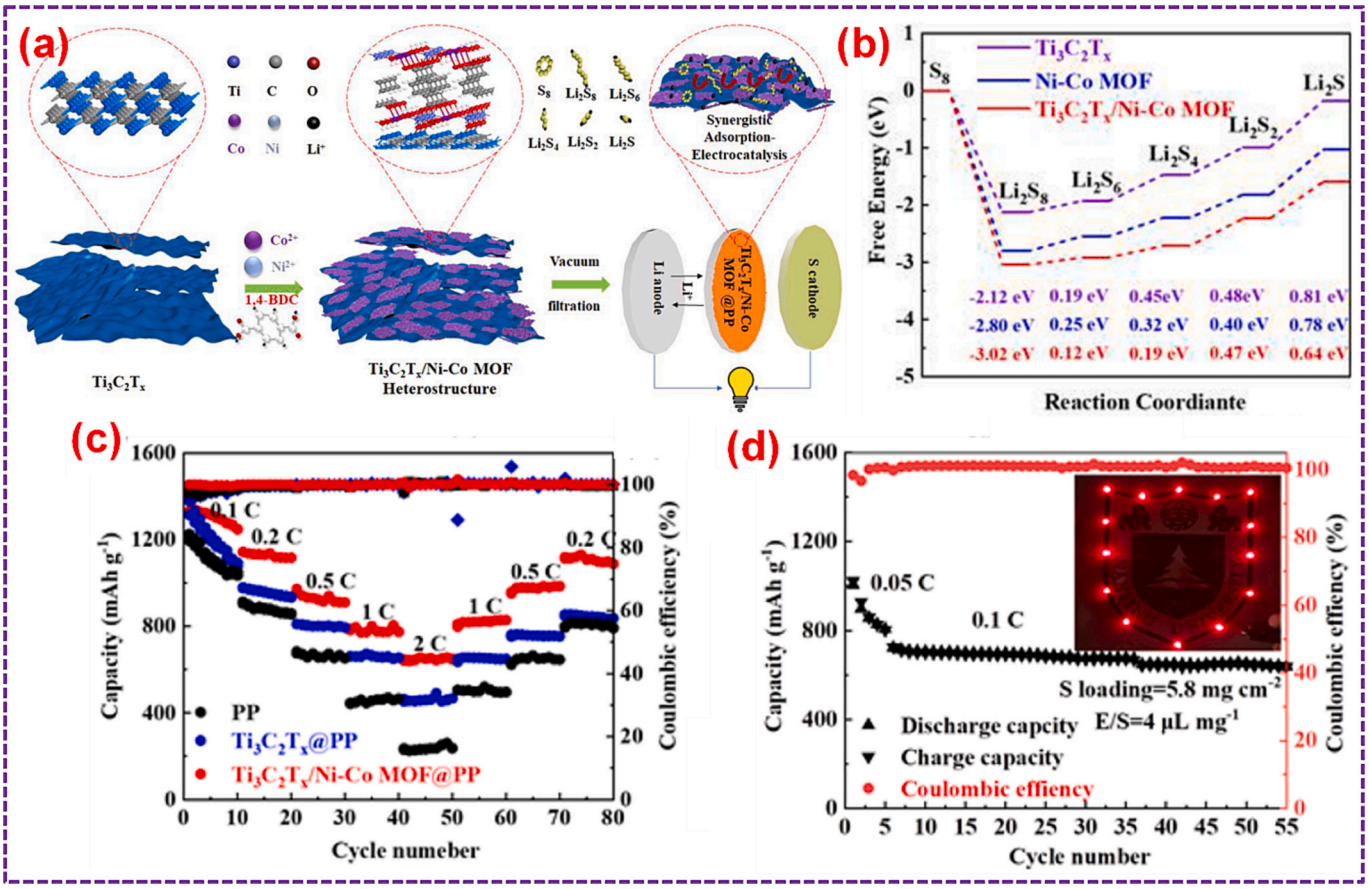

Fig. 29. (a) Scheme for the preparation of the 2D/2D $Ti_3C_2T_x$/Ni-Co MOF heterostructure. (b) Relative free energy for the discharging mechanism from S_8 to Li_2S on the $Ti_3C_2T_x$, Ni—Co MOF and $Ti_3C_2T_x$/Ni-Co MOF surfaces. (c) Rate performance of Li—S batteries with PP, $Ti_3C_2T_x$@PP, and $Ti_3C_2T_x$/Ni-Co MOF@PP separator. (d) Cycle stability of $Ti_3C_2T_x$/Ni-Co MOF@PP (inset photograph of LEDs powered by $Ti_3C_2T_x$/Ni-Co MOF@PP LSB). Adopted with permission from Ref. [301], Copyright 2022, Elsevier B.V.

materials with enhanced ion diffusion and support for volume fluctuations during cycling becomes essential. A pivotal solution lies in the utilization of hierarchical porous structures that furnish an abundance of interconnected channels, thereby expediting ion diffusion and facilitating the immersion of electrolyte. Additionally, these structures provide effective vacant spaces to accommodate volume changes during the charge/discharge cycle process. Yao and his group [306] illustrated the efficacy of $CoSe_2$ NPs integrated into hierarchical porous nitrogen-doped carbon NSs ($CoSe_2$-NPCS) in exhibiting exceptional Al^{3+} diffusion kinetics and structural stability. In their study, Zn-doped ZIF-67 was amalgamated with PVP (polyvinyl pyrrolidone) and MXene to prepare MXene@ZIFs@PVP NSs, which were subsequently subjected to carbonization and selenization to yield $CoSe_2$-NPCS. As shown in Fig. 30i, the resulting sample showcased a distinctive 2D lamellar porous structure, enabling electrolyte immersion and facile diffusion of Al_xCl_y species. The presence of this unique structure, along with ultrafine $CoSe_2$ particles, empowered the $CoSe_2$-NPCS electrode to attain high-rate capability of 122 mA h g^{-1} at 5 A g^{-1} (Fig. 30j), accompanied by remarkable cycle stability of 111 mA h g^{-1} even after 5000 cycles. Comparative analysis with $CoSe_2$-NCS fabricated using MXene@Co-ZIF@PVP as precursors and $CoSe_2$-NC derived from Co-ZIF@PVP precursors revealed that $CoSe_2$-NPCS exhibited superior Al^{3+} diffusion kinetics, evident from the steeper slope of the Warburg coefficient curves depicted in Fig. 30k. Remarkably, the introduction of nitrogen atoms via the N-C/MXene hybrid improved the interfacial interactions between the MXene substrate and Co species (Fig. 30l), thereby enhancing reaction kinetics and bolstering long-term cycling performance.

5.3. Electrocatalysis

Given the escalating global demand for renewable and environmentally sustainable energy sources, the pursuit of advanced energy materials for efficient and ecologically friendly chemical energy conversion is imperative. Among the vital processes in sustainable energy systems, the oxygen evolution reaction (OER), hydrogen evolution reaction (HER), oxygen reduction reaction (ORR), and carbon dioxide reduction reaction (CO_2 RR) hold paramount significance. Notably, water splitting embodies an eco-friendly and scalable means of converting solar energy into storable hydrogen fuel, encompassing the pivotal half-reactions of OER and HER. Furthermore, in the realm of fuel cells that convert the chemical energy of various fuels into electricity, the oxygen reduction reaction (ORR) stands as a core reaction. Within this context, our focus centers on the advancement of MXene@MOF composites and their derived materials as electrocatalysts in crucial electrocatalytic energy conversion reactions, which encompass the OER, HER, and ORR processes as illustrated in Table 6.

5.3.1. OER

The oxygen evolution reaction (OER) characterized by complex 4-electron pathways often exhibits sluggish kinetics and requires high overpotentials for initiation. While catalysts based on precious metals such as RuO_2 and IrO_2 demonstrate exceptional activity in driving the OER, their scarcity and elevated costs hinder widespread commercial utilization. Consequently, the exploration of electrocatalysts that offer both high efficiency and cost-effectiveness remains an ongoing pursuit. In this context, MXene@MOF based composite materials have emerged

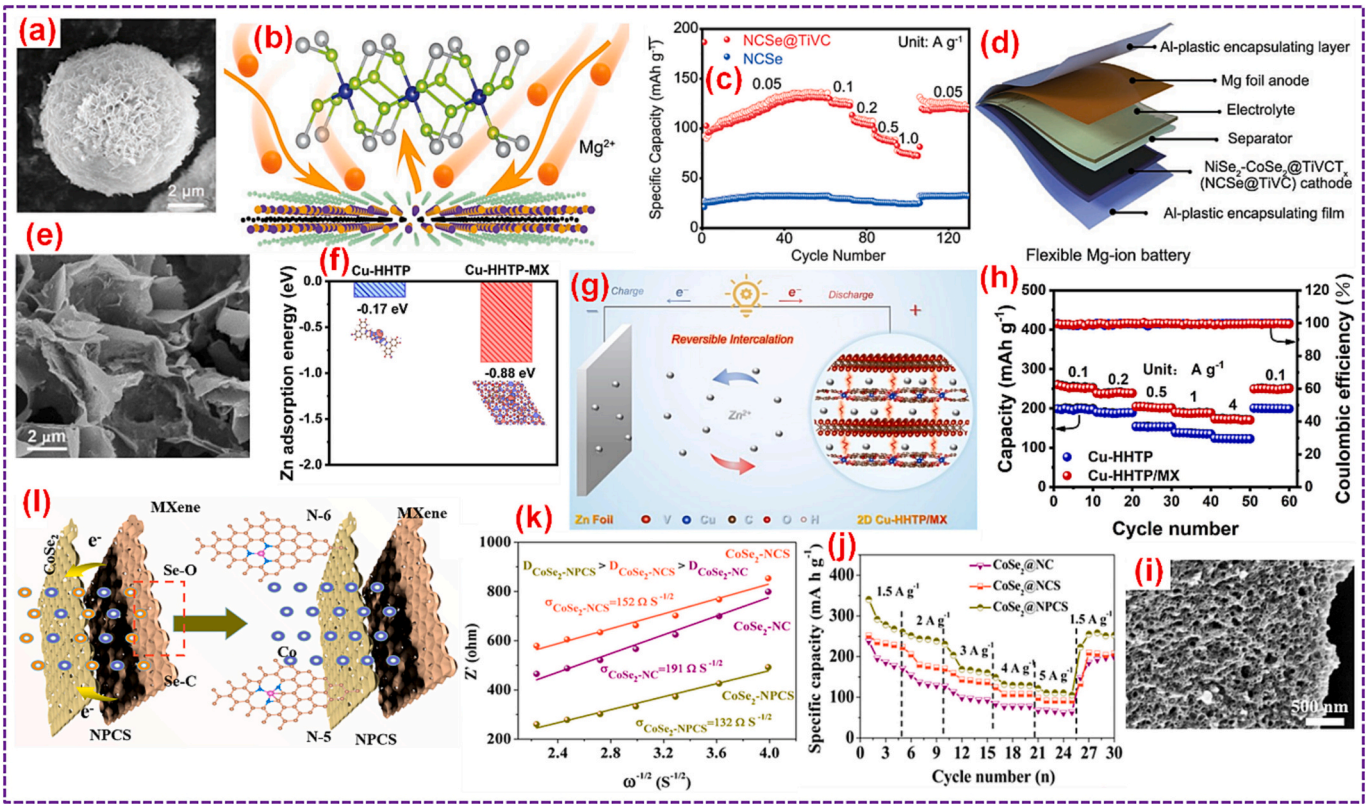

Fig. 30. (a) SEM image of NCSe@TiVC. (b) Scheme for the Mg^{2+} diffusion within the NCSe@TiVC cathode. (c) Rate capabilities of NCSe@TiVC. (d) Pictorial representation of the NCSe@TiVC-based MIBs. Adopted with permission from Ref. [305], Copyright 2022, Wiley-VCH. (e) SEM analysis, and (f) Zn^{2+} adsorption energy of Cu-HHTP/MX. (g) The Zn/Cu-HHTP/MX battery mechanism. (h) Rate capabilities of Cu-HHTP/MX. Adopted with permission from Ref. [191], Copyright 2022, Wiley-VCH. (i) SEM analysis, (j) Rate capabilities, and (k) Warburg coefficient plots of $CoSe_2$-NPCS. (l) Mechanism of the Co controlled by $CoSe_2$-NPCS. Adopted with permission from Ref. [306], Copyright 2021, The American Chemical Society.

Table 6
MXene@MOF composites and their derived materials for electrocatalysis field.

Sample	Precursor	Application	Over potential/half wave potential (mV)	Tafel slope (mV dec^{-1})	Electrolyte	Ref.
Co BDC/MXene	–	HER	29/–	46	1 M KOH	[313]
Co BDC/MXene	–	HER	76/–	71	1 M PBS	[313]
Co BDC/MXene	–	HER	41/–	59	0.5 M H_2SO_4	[313]
Ti_2NT_x@MOF-CoP	Ti_2NT_x/ZIF-67	HER	112/–	79.1	1 M KOH	[218]
Ti_2NT_x@MOF-CoP	Ti_2NT_x/ZIF-67	HER	131/–	125.6	1 M PBS	[218]
Ti_2NT_x@MOF-CoP	Ti_2NT_x/ZIF-67	HER	129/–	96.7	0.5 M H_2SO_4	[218]
CoO_x-N-C/TiO_2C	CoZn-ZIF/$Ti_3C_2T_x$	HER	67.8	134	0.1 M KOH	[87]
MoNiS/$Mo_2TiC_2T_x$	Ni-MOF/$Mo_2TiC_2T_x$	HER	153/–	92	1 M KOH	[314]
Ru@ZIF-L (Co)/$Ti_3C_2T_x$	ZIF-L (Co)/$Ti_3C_2T_x$	HER	16.2/–	21	1 M KOH	[233]
FeP-CoP/$Ti_3C_2T_x$	FeCo-PBA/ $Ti_3C_2T_x$	OER	270/–	49.1	1 M KOH	[315]
$Ti_3C_2T_x$-CoBDC	–	OER	1640/–	48.2	0.1 M KOH	[78]
CoNi-ZIF-67@ $Ti_3C_2T_x$	–	OER	275/–	65.1	0.1 M KOH	[179]
Co_3O_4/Co_2TiO_4	Co-BDC/ $Ti_3C_2T_x$	OER	280/–	66.4	1 M KOH	[316]
Co_2Ni-MOF@MX	–	OER	265/–	51.7	1 M KOH	[102]
CoFe LDH/Ti_3C_2/NF	ZIF-67/Ti_3C_2/NF	OER	170/–	31.5	1 M KOH	[235]
NF/$Ti_2VC_2T_x$@C, N-Co_2P	NF/$Ti_2VC_2T_x$@Co-MOF	OER	246/–	28.2	1 M KOH	[317]
Fe-N-C@$Ti_3C_2T_x$	Fe doped ZIF-8	ORR	–/887	88	0.1 M KOH	[225]
Fe-N-C@$Ti_3C_2T_x$	Fe doped ZIF-8	ORR	–/777	78	0.1 M $HClO_4$	[225]
CoO_x-N-C/TiO_2C	CoZn-ZIF/$Ti_3C_2T_x$	ORR	–/850	–	0.1 M KOH	[87]
CoZn/NC-Ti_3C_2	CoZn-ZIF/Ti_3C_2	ORR	–/847	95	0.1 M KOH	[318]
Co-CNT/Ti_3C_2	ZIF-67/Ti_3C_2	ORR	–/820	63	0.1 M KOH	[168]

as novel contenders for OER electrocatalysis, attributed to their porous structures, excellent conductivity, extensive active surfaces, and pronounced hydrophilicity. These attributes contribute to efficient aqueous electrolyte immersion and rapid charge transfer. The inception of MXene@MOF composite electrocatalysts dates back to 2017, marked by the introduction of the well-defined $Ti_3C_2T_x$-CoBDC system. This composite demonstrated an overpotential of 1.64 V at 10 mA cm^{-2} and a low Tafel slope of 48.2 mV dec^{-1} in a 0.1 M KOH electrolyte [78]. Furthermore, the coupling of bimetallic Co_2Ni-MOF NSs with MXene yielded remarkably electroactive catalysts, exhibiting a Tafel slope of 51.7 mV dec^{-1} and a reduced overpotential of 265 mV. It is noteworthy that both $Ti_3C_2T_x$-CoBDC and Co_2Ni-MOF@MX outperformed pristine MXene and unmodified MOFs in terms of electrocatalytic performance [319]. Concurrently, a strategic approach involves the deliberate

transformation of unmodified MOFs into derivatives, effectively yielding OER electrocatalysts with tailored performance characteristics. The robust electronic coupling synergy between MXene and MOF-derived materials serves to fine-tune the intrinsic catalytic activity while also modulating the interaction tendencies of OER intermediates. Illustratively, the work by Hu et al. [235] introduced electronic optimization to MOF-derived LDH NS arrays through the facilitation of MXene's induction effect. As depicted in Fig. 31a, the CoFe LDH/Ti_3C_2 composite was engineered, where Ti_3C_2 NSs initially coated a nanofiber substrate (NF) to serve as a foundation for ZIF-67 deposition. Subsequently, the ZIF-67/Ti_3C_2/NF precursor underwent an etching-precipitation procedure to produce CoFe LDH/Ti_3C_2/NF. The resultant CoFe LDH/Ti_3C_2 exhibited a hierarchical structure with well-exposed active areas, thus favoring the transport of species relevant to the OER process, as illustrated in Fig. 31b. This catalyst demonstrated remarkable OER performance, showcasing an overpotential of 170 mV and a Tafel slope of 31.5 mV dec^{-1} (Fig. 31c, d). In a similar vein, MOF-derived C,N-doped porous Co_2P was immobilized onto $Ti_2VC_2T_x$ MXene to enhance OER efficiency [320]. Fig. 31e delineates the fabrication process, where $Ti_2VC_2T_x$ NSs coated an NF for the electrodeposition of Co-LDH. The generated Co-LDH underwent conversion into Co-MOFs, which were then phosphorized. This sequence yielded the MX@C, N-Co_2P catalyst, characterized by an interconnected porous sheet type structure featuring abundant active sites (Fig. 31f). The distinctive structure, combined with the synergistic interplay between C, N-Co_2P and MXenes, enabled the catalyst to attain a low overpotential of 246 mV and an ultra-low Tafel slope of 28.2 mV dec^{-1} (Fig. 31g, h).

Furthermore, the integration of MOF-derived Ni-Co-mixed metal

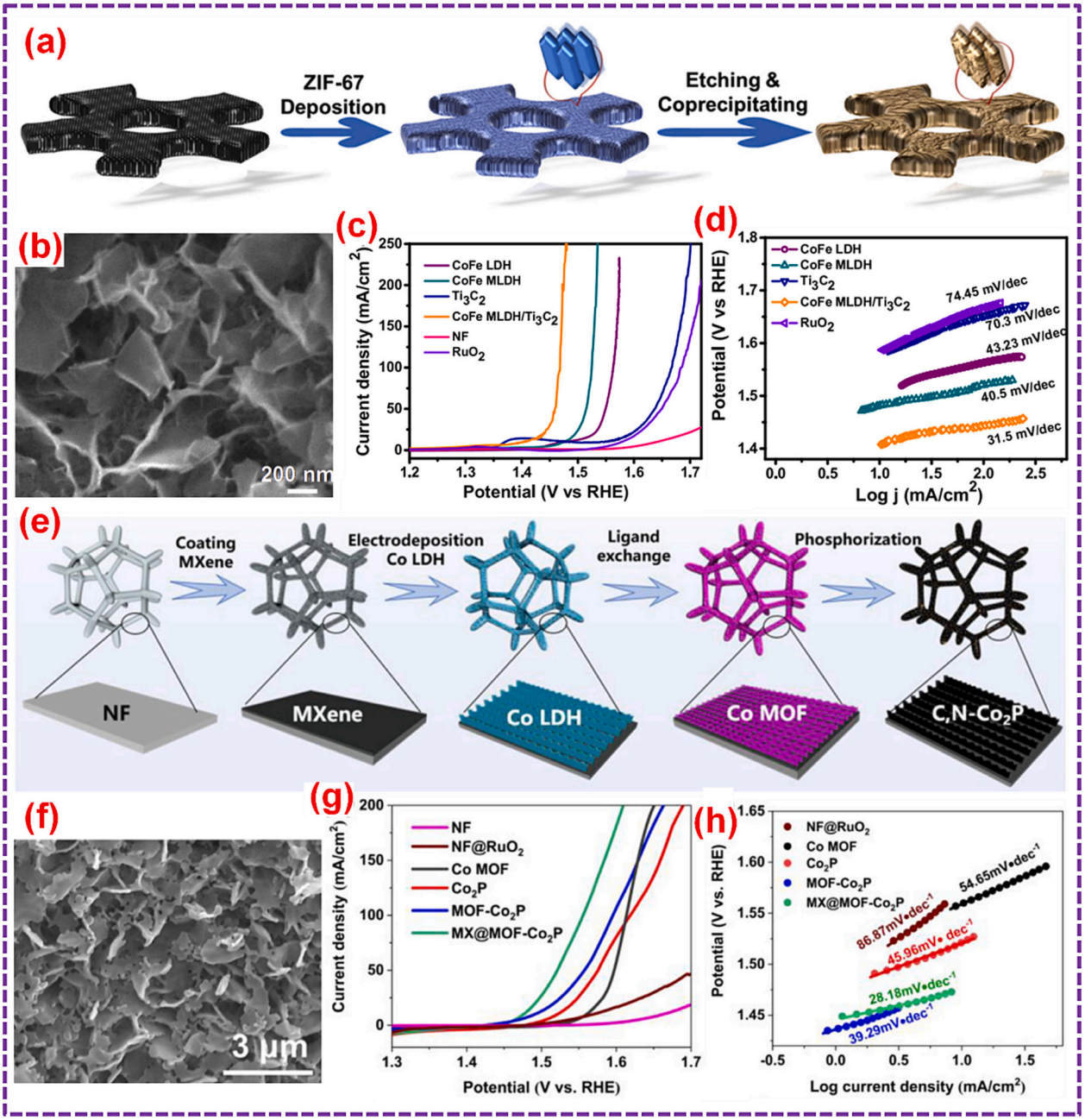

Fig. 31. (a) Schematic preparation of CoFe LDH/Ti_3C_2. (b) SEM analysis of CoFe LDH/Ti_3C_2. (c) OER polarization plots and (d) Tafel plots of CoFe LDH/Ti_3C_2. Adopted with permission from Ref. [235], Copyright 2021, Elsevier B.V. (e) Schematic preparation of MX@C,N-Co_2P. (f) SEM images of MX@C,N-Co_2P. g) OER polarization plots and h) Tafel plots of MX@C,N-Co_2P. Adopted with permission from Ref. [320] Copyright 2022, Elsevier B.V.

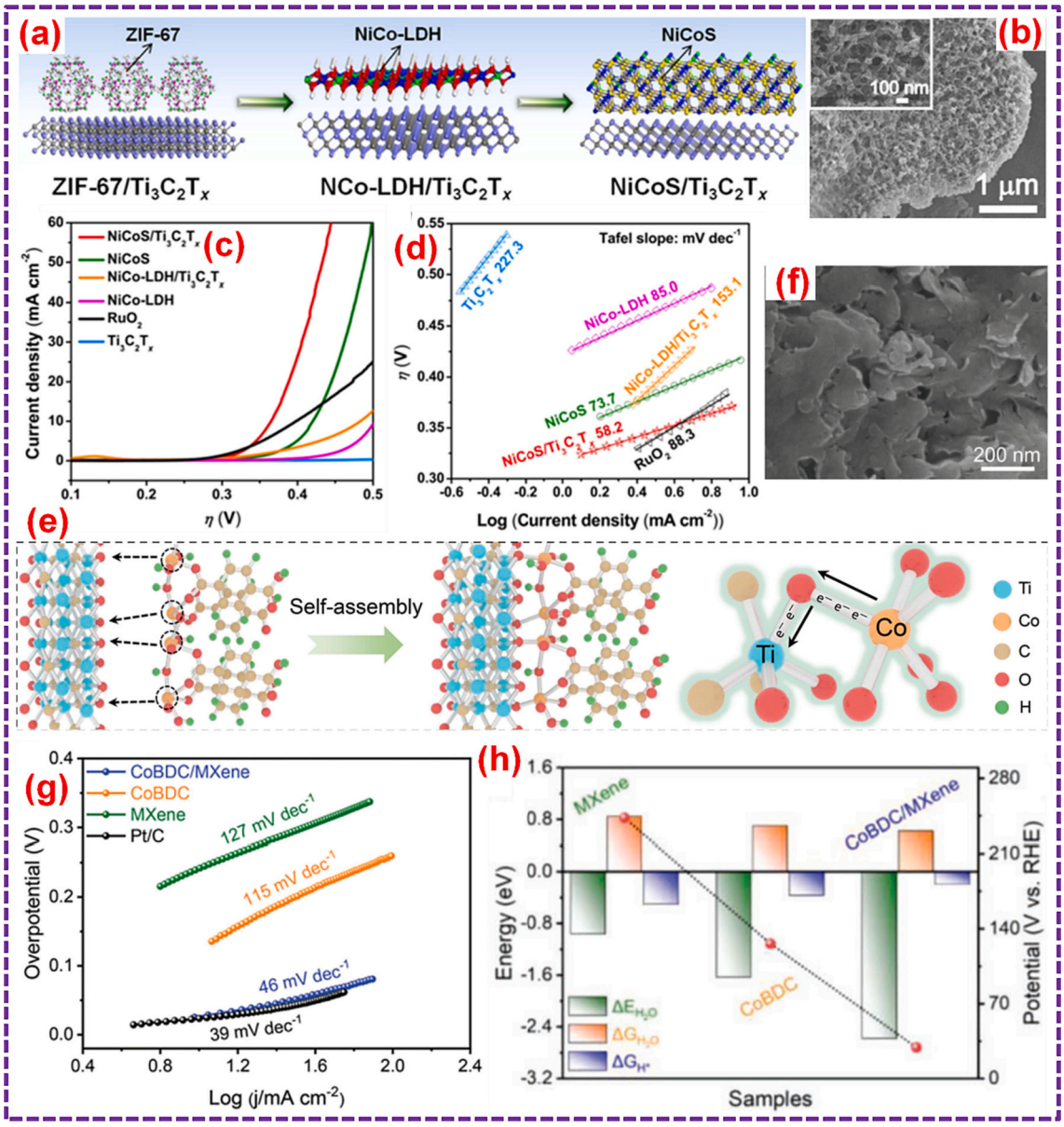

Fig. 32. (a) Schematic synthesis of NiCoS/$Ti_3C_2T_x$. (b) SEM images of NiCoS/$Ti_3C_2T_x$. (c) OER polarization plots and (d) Tafel plots of NiCoS/$Ti_3C_2T_x$. Adopted with permission from Ref. [215], Copyright 2018, The American Chemical Society. (e) Scheme for the synthesis and charge transport of CoBDC/MXene with interfacial Co-O-Ti bridging. (f) SEM analysis of CoBDC/MXene. (g) Tafel curves for various materials. (h) The correlation among the evaluated adsorption energy of H_2O (ΔE_{H2O}), dissociation free energy of H_2O (ΔG_{H2O}), and free energy of adsorbed H* intermediates (ΔG_{H^*}). Adopted with permission from Ref. [313], Copyright 2022, Wiley-VCH.

sulfide onto $Ti_3C_2T_x$ (NiCoS/ $Ti_3C_2T_x$) was found to exhibit superior OER activity. [215] Fig. 32a outlines the fabrication process, while Fig. 32b showcases the morphological attributes of the resulting catalyst. The distinctive hierarchical porous structure, coupled with strong interactions in NiCoS/$Ti_3C_2T_x$, contributed to an expanded active area and elevated conductivity. This composite catalyst showcased commendable OER activity, manifesting an overpotential of 365 mV and a Tafel slope of 58.2 mV dec^{-1} (Fig. 32c, d).

5.3.2. HER

HER stands as another pivotal energy conversion mechanism essential for advancing the sustainable development of H_2 fuel. Ru-based catalysts have earned significance in HER due to their inherent remarkable electrocatalytic capabilities [168,321]. However, the synthesis process of catalysts involving Ru NPs tends to lead to aggregation. A promising strategy involves the creation of well-dispersed Ru nanoclusters to enhance HER activity. In this context, Luo et al. [233] engineered ultrafine Ru NPs embedded within leaf-shaped ZIF-L (Co)/$Ti_3C_2T_x$ composites, leading to exceptional HER performance in alkaline media. The resultant Ru@ZIF-L(Co)/FL-$Ti_3C_2T_x$ catalyst demonstrated superior catalytic efficiency, presenting an overpotential of 16.2 mV and a Tafel slope of 21 mV dec^{-1}. Notably, this catalyst outperformed Ru@ZIF-L (Co), underscoring the role of $Ti_3C_2T_x$ in amplifying fast charge transfer kinetics. Despite the evident superiority of noble metal-based electrocatalysts, the substantial expense associated with their production remains a limiting factor. Hence, there exists a need to investigate cost-effective alternatives, such as electrocatalysts based on earth-abundant metals, to address this concern. As an illustration, Wang et al. [313] orchestrated the fabrication of a 2D/2D heterostructure by on-site cultivation of CoBDC NSs atop MXene NSs to achieve proficient HER performance. In the CoBDC/MXene structure, the formation of interfacial Co-O-Ti bridges facilitated accelerated charge and ion

transport, culminating in heightened electrocatalytic activity depicted in Fig. 32e, f. This assertion is further substantiated by Fig. 32g, wherein the optimized HER reaction energy barrier of CoBDC/MXene underlines its enhanced catalytic action. The catalytic prowess of CoBDC/MXene was estimated across alkaline, acidic, and neutral electrolytic environments, showcasing minimal overpotentials of 29, 41, and 76 mV, respectively (Fig. 32h). In a similar vein, Ti_2NT_x-wrapped MOF-derived CoP heterostructures were engineered to achieve remarkable HER capabilities [218]. The synthesized Ti_2NT_x@MOF-CoP catalyst exhibited notably low overpotentials of 112 mV, 131 mV, and 129 mV in alkaline, neutral, and acidic contexts, respectively. The improved HER activity of Ti_2NT_x@MOF-CoP, in contrast to MOF-CoP, underscores the augmentation in available surface areas and the enhanced stability of heterojunction electrocatalysts. Moreover, MOF-derived bimetallic NiMo-based sulfide coupled with $Mo_2TiC_2T_x$ was harnessed as an efficient electrocatalyst for HER [314]. The heterojunction between MOF-derived Ni_2S and $MoS_2/Mo_2TiC_2T_x$ engendered a synergistic effect, optimizing the electronic structure. The resulting $MoNiS/Mo_2TiC_2T_x$ catalyst outperformed MOF-derived NiS and $MoS_2/Mo_2TiC_2T_x$ counterparts, attesting to its superior HER performance, catalytic efficacy, and exceptional stability.

5.3.3. ORR

The ORR assumes a pivotal role in renewable energy technologies, such as fuel cells and metal-air batteries. MOF-derived electrocatalysts, characterized by high surface area and an abundance of electroactive sites, hold significant promise in enhancing ORR kinetics. Nonetheless, challenges concerning aggregation and limited stability persistently confront these catalysts [322]. As a potential solution, the integration of highly conductive MXene has been proposed to counteract the aggregation and structural instability issues inherent in MOF-derived electrocatalysts. Exemplifying this approach, Wang et al. [225] demonstrated the superior ORR activity of MOF-derived Fe-N-C following its hybridization with few-layered $Ti_3C_2T_x$. The introduced MXene not only facilitated more efficient electron transfer pathways but also safeguarded the structural integrity of Fe-N-C. The resulting Fe-N-C@$Ti_3C_2T_x$ composite exhibited remarkable ORR efficiency across both alkaline and acidic electrolytes. In a 0.1 M KOH electrolyte, the catalyst displayed a half-wave potential of 0.887 V and maintained this performance even after 10,000 cycles. Likewise, in a 0.1 M $HClO_4$ electrolyte, the catalyst demonstrated a half-wave potential of 0.777 V, with only a minor 11 mV decrease following 10,000 cycles. Moreover, MOF-derived Co-tipped CNTs were shown to enhance ORR kinetics, aided by the incorporation of MXene NSs [168]. The inclusion of Ti_3C_2 during the pyrolysis of pristine MOF led to a higher degree of carbon graphitization, thereby enhancing the conductivity of Co-CNT/Ti_3C_2, and promoting electron transfer kinetics. The optimized Co-CNT/Ti_3C_2 composite showcased a low half-wave potential of 0.82 V and a substantial diffusion-limiting current density of 5.30 mA cm^{-2}.

5.3.4. Carbon dioxide reduction reaction

Due to the substantial emissions of carbon dioxide (CO_2) from the

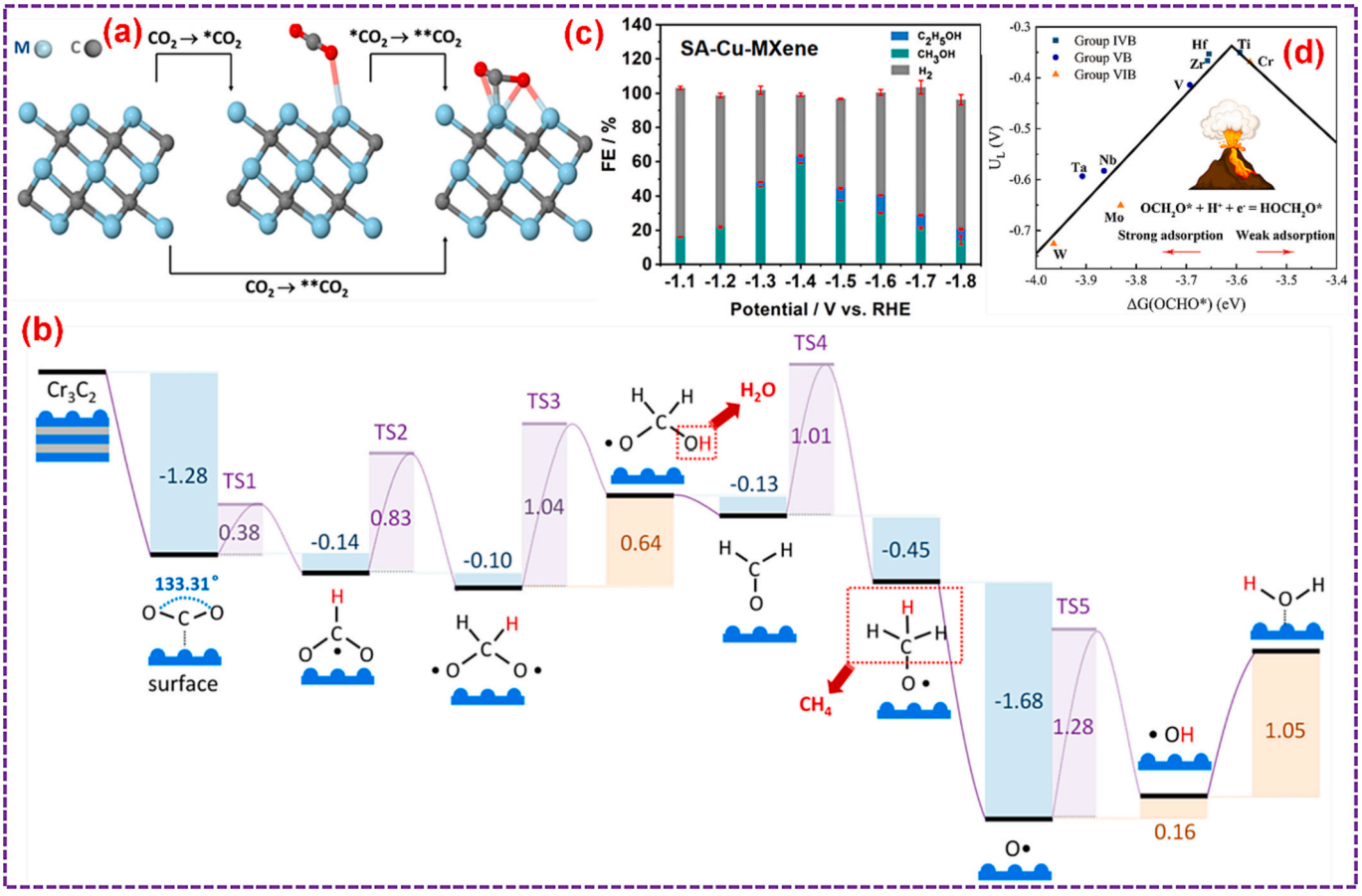

Fig. 33. (a) The metal surfaces of MXenes adsorb CO_2 through physical adsorption, chemisorption, and interaction. "M and C" refer to octahedral coordination transition metals and carbon atoms, respectively; The * and ** symbols denote substances that are physically and chemically absorbed, respectively. (b) O^- and OH^- functionalized Cr_3C_2 and Mo_3C_2 MXenes can significantly reduce the energy barrier of CO_2 conversion to CH_4. Adopted with permission from Ref. [324], Copyright 2017, The American Chemical Society. (c) FEs of SA-Cu-MXene. Adopted with permission from Ref. [325], Copyright 2021, The American Chemical Society. (d) The CO_2 RR volcano plot of Mo_3C_2 and TM-substituted bimetal MXenes. OCHO* represents the possible products of hydrogenation. Adopted with permission from Ref. [326], Copyright 2022, Elsevier B.V.

combustion of fossil fuels, there has been a surge in global climate change. The electrocatalytic CO_2 reduction reaction (RR) is seen as a promising method for converting CO_2 into valuable materials and fuels [323]. MXenes and MXene-based materials, known for their high electrical conductivity and tunable structures, are considered potential electrocatalysts for CO_2 RR. For instance, Cr_3C_2 and Mo_3C_2 MXenes have been proposed for the selective conversion of CO_2 to CH_4. The metal-terminated surfaces of MXenes adsorb CO_2 initially through physical adsorption and subsequently via chemisorption/interaction, as illustrated in Fig. 33a. Specifically, the O^- and OH^- functionalized Cr_3C_2 and Mo_3C_2 MXenes can significantly reduce the energy barrier for the conversion of CO_2 to CH_4, as depicted in Fig. 33b [324]. Zhao et al. demonstrated the selective etching of the Al layer in a four-element MAX (A = Al and Cu) to obtain accordion-shaped Cu-$Ti_3C_2Cl_x$, where Cu atoms predominantly formed coordination with the MXene surface in the form of Cu—O coordination [325]. Cu-$Ti_3C_2Cl_x$ exhibited high selectivity for methanol in the electrocatalytic CO_2 reduction process, with an optimal Cu content of 2 wt%. The Faradaic efficiency reached 59.1 % at −1.4 V, with a charge-transfer resistance (CdI) of 9.7 mF cm^{-2} and stable current density, as illustrated in Fig. 33c. Furthermore, the Faradaic efficiency could be maintained at around 58 %, and after a stability test of 30 h, the material was found to be resistant to oxidation. This was attributed to dispersed Cu atoms inhibiting the C—C coupling of C1 intermediates such as *CO, reducing the formation of C^{2+} products like ethanol. Additionally, the electronic structure of single-atom Cu is unsaturated. Bharath et al. designed a Pd50-Ru50/$Ti_3C_2T_x$ catalyst for CO_2 electrocatalytic hydrogenation, exhibiting high selectivity towards methanol products at low temperatures with a methanol yield of approximately 76 % [325]. At a catalyst loading of 20 mg, the maximum conversion rate of CO_2 was about 78 %, and the total turnover number (TON) reached 2932. This was attributed to the loading of Pd50-Ru50 on $Ti_3C_2T_x$, effectively preventing the aggregation of Pd50-Ru50, while Pd50-Ru50 prevented the aggregation of MXene. The mesoporous structure formed by the combination of Pd50-Ru50 and $Ti_3C_2T_x$ had a high specific surface area (120 m^2 g^{-1}), exposing more active sites. It was also found that extending the reaction time led to formic acid formation, promoting methanol production. In contrast to previous studies on single-atom metal-doped MXene, Li et al. investigated the electrocatalytic reduction of CO_2 by substituting Mo in Mo_3C_2 with Ti, Zr, Hf, V, Nb, Ta, Cr, and W [326]. Complete substitution of the interlayer resulted in the best catalytic performance for CO_2 reduction, with highly selective methane synthesis and suppression of competing reactions with water reduction. Among them, Mo_2TiC_2 exhibited the best electrocatalytic performance for CO_2 RR, lowering the limiting potential of MXene from −0.651 to −0.350 V, as shown in Fig. 33d. This improvement can be attributed not only to the disruption of linear scaling relationships between intermediate adsorption energies caused by transition metal doping, severely hindering catalytic efficiency, but also to the presence of Ti, which provides Mo with stronger localized lone-pair states.

6. Conclusions and outlook

This comprehensive review systematically delves into the preparation methodologies of MXene@MOF composites, along with the derivation processes of MXene@MOF-derived materials. Subsequently, a comprehensive analysis and summarization of the crucial electrochemical applications of both MXene@MOF composites and their derived materials are provided, encompassing SCs, alkali metal-ion batteries, multivalent ion batteries, LSBs, water splitting, and ORR. The incorporation of MXene proves highly effective in mitigating the chemical instability and low electron conductivity inherent in MOFs. In a reciprocal manner, the pronounced oxidation degradation and tendency to self-stack observed in MXene can be effectively mitigated through the integration of MOFs. A multitude of investigations underscore the enhanced electrochemical properties exhibited by MXene@MOF composites in comparison to pure MXene and pristine MOFs. This superiority can be attributed to meticulously engineered structures, robust interfacial interactions, abundant active sites, and well-connected conductive pathways. Furthermore, the coupling of MXene with diverse functional MOF-derived nanomaterials, such as LDHs, oxides/chalcogenides/phosphides of metal, and metal/carbon hybrids, has demonstrated impressive success in delivering significantly heightened electrochemical performance. The synergistic combination of these materials yields remarkable enhancements in specific capacities, rate performance, cycling stability, Tafel slopes, and more. This underscores the pivotal roles played by well-designed structures, robust interfacial interactions, ample active sites, and outwardly accessible conductive pathways in driving superior electrochemical attributes.

While substantial strides have been taken in the realm of MXene@MOF composites and their derived materials, their application within the electrochemistry domain remains in its nascent stages. To foster more robust progress in the future, it is crucial to address the principal challenges and outline potential avenues for advancement in MXene@MOF composite research:

1. **Enhancing compositional diversity in MXene@MOF composites:** The amalgamation of MXene with various MOFs has yielded commendable outcomes, yet the array of accessible MOF species remains limited, with ZIFs and BDC-based MOFs constituting the prevailing choices. It is therefore imperative to explore a wider spectrum of MOFs that exhibit favorable compatibility with MXene. Simultaneously, while the repertoire of newly discovered MXenes continues to expand, the preponderance of research still centers around $Ti_3C_2T_x$. Numerous other MXene variants have displayed distinct promise and performance attributes, showcasing diverse compositions and surface functional groups that hold boundless potential for elevating the MXene@MOF composites performance.
2. **Optimization of synthetic approaches:** Conventional hydro/solvothermal preparation or thermal treatment of MXene@MOF composites can inadvertently hasten the oxidation of MXene, impacting its properties. To counter act this, it is recommended to employ milder synthetic methodologies. For instance, favoring synthesis at room temperature or employing straightforward conditions is advantageous. Additionally, the pursuit of greener, cost-effective, and scalable routes for synthesizing MXene@MOF composites and their derivatives is highly desirable.
3. **Establishing interfacial interactions:** The establishment of robust interfacial interactions between MXene and MOFs, or their derived materials, stands out as a potent avenue for enhancing structural integrity, stability, rate performance, and cyclic stability of energy storage devices. These interactions also influence the interfacial charge-transfer capacity by modulating the interfacial electric field. Therefore, the deliberate creation of strong coupling forces, such as chemical bonds, van der Waals interactions, and hydrogen bonds, between MXene and MOFs holds promise for achieving superior energy-related devices.
4. **Architectural design:** Crafting intricate architectures of MXenes/MOFs-based heterostructures with mixed dimensions (xD/2D, x = 0, 1, 2, and 3) is anticipated to amplify their electrocatalytic and energy storage attributes. Moreover, exploring diversified MXene-based support frameworks showcasing unique structures like hollow MXene spheres, MXene aerogels, layered MXene assemblies, and porous MXene NSs can significantly optimize electrochemical performance.
5. **Exploring MXene derived MOFs:** Beyond the in-situ conversion of V_2CT_x MXene into MOFs, the exploration of other MXene-derived MOFs remains underexplored. Although 2D V_2CT_x-derived MOFs have demonstrated compelling proton conductivity beneficial for advanced energy storage, current research in this domain is limited. Unlocking the potential of MXene-derived MOFs within the energy storage arena warrants further investigation.

6. **Fabrication of energy related devices:** Leveraging the innate hydrophilicity of MXene, the fabrication of micro or flexible electronic devices based on MXene@MOF composites can be pursued using advanced spinning, coating, and printing techniques. Furthermore, evaluating the practical viability of assembled energy storage devices under non-standard conditions holds promise for expanding their application scope.
7. **Understanding working mechanisms:** Employing advanced DFT calculations and coupled with characteristic techniques like in situ infrared, Raman spectroscopy, and synchrotron radiation can furnish deep insights into the intrinsic active sites and interfacial electronic structures evolution within MXene@MOF-based composites. Such understanding is pivotal to guiding subsequent explorations. Regrettably, numerous published works lack in-depth characteristic measurements and theoretical simulations. To attain a profound comprehension of these composites' energy storage and conversion mechanisms, enhancing theoretical calculations and in situ characterizations is paramount.

While MXene@MOF composites and their derived materials encounter significant challenges, their noteworthy strides in energy storage and conversion are undeniable. This review aspires to facilitate a deeper comprehension of functional MXene/MOF-based composites and offer valuable guidance for their future progression in the realm of electrochemical applications.

CRediT authorship contribution statement

Narasimharao Kitchamsetti: Conceptualization, Data curation, Formal analysis, Investigation, Methodology, Validation, Visualization, Writing – original draft, Writing – review & editing. **Jung Sang Cho:** Resources, Supervision, Writing – review & editing.

Declaration of competing interest

The authors declare that they have no known competing financial interests or personal relationships that could have appeared to influence the work reported in this paper.

Data availability

Data will be made available on request.

Acknowledgements

Narasimharao Kitchamsetti acknowledges Prof. Daewon Kim at Kyung Hee University, Republic of Korea for helping him in gaining in-depth knowledge and advancing his career in the field of energy storage and environmental applications. This work was supported by the National Research Foundation of Korea (NRF) grant funded by the Korea government (MSIT) [No. RS-2023-00217581]. This work was also supported by the Commercialization Promotion Agency for R&D Outcomes (COMPA) grant funded by the Korea government (Ministry of Science and ICT) [No. RS-2023-00304768]. This work was also supported by the Ministry of Education and National Research Foundation of Korea (NRF) for “Leaders in Industry-University Cooperation 3.0” project.

References

[1] M. Farghali, A.I. Osman, I.M.A. Mohamed, Z.H. Chen, L. Chen, I. Ihara, P.S. Yap, D.W. Rooney, Strategies to save energy in the context of energy crisis: a review, Environ. Chem. Lett. 21 (2023) 2003–2039, https://doi.org/10.1007/s10311-023-01591-5.
[2] P. Ekins, D. Zenghelis, The costs and benefits of environmental sustainability, Sustain. Sci. 16 (2021) 949–965, https://doi.org/10.1007/s11625-021-00910-5.
[3] N.Y.W. Zaw, S. Jo, J. Park, N. Kitchamsetti, N. Jayababu, D. Kim, Clay-assisted hierarchical growth of metal-telluride nanostructures as an anode material for hybrid supercapacitors, Appl. Clay Sci. 225 (2022) 106539, https://doi.org/10.1016/j.clay.2022.106539.
[4] G. Kothandam, G. Singh, X.W. Guan, J.M. Lee, K. Ramadass, S. Joseph, M. Bezigar, A. Karakoti, J.B. Yi, P. Kumar, A. Vinu, Recent advances in carbon-based electrodes for energy storage and conversion, Adv. Sci. 10 (2023) 2301045, https://doi.org/10.1002/advs.202301045.
[5] N. Kitchamsetti, A review on recent advances in Prussian blue, its analogues, and their derived materials as electrodes for high performance supercapacitors, J. Energy Storage 73 (2023) 108958, https://doi.org/10.1016/j.est.2023.108958.
[6] J. Park, S. Jo, N. Kitchamsetti, S. Zaman, D. Kim, The development of $NiCo_2O_4$/PVP/PANI heterogeneous nanocomposites as an advanced battery-type electrode material for high-performing supercapacitor application, J. Alloys Compd. 926 (2022) 166815, https://doi.org/10.1016/j.jallcom.2022.166815.
[7] I.Y. Kim, H.W. Cho, N. Kitchamsetti, J.H. Yun, J.M. Lee, W. Park, D.W. Kim, A robust triboelectric impact sensor with carbon dioxide precursor-based calcium carbonate layer for slap match application, Micromachines 14 (2023) 1778, https://doi.org/10.3390/mi14091778.
[8] J. Park, Y. Kim, N. Kitchamsetti, S. Jo, S. Lee, J. Song, W. Park, D. Kim, FeV LDH coated on sandpaper as an electrode material for high-performance flexible energy storage devices, Polymers 15 (2023) 1136, https://doi.org/10.3390/polym15051136.
[9] K. Narasimharao, G.V. Ramana, D. Sreedhar, V. Vasudevarao, Synthesis of graphene oxide by modified hummers method and hydrothermal synthesis of graphene-NiO nano composite for supercapacitor application, J. Material Sci. Eng. 5 (2016) 1000284, https://doi.org/10.4172/2169-0022.1000284.
[10] N. Kitchamsetti, D. Narsimulu, A. Chinthakuntla, C.S. Chakra, A.L.F. de Barros, Bimetallic MOF derived $ZnCo_2O_4$ nanocages as a novel class of high performance photocatalyst for the removal of organic pollutants, Inorg. Chem. Commun. 144 (2022) 109946, https://doi.org/10.1016/j.inoche.2022.109946.
[11] R. Chavan, N. Bhat, S. Parit, K. Narasimharao, R.S. Devan, R.B. Patil, V.C. Karade, N.V. Pawar, J.H. Kim, J.P. Jadhav, A.D. Chougale, Development of magnetically recyclable nanocatalyst for enhanced Fenton and photo-Fenton degradation of MB and Cr (VI) photo-reduction, Mater. Chem. Phys. 293 (2023) 126964, https://doi.org/10.1016/j.matchemphys.2022.126964.
[12] N. Kitchamsetti, C.S. Chakra, A.L.F. de Barros, D. Kim, Development of MOF based recyclable photocatalyst for the removal of different organic dye pollutants, Nanomaterials 13 (2023) 336, https://doi.org/10.3390/nano13020336.
[13] N. Kitchamsetti, M.S. Ramteke, S.R. Rondiya, S.R. Mulani, M.S. Patil, R.W. Cross, N.Y. Dzade, R.S. Devan, DFT and experimental investigations on the photocatalytic activities of NiO nanobelts for removal of organic pollutants, J. Alloys Compd. 855 (2021) 157337, https://doi.org/10.1016/j.jallcom.2020.157337.
[14] S. Jo, N. Kitchamsetti, H. Cho, D. Kim, Microwave-assisted hierarchically grown flake-like NiCo layered double hydroxide nanosheets on transitioned polystyrene towards triboelectricity-driven self-charging hybrid supercapacitors, Polymers 15 (2023) 454, https://doi.org/10.3390/polym15020454.
[15] Q. Xu, X. Liu, J. Zhang, Y. Xu, M. Zhou, J. Li, M. Du, K. Zhang, X. Qian, B. Xu, X. Wang, B. Wang, K. Zhang, Transition metal hydroxides@conducting MOFs on carbon nanotube yarns for ultra-stable quasi-solid-state supercapacitors with a ship-in-a-bottle architecture, J. Mater. Chem. A 11 (2023) 5309–5319, https://doi.org/10.1039/D2TA07804J.
[16] J.M. Mazurków, A. Kusior, A. Mikula, M. Radecka, Well-ordered surface metal atoms complexation by deposition of Pd cyclometa, Appl. Surf. Sci. 606 (2022) 154960, https://doi.org/10.1016/j.apsusc.2022.154960.
[17] J. Rehman, K. Eid, R. Ali, X. Fan, G. Murtaza, M. Faizan, A. Laref, W. Zheng, R. S. Varma, Engineering of transition metal sulfide nanostructures as efficient electrodes for high-performance supercapacitors, ACS Appl. Energy Mater. 5 (2022) 6481–6498, https://doi.org/10.1021/acsaem.1c03937.
[18] M. Wang, L. Zhang, Y. He, H. Zhu, Recent advances in transition-metal-sulfide-based bifunctional electrocatalysts for overall water splitting, J. Mater. Chem. A 9 (2021) 5320–5363, https://doi.org/10.1039/D0TA12152E.
[19] N. Kitchamsetti, M. Samtham, D. Singh, E. Choudhary, S.R. Rondiya, Y.R. Ma, R. W. Cross, N.Y. Dzade, R.S. Devan, Hierarchical 2D MnO_2@1D mesoporous $NiTiO_3$ core-shell hybrid structures for high-performance supercapattery electrodes: theoretical and experimental investigations, J. Electroanal. Chem. 936 (2023) 117359, https://doi.org/10.1016/j.jelechem.2023.117359.
[20] N. Kitchamsetti, D. Kim, High performance hybrid supercapacitor based on hierarchical MOF derived $CoFe_2O_4$ and $NiMn_2O_4$ composite for efficient energy storage, J. Alloys Compd. 959 (2023) 170483, https://doi.org/10.1016/j.jallcom.2023.170483.
[21] N. Kitchamsetti, A.L.F de Barros, Recent Advances in MXenes Based Composites as Photocatalysts: Synthesis, Properties and Photocatalytic Removal of Organic Contaminants from Wastewater, ChemCatChem 15 (2023) e202300690, doi: https://doi.org/10.1002/cctc.202300690.
[22] N. Kitchamsetti, R.J. Choudhary, D.M. Phase, R.S. Devan, Structural correlation of a nanoparticle-embedded mesoporous $CoTiO_3$ perovskite for an efficient electrochemical supercapacitor, RSC Adv. 10 (2020) 23446, https://doi.org/10.1039/D0RA04052E.
[23] M. Naguib, M. Kurtoglu, V. Presser, J. Lu, J. Niu, M. Heon, L. Hultman, Y. Gogotsi, M.W. Barsoum, Two-dimensional nanocrystals produced by exfoliation of Ti_3AlC_2, Adv. Mater. 23 (2011) 4248–4253, https://doi.org/10.1002/adma.201102306.
[24] N. Kitchamsetti, D. Kim, A facile method for synthesizing MOF derived $ZnCo_2O_4$ particles on MXene nanosheets as a novel anode material for high performance

hybrid supercapacitors, Electrochim. Acta 441 (2023) 141824, https://doi.org/10.1016/j.electacta.2023.141824.
[25] J. Yun, J. Park, M. Ryoo, N. Kitchamsetti, T.S. Goh, D. Kim, Piezo-triboelectric hybridized nanogenerator embedding MXene based bifunctional conductive filler in polymer matrix for boosting electrical power, Nano Energy 105 (2023) 108018, https://doi.org/10.1016/j.nanoen.2022.108018.
[26] M. Shekhirev, C.E. Shuck, A. Sarycheva, Y. Gogotsi, Characterization of MXenes at every step, from their precursors to single flakes and assembled films, Prog. Mater. Sci. 120 (2021) 100757, https://doi.org/10.1016/j.pmatsci.2020.100757.
[27] A.K. Tareen, K. Khan, M. Iqbal, S. Golovynskyi, Y. Zhang, A. Mahmood, N. Mahmood, J. Long, A. Al-Ghamdi, C. Li, H. Zhang, Recent advances in MXenes: new horizons in biomedical technologies, Mater. Today Chem. 26 (2022) 101205, https://doi.org/10.1016/j.mtchem.2022.101205.
[28] M.R. Tang, J. Li, Y. Wang, W. Han, S. Xu, M. Lu, W. Zhang, H. Li, Surface terminations of MXene: synthesis, characterization, and properties, Symmetry 14 (2022) 2232, https://doi.org/10.3390/sym14112232.
[29] Y. Gogotsi, Q. Huang, MXenes: two-dimensional building blocks for future materials and devices, ACS Nano 15 (2021) 5775–5780, https://doi.org/10.1021/acsnano.1c03161.
[30] X. Guan, Z. Yang, M. Zhou, L. Yang, R. Peymanfar, B. Aslibeiki, G. Ji, 2D MXene nanomaterials: synthesis, mechanism, and multifunctional applications in microwave absorption, Small Struct. 3 (2022) 2200102, https://doi.org/10.1002/sstr.202200102.
[31] W.K. Fan, A. Sherryna, M. Tahir, Advances in titanium carbide ($Ti_3C_2T_x$) MXenes and their metal-organic framework (MOF)-based nanotextures for solar energy applications: a review, ACS Omega 7 (2022) 38158–38192, https://doi.org/10.1021/acsomega.2c05030.
[32] N. Goel, A. Kushwaha, M. Kumar, Two-dimensional MXenes: recent emerging applications, RSC Adv. 12 (2022) 25172–25193, https://doi.org/10.1039/D2RA04354H.
[33] X. Bian, Z. Yang, T. Zhang, J. Yu, G. Xu, A. Chen, Q. He, J. Pan, Multifunctional flexible AgNW/MXene/PDMS composite films for efficient electromagnetic interference shielding and strain sensing, ACS Appl. Mater. Interfaces 15 (2023) 41906, https://doi.org/10.1021/acsami.3c08093.
[34] M.R. Lukatskaya, S. Kota, Z. Lin, M.Q. Zhao, N. Shpigel, M.D. Levi, J. Halim, P. L. Taberna, M.W. Barsoum, P. Simon, Y. Gogotsi, Ultra-high-rate pseudocapacitive energy storage in two-dimensional transition metal carbides, Nat. Energy 2 (2017) 17105, https://doi.org/10.1038/nenergy.2017.105.
[35] M. Naguib, J. Come, B. Dyatkin, V. Presser, P.L. Taberna, P. Simon, M. W. Barsoum, Y. Gogotsi, MXene: a promising transition metal carbide anode for lithium-ion batteries, Electrochem. Commun. 16 (2012) 61–64, https://doi.org/10.1016/j.elecom.2012.01.002.
[36] B. Huang, X. Tong, X. Zhang, Q. Feng, M.N. Rumyantseva, J. Prakash, X. Li, MXene/NiO composites for chemiresistive-type room temperature formaldehyde sensor, Chemosensors 11 (2023) 258, https://doi.org/10.3390/chemosensors11040258.
[37] M.T. Rahman, S.M.S. Rana, M. Salauddin, M.A. Zahed, S.H. Lee, E.S. Yoon, J. Y. Park, Silicone-incorporated nanoporous cobalt oxide and MXene nanocomposite-coated stretchable fabric for wearable triboelectric nanogenerator and self-powered sensing applications, Nano Energy 100 (2022) 107454, https://doi.org/10.1016/j.nanoen.2022.107454.
[38] J. Jin, T. Xiao, Y.F. Zhang, H. Zheng, H. Wang, R. Wang, Y.S. Gong, B. He, X. Liu, K. Zhou, Hierarchical MXene/transition metal chalcogenide heterostructures for electrochemical energy storage and conversion, Nanoscale 13 (2021) 19740–19770, https://doi.org/10.1039/D1NR05799E.
[39] K. Mistry, R. Jalja, B. Lakhani, S. Tripathi, P. Shinde, Chandra, recent trends in MXene/metal chalcogenides for electro−/photocatalytic hydrogen evolution reactions, Int. J. Hydrogen Energy 47 (2022) 41711–41732, https://doi.org/10.1016/j.ijhydene.2022.02.049.
[40] A.Z. Macknojia, A. Ayyagari, E. Shevchenko, D. Berman, MXene/graphene oxide nanocomposites for friction and wear reduction of rough steel surfaces, Sci. Rep. 13 (2023) 11057, https://doi.org/10.1038/s41598-023-37844-0.
[41] X.Y. Fu, C.J. Ma, R.Y. Shu, Y.Y. Zhang, H.B. Jiang, Electrostatic self-assembled MXene-graphene oxide composite electrodes for planar supercapacitors, Appl. Phys. Lett. 122 (2023) 113901, https://doi.org/10.1063/5.0130443.
[42] Y. Zhou, K. Maleski, B. Anasori, J.O. Thostenson, Y. Pang, Y. Feng, K. Zeng, C. B. Parker, S. Zauscher, Y. Gogotsi, J.T. Glass, C. Cao, $Ti_3C_2T_x$ MXene-reduced graphene oxide composite electrodes for stretchable supercapacitors, ACS Nano 14 (2020) 3576–3586, https://doi.org/10.1021/acsnano.9b10066.
[43] S. Wei, Y. Fu, M. Liu, H. Yue, S. Park, Y.H. Lee, H. Li, F. Yao, Dual-phase MoS_2/MXene/CNT ternary nanohybrids for efficient electrocatalytic hydrogen evolution, npj 2D Mater. Appl. 6 (2022) 25, https://doi.org/10.1038/s41699-022-00300-0.
[44] Y. Cui, K. Yang, F. Zhang, Y. Lyu, Q. Zhang, B. Zhang, Ultra-light MXene/CNTs/PI aerogel with neat arrangement for electromagnetic wave absorption and photothermal conversion, Compos. Part A Appl. Sci. Manuf. 158 (2022) 106986, https://doi.org/10.1016/j.compositesa.2022.106986.
[45] Z. Yan, Y. Ding, M. Huang, J. Li, Q. Han, M. Yang, W. Li, MXene/CNTs/aramid aerogels for electromagnetic interference shielding and joule heating, ACS Appl. Nano Mater. 6 (2023) 6141–6150, https://doi.org/10.1021/acsanm.3c00249.
[46] Y. Xia, Y. Ma, Y. Wu, Y. Yi, H. Lin, G. Zhu, Free-electrodeposited anodic stripping voltammetry sensing of cu(II) based on $Ti_3C_2T_x$ MXene/carbon black, Microchim. Acta 188 (2021) 377, https://doi.org/10.1007/s00604-021-05042-2.
[47] J. Zhang, Y. Zhao, X. Guo, C. Chen, C.L. Dong, R.S. Liu, C.P. Han, Y. Li, Y. Gogotsi, G. Wang, Single platinum atoms immobilized on an MXene as an efficient catalyst for the hydrogen evolution reaction, Nat. Catal. 1 (2018) 985–992, https://doi.org/10.1038/s41929-018-0195-1.
[48] T.A. Le, N.Q. Tran, Y. Hong, H.Y. Lee, Intertwined titanium carbide MXene within a 3 D tangled polypyrrole nanowires matrix for enhanced supercapacitor performances, Chem. A Eur. J. 25 (2019) 1037–1043, https://doi.org/10.1002/chem.201804291.
[49] X. Fu, L. Zhao, Z. Yuan, Y. Zheng, V. Shulga, W. Han, L. Wang, Hierarchical MXene@ZIF-67 film based high performance tactile sensor with large sensing range from motion monitoring to sound wave detection, Adv. Mater. Technol. 7 (2022) 2101511, https://doi.org/10.1002/admt.202101511.
[50] T.Y. Ma, J.L. Cao, M. Jaroniec, S.Z. Qiao, Interacting carbon nitride and titanium carbide nanosheets for high-performance oxygen evolution, Angew. Chem. Int. Ed. 55 (2016) 1138–1142, https://doi.org/10.1002/anie.201509758.
[51] Q.X. Deng, M.Q. Wang, X.L. Liu, H.S. Fan, Y.F. Zhang, H.Y. Yang, Ultrathin cobalt nickel selenides ($Co_{0.5}Ni_{0.5}Se_2$) nanosheet arrays anchoring on Ti_3C_2 MXene for high-performance Na^+/K^+ batteries, J. Colloid Interface Sci. 626 (2022) 700–709, https://doi.org/10.1016/j.jcis.2022.06.073.
[52] W.B. Zhao, Y.T. Zeng, Y.H. Zhao, X.L. Wu, Recent advances in metal-organic framework-based electrode materials for supercapacitors: a review, J. Energy Storage 62 (2023) 106934, https://doi.org/10.1016/j.est.2023.106934.
[53] S.Q. Yang, T.L. Hu, Reverse-selective metal-organic framework materials for the efficient separation and purification of light hydrocarbons, Coord. Chem. Rev. 468 (2022) 214628, https://doi.org/10.1016/j.ccr.2022.214628.
[54] S. Jiang, T.T. Lv, Y. Peng, H. Pang, MOFs containing solid-state electrolytes for batteries, Adv. Sci. 10 (2023) 2206887, https://doi.org/10.1002/advs.202206887.
[55] L.S. Andrade, H.H.L.B. Lima, C.T.P. Silva, W.L.N. Amorim, J.G.R. Poco, A. L. Castillo, M.V. Kirillova, W.A. Carvalho, A.M. Kirillov, D. Mandelli, Metal-organic frameworks as catalysts and biocatalysts for methane oxidation: the current state of the art, Coord. Chem. Rev. 481 (2023) 215042, https://doi.org/10.1016/j.ccr.2023.215042.
[56] H. Yuan, N. Li, W.D. Fan, H. Cai, D. Zhao, Metal-organic framework based gas sensors, Adv. Sci. 9 (2022) 2104374, https://doi.org/10.1002/advs.202104374.
[57] T. Mai, W.Y. Guo, P.L. Wang, L. Chen, M.Y. Qi, Q. Liu, Y. Ding, M.G. Ma, Bilayer metal-organic frameworks/MXene/nanocellulose paper with electromagnetic double loss for absorption-dominated electromagnetic interference shielding, Chem. Eng. J. 464 (2023) 142517, https://doi.org/10.1016/j.cej.2023.142517.
[58] H.M. Sun, X.N. Tang, S. Li, Y. Yao, L. Liu, MOF-derived one-dimensional Ru/Mo co-doped Co_3O_4 hollow microtubes for high-performance triethylamine sensing, Sens. Actuators B Chem. 383 (2023) 133583, https://doi.org/10.1016/j.snb.2023.133583.
[59] N. Muzaffar, A.M. Afzal, H.H. Hegazy, M.W. Iqbal, Recent advances in two-dimensional metal-organic frameworks as an exotic candidate for the evaluation of redox-active sites in energy storage devices, J. Energy Storage 64 (2023) 107142, https://doi.org/10.1016/j.est.2023.107142.
[60] H.N. Abdelhamid, S. Sultan, A.P. Mathew, Binder-free three-dimensional (3D) printing of cellulose-ZIF8 (CelloZIF-8) for water treatment and carbon dioxide (CO_2) adsorption, Chem. Eng. J. 468 (2023) 143567, https://doi.org/10.1016/j.cej.2023.143567.
[61] M.B. Poudel, P.C. Lohani, D. Acharya, D.R. Kandel, A.A. Kim, D.J. Yoo, MOF derived hierarchical ZnNiCo-LDH on vapor solid phase grown Cu_xO nanowire array as high energy density asymmetric supercapacitors, J. Energy Storage 72 (2023) 108220, https://doi.org/10.1016/j.est.2023.108220.
[62] Y. Cong, K. Chen, X.N. Chen, W. Xu, A. Cai, T.T. Li, Interface engineering of MOF-derived $NiMoO_4$@NiFeP core-shell nanorods for energy-saving hydrogen evolution via urea electrolysis, Inorg. Chem. 62 (2023) 4960–4970, https://doi.org/10.1021/acs.inorgchem.3c00074.
[63] D. Acharya, I. Pathak, B. Dahal, P.C. Lohani, R.M. Bhattarai, A. Muthurasu, T. W. Kim, T.H. Ko, K. Chhetri, H.Y. Kim, Immoderate nanoarchitectures of bimetallic MOF derived Ni-Fe-O/NPC on porous carbon nanofibers as freestanding electrode for asymmetric supercapacitors, Carbon 201 (2023) 12–23, https://doi.org/10.1016/j.carbon.2022.08.091.
[64] T. Maity, P. Malik, S. Bawari, S. Ghosh, J. Mondal, R. Halder, Chemically routed interpore molecular diffusion in metal-organic framework thin films, Nat. Commun. 14 (2023) 2212, https://doi.org/10.1038/s41467-023-37739-8.
[65] B.S. Du, F.F. Yan, X.H. Lin, C.Y. Liang, X.Z. Guo, Y. Tan, H. Zhen, C. Zhao, Y. Shi, E. Kibet, Y. He, X. Yang, A bottom-up sonication-assisted synthesis of Zn-BTC MOF nanosheets and the ppb-level acetone detection of their derived ZnO nanosheets, Sens. Actuators B Chem. 375 (2023) 132854, https://doi.org/10.1016/j.snb.2022.132854.
[66] A.K. Singh, K. Bijalwan, N. Kaushal, A. Kumari, A. Saha, A. Indra, Oxidase-like nanozyme activity of manganese metal-organic framework nanosheets for colorimetric and fluorescence sensing of L-cysteine, ACS Appl. Nano Mater. 6 (2023) 8036–8045, https://doi.org/10.1021/acsanm.3c01404.
[67] H.T. Guo, X.H. Lu, J. He, H.X. Zhang, H. Zhang, Y.H. Dong, D. Zhou, Q.H. Xia, Co-MOF nanosheet supported on ZSM-5 with an improved catalytic activity for air epoxidation of olefins, Mater. Chem. Phys. 294 (2023) 127001, https://doi.org/10.1016/j.matchemphys.2022.127001.
[68] W. Han, Y. Chen, Y. Jiao, S.M. Liang, W. Li, G.H. Tian, Oxygen vacancy-rich S-scheme CeO_2@$Ni_{1-x}Co_xSe_2$ hollow spheres derived from NiCo-MOF for remarkable photocatalytic CO_2 conversion, ACS Sustain. Chem. Eng. 11 (2023) 7787–7797, https://doi.org/10.1021/acssuschemeng.3c00470.
[69] X.Y. Chen, S.H. Xia, T.Y. Tan, Y. Zhu, L. Li, Q.C. Zhu, W.M. Zhang, In situ growth of MOF-derived nitrogen-doped carbon nanotubes on hollow MXene spheres for K-ion storage, Inorg. Chem. Front. 10 (2023) 4414–4424, https://doi.org/10.1039/D3QI00763D.

[70] T.Y. Lan, H.M. Du, Y.W. Li, K.G. Qu, J.S. Zhao, X.X. Zhang, Y.Y. Dong, Y. Zhang, X.Y. Zhang, D.Y. Zhang, One-pot synthesis of NiFe-MOF/$NiFe_2O_4$ hollow spheres and their application as bifunctional ORR/OER electrocatalysts in Zn-air batteries, J. Alloys Compd. 943 (2023) 169144, https://doi.org/10.1016/j.jallcom.2023.169144.
[71] M.R. Momeni, Z. Zhang, D.D. Angelo, F.A. Shakib, Tuning electronic properties of conductive 2D layered metal-organic frameworks via host-guest interactions: dioxygen as an electroactive chemical stimuli, APL Mater. 9 (2021) 051109, https://doi.org/10.1063/5.0049317.
[72] J.J. Liu, X.Y. Song, T. Zhang, S.Y. Liu, H. Wen, L. Chen, 2D conductive metal-organic frameworks: an emerging platform for electrochemical energy storage, Angew. Chem. Int. Ed. 133 (2021) 5672–5684, https://doi.org/10.1002/ange.202006102.
[73] C. Li, L. Zhang, J. Chen, X.L. Li, J.W. Sun, J.W. Zhu, X. Wang, Y.S. Fu, Recent development and applications of electrical conductive MOFs, Nanoscale 13 (2021) 485–509, https://doi.org/10.1039/D0NR06396G.
[74] J.G. Li, A. Kumar, B.A. Johnson, S. Ott, Experimental manifestation of redox-conductivity in metal-organic frameworks and its implication for semiconductor/insulator switching, Nat. Commun. 14 (2023) 4388, https://doi.org/10.1038/s41467-023-40110-6.
[75] X.M. Liu, L. Zhang, J. Wang, Design strategies for MOF-derived porous functional materials: preserving surfaces and nurturing pores, J. Mater. 7 (2021) 440–459, https://doi.org/10.1016/j.jmat.2020.10.008.
[76] X.L. Liu, G. Verma, Z.S. Chen, B.W. Hu, Q. Huang, H. Yang, S.Q. Ma, X.K. Wang, Metal-organic framework nanocrystal-derived hollow porous materials: synthetic strategies and emerging applications, Innovation 3 (2022) 100281, https://doi.org/10.1016/j.xinn.2022.100281.
[77] J.D. Sosa, T.F. Bennett, K.J. Nelms, B.M. Liu, R.C. Tovar, Y.Y. Liu, Metal-organic framework hybrid materials and their applications, Crystals 8 (2018) 325, https://doi.org/10.3390/cryst8080325.
[78] L. Zhao, B.L. Dong, S.Z. Li, L.J. Zhou, L.F. Lai, Z.W. Wang, S.L. Zhao, M. Han, K. Gao, M. Lu, X. Xie, B. Chen, Z.D. Liu, X.J. Wang, H. Zhang, H. Li, J.Q. Liu, H. Zhang, X. Huang, W. Huang, Interdiffusion reaction-assisted hybridization of two-dimensional metal-organic frameworks and $Ti_3C_2T_x$ nanosheets for electrocatalytic oxygen evolution, ACS Nano 11 (2017) 5800–5807, https://doi.org/10.1021/acsnano.7b01409.
[79] H.M. Wang, R. Zhao, J.Q. Qin, H.X. Hu, X.W. Fan, X. Cao, D. Wang, MIL-100(Fe)/Ti_3C_2 MXene as a Schottky catalyst with enhanced photocatalytic oxidation for nitrogen fixation activities, ACS Appl. Mater. Interfaces 11 (2019) 44249–44262, https://doi.org/10.1021/acsami.9b14793.
[80] S.J. Yang, T.H. Kim, J.H. Im, Y.S. Kim, K. Lee, H. Jung, C.R. Park, MOF-derived hierarchically porous carbon with exceptional porosity and hydrogen storage capacity, Chem. Mater. 24 (2012) 464–470, https://doi.org/10.1021/cm202554j.
[81] W.Y. Chen, B. Han, Y. Xie, S. Liang, H. Deng, Z. Lin, Ultrathin Co-Co LDHs nanosheets assembled vertically on MXene: 3D nanoarrays for boosted visible-light-driven CO_2 reduction, Chem. Eng. J. 391 (2020) 123519, https://doi.org/10.1016/j.cej.2019.123519.
[82] X. Zhao, H. Xu, Z.Y. Hui, Y. Sun, C.Y. Yu, J. Xue, R.C. Zhou, L. Wang, H. Dai, Y. Zhao, J. Yang, J.Y. Zhou, Q. Chen, G.Z. Sun, W. Huang, Electrostatically assembling 2D nanosheets of MXene and MOF-derivatives into 3D hollow frameworks for enhanced lithium storage, Small 15 (2019) 1904255, https://doi.org/10.1002/smll.201904255.
[83] M. Wang, P.P. Zhou, T. Feng, Z. Song, Q.G. Ren, H.D. Gu, X.Q. Shi, Q. Zhang, L. Wang, Ni-MOF/$Ti_3C_2T_x$ derived multidimensional hierarchical Ni/TiO_2/C nanocomposites with lightweight and efficient microwave absorption, Ceram. Int. 48 (2022) 22681–22690, https://doi.org/10.1016/j.ceramint.2022.03.154.
[84] T.E. Chen, T. Shen, Y.H. Wang, Z. Yu, W. Zhang, Y. Zhang, Z. Ouyang, Q.G. Cai, Y. X. Ji, S.F. Wang, In Situ Synthesis of Ni-BTC Metal–Organic Framework@ Graphene Oxide Composites for High-Performance Supercapacitor Electrodes, ACS Omega 8 (2023) 10888–10898, doi:https://doi.org/10.1021/acsomega.2c07187.
[85] X.Y. Liang, X.F. Ren, Q. Yang, L. Gao, M.F. Gao, Y. Yang, H. Zhu, G.X. Li, T. Ma, A. Liu, A two-dimensional MXene-supported metal-organic framework for highly selective ambient electrocatalytic nitrogen reduction, Nanoscale 13 (2021) 2843–2848, https://doi.org/10.1039/D0NR08744K.
[86] H.B. Parse, I. Patil, B. Kakade, A. Swami, Cobalt nanoparticles encapsulated in N-doped carbon on the surface of MXene (Ti_3C_2) play a key role for electroreduction of oxygen, Energy Fuel 35 (2021) 17909–17918, https://doi.org/10.1021/acs.energyfuels.1c02486.
[87] L.H. He, J.M. Liu, B. Hu, Y.K. Liu, B.B. Cui, D.L. Peng, Z.H. Zhang, S. Wu, B.Z. Liu, Cobalt oxide doped with titanium dioxide and embedded with carbon nanotubes and graphene-like nanosheets for efficient trifunctional electrocatalyst of hydrogen evolution, oxygen reduction, and oxygen evolution reaction, J. Power Sources 414 (2019) 333–344, https://doi.org/10.1016/j.jpowsour.2019.01.020.
[88] Y. Wu, X.M. Li, Q. Yang, D.B. Wang, F.B. Yao, J. Cao, Z. Chen, X.D. Huang, Y. Yang, X.P. Li, Mxene-modulated dual-heterojunction generation on a metal-organic framework (MOF) via surface constitution reconstruction for enhanced photocatalytic activity, Chem. Eng. J. 390 (2020) 124519, https://doi.org/10.1016/j.cej.2020.124519.
[89] L. Yao, Q.F. Gu, X.B. Yu, Three-dimensional MOFs@MXene aerogel composite derived MXene threaded hollow carbon confined CoS nanoparticles toward advanced alkali-ion batteries, ACS Nano 15 (2021) 3228–3240, https://doi.org/10.1021/acsnano.0c09898.
[90] W.X. Zhang, S. Tang, Z.H. Chen, X.C. Xiong, B. Chen, K. Wu, G.H. Xu, S. Cheng, Y. C. Cao, The controllable construction of nanochannel in two-dimensional lamellar film for efficient oxygen reduction reaction and lithium-oxygen batteries, Chem. Eng. J. 430 (2022) 132489, https://doi.org/10.1016/j.cej.2021.132489.
[91] J.H. Zhao, L.W. Liu, K. Li, T. Li, F.T. Liu, Conductive Ti_3C_2 and MOF-derived CoS_x boosting the photocatalytic hydrogen production activity of TiO_2, CrystEngComm 21 (2019) 2416, https://doi.org/10.1039/C8CE02050G.
[92] D.D. Song, X. Jiang, Y.S. Li, X. Lu, S.R. Luan, Y.Z. Wang, Y. Li, F.M. Gao, Metal-organic frameworks-derived MnO_2/Mn_3O_4 microcuboids with hierarchically ordered nanosheets and Ti_3C_2 MXene/Au NPs composites for electrochemical pesticide detection, J. Hazard. Mater. 373 (2019) 367–376, https://doi.org/10.1016/j.jhazmat.2019.03.083.
[93] S.H. Nam, M. Mahato, K. Matthews, R.W. Lord, Y.H. Lee, P. Thangasamy, C. W. Ahn, Y. Gogotsi, I.K. Oh, Bimetal organic framework-$Ti_3C_2T_x$ MXene with metalloporphyrin electrocatalyst for lithium-oxygen batteries, Adv. Funct. Mater. 33 (2023) 2210702, https://doi.org/10.1002/adfm.202210702.
[94] H.B. Li, J.L. Li, L. Ma, X. Zhang, J.F. Li, J.B. Li, T. Lu, L. Pan, Heteroatomic interface engineering of an octahedron VSe_2-ZrO_2/C/MXene composite derived from a MXene-MOF hybrid as a superior-performance anode for lithium-ion batteries, J. Mater. Chem. A 11 (2023) 2836–2847, https://doi.org/10.1039/D2TA09043K.
[95] Y.H. Liu, L.X. Li, A.Y. Wen, F.F. Cao, H. Ye, A Janus MXene/MOF separator for the all-in-one enhancement of lithium-sulfur batteries, Energy Storage Mater. 55 (2023) 652–659, https://doi.org/10.1016/j.ensm.2022.12.028.
[96] Z. Pouramini, S.M. Mousavi, A. Babapoor, S.A. Hashemi, C.W. Lai, Y. Mazaheri, W.H. Chiang, Effect of metal atom in zeolitic imidazolate frameworks (ZIF-8 & 67) for removal of dyes and antibiotics from wastewater: a review, Catalysts 13 (2023) 155, https://doi.org/10.3390/catal13010155.
[97] W.C. Hong, B.C. Wyatt, S.K. Nemani, B. Anasori, Double transition-metal MXenes: atomistic design of two-dimensional carbides and nitrides, MRS Bull. 45 (2020) 850–861, https://doi.org/10.1557/mrs.2020.251.
[98] F. Wu, Z.H. Liu, J. Wang, T. Shah, P. Liu, Q.Y. Zhang, B.L. Zhang, Template-free self-assembly of MXene and CoNi-bimetal MOF into intertwined one-dimensional heterostructure and its microwave absorbing properties, Chem. Eng. J. 422 (2021) 130591, https://doi.org/10.1016/j.cej.2021.130591.
[99] R.H. Li, X.F. Fu, G.Z. Liu, J.H. Li, G.Y. Zhou, G.P. Liu, W.Q. Jin, Room-temperature in situ synthesis of MOF@MXene membrane for efficient hydrogen purification, J. Membr. Sci. 664 (2022) 121097, https://doi.org/10.1016/j.memsci.2022.121097.
[100] M. Liu, J.X. Wang, P. Song, J. Li, Q. Wang, Metal-organic frameworks-derived In_2O_3 microtubes/$Ti_3C_2T_x$ MXene composites for NH_3 detection at room temperature, Sens. Actuators B Chem. 361 (2022) 131755, https://doi.org/10.1016/j.snb.2022.131755.
[101] H.Y. Wang, X.B. Sun, G.S. Wang, A MXene-modulated 3D crosslinking network of hierarchical flower-like MOF derivatives towards ultra-efficient microwave absorption properties, J. Mater. Chem. A 9 (2021) 24571–24581, https://doi.org/10.1039/D1TA06505J.
[102] P.P. Tan, R.W. Gao, Y.W. Zhang, N. Han, Y.Z. Jiang, M.W. Xu, S.J. Bao, X. Zhang, Electrostatically directed assembly of two-dimensional ultrathin Co_2Ni-MOF/$Ti_3C_2T_x$ nanosheets for electrocatalytic oxygen evolution, J. Colloid Interface Sci. 630 (2023) 363–371, https://doi.org/10.1016/j.jcis.2022.10.109.
[103] Y. Yang, X.Y. Huang, C. Sheng, Y.Y. Pan, Y. Huang, X.H. Wang, In-situ formation of MOFs derivatives $CoSe_2$/Ni_3Se_4 nanosheets on MXene nanosheets for hybrid supercapacitor with enhanced electrochemical performance, J. Alloys Compd. 920 (2022) 165908, https://doi.org/10.1016/j.jallcom.2022.165908.
[104] Y. Gogotsi, Transition metal carbides go 2D, Nat. Mater. 14 (2015) 1079–1080, https://doi.org/10.1038/nmat4386.
[105] B.G. Zhou, H.H. Yin, C.H. Dong, L.P. Sun, W. Feng, Y.Y. Pu, X.X. Han, X.L. Li, D. Du, H.X. Xu, Y. Chen, Biodegradable and Excretable 2D $W_{1.33}C$ *i*-MXene with Vacancy Ordering for Theory-Oriented Cancer Nanotheranostics in Near-Infrared Biowindow, Adv. Sci. 8 (2021) 2101043, doi:https://doi.org/10.1002/advs.202101043.
[106] Y. Wei, P. Zhang, R.A. Soomro, Q.Z. Zhu, B. Xu, Advances in the synthesis of 2D MXenes, Adv. Mater. 33 (2021) 2103148, https://doi.org/10.1002/adma.202103148.
[107] H. Xu, A. Ren, J. Wu, Z.M. Wang, Recent advances in 2D MXenes for photodetection, Adv. Funct. Mater. 30 (2020) 2000907, https://doi.org/10.1002/adfm.202000907.
[108] M. Ghidiu, M.R. Lukatskaya, M.Q. Zhao, Y. Gogotsi, M.W. Barsoum, Conductive two-dimensional titanium carbide 'clay' with high volumetric capacitance, Nature 516 (2014) 78–81, https://doi.org/10.1038/nature13970.
[109] Y. Yao, Z.F. Wang, Y.T. Han, L. Xie, X.L. Zhao, S. Shahrokhian, N. Barsan, Z. G. Zhu, Conductometric Cr_2O_3/TiO_2/$Ti_3C_2T_x$ gas sensor for detecting triethylamine at room temperature, Sens. Actuators B Chem. 381 (2023) 133412, https://doi.org/10.1016/j.snb.2023.133412.
[110] C.J. Shen, L. Wang, A. Zhou, B. Wang, X.L. Wang, W.W. Lian, Q.K. Hu, G. Qin, X. Q. Liu, Synthesis and electrochemical properties of two-dimensional RGO/$Ti_3C_2T_x$ nanocomposites, Nanomaterials 8 (2018) 80, https://doi.org/10.3390/nano8020080.
[111] L.H. Karlsson, J. Birch, J. Halim, M.W. Barsoum, P.O.A. Persson, Atomically resolved structural and chemical investigation of single MXene sheets, Nano Lett. 15 (2015) 4955–4960, https://doi.org/10.1021/acs.nanolett.5b00737.
[112] M.W. Zhang, R.L. Liang, N. Yang, R. Gao, Y. Zheng, Y.P. Deng, Y.F. Hu, A.P. Yu, Z. W. Chen, Eutectic etching toward in-plane porosity manipulation of cl-terminated MXene for high-performance dual-ion battery anode, Adv. Energy Mater. 12 (2022) 2102493, https://doi.org/10.1002/aenm.202102493.
[113] Y. Bai, C.L. Lui, T.T. Chen, W.T. Li, S. Zheng, Y.C. Pi, Y.S. Luo, H. Pang, MXene-copper/cobalt hybrids via Lewis acidic molten salts etching for high performance

symmetric supercapacitors, Angew. Chem. Int. Ed. 60 (2021) 25318–25322, https://doi.org/10.1002/anie.202112381.
[114] W. Sun, S.A. Shah, Y. Chen, Z. Tan, H. Gao, T. Habib, M. Radovic, M.J. Green, Electrochemical etching of Ti_2AlC to Ti_2CT_x (MXene) in low-concentration hydrochloric acid solution, J. Mater. Chem. A 5 (2017) 21663–21668, https://doi.org/10.1039/C7TA05574A.
[115] L. Wang, X. Zhang, C. Li, Y. Xu, Y. An, W.J. Liu, T. Hu, S. Yi, K. Wang, X.Z. Sun, Y. Gong, Z.S. Wu, Y.W. Ma, Cation-deficient T-Nb_2O_5/graphene hybrids synthesized via chemical oxidative etching of MXene for advanced lithium-ion capacitors, Chem. Eng. J. 468 (2023) 143507, https://doi.org/10.1016/j.cej.2023.143507.
[116] G.Z. Guan, F.M. Guo, A review of Nb_2CT_x MXene: synthesis, properties and applications, Batteries 9 (2023) 235, https://doi.org/10.3390/batteries9040235.
[117] F. Seidi, A.A. Shamsabadi, M.D. Firouzjaei, M. Elliot, M.R. Saeb, Y. Huang, C.C. Li, H.N. Xiao, B. Anasori, MXenes antibacterial properties and applications: a review and perspective, Small 19 (2023) 2206716, https://doi.org/10.1002/smll.202206716.
[118] Z.D. Guo, G.S. Dong, M. Zhang, M. Gao, L.J. Shao, M. Chen, H.L. Liu, M.C. Ni, D. X. Cao, K. Zhu, Sulfur-decorated $Ti_3C_2T_x$ MXene for high-performance sodium/potassium-ion batteries, Chem. Asian J. 18 (2023) e202300336, https://doi.org/10.1002/asia.202300336.
[119] F.W. Ming, H.F. Liang, G. Huang, Z. Bayhan, H.N. Alshareef, MXenes for rechargeable batteries beyond the lithium-ion, Adv. Mater. 33 (2021) 2004039, https://doi.org/10.1002/adma.202004039.
[120] B.L. Yang, B.J. Li, Z.H. Xiang, Advanced MOF-based electrode materials for supercapacitors and electrocatalytic oxygen reduction, Nano Res. 16 (2023) 1338–1361, https://doi.org/10.1007/s12274-022-4682-y.
[121] A. Bhat, S. Anwer, K.S. Bhat, M.I.H. Mohideen, K. Liao, A. Qurashi, Prospects challenges and stability of 2D MXenes for clean energy conversion and storage applications, npj 2d Mater. Appl. 5 (2021) 61, https://doi.org/10.1038/s41699-021-00239-8.
[122] C.C. Ji, H.N. Cui, H.Y. Mi, S.C. Yang, Applications of 2D MXenes for electrochemical energy conversion and storage, Energies 14 (2021) 8183, https://doi.org/10.3390/en14238183.
[123] S.K. Azadi, M. Zeynali, S. Asgharizadeh, M.A. Fooladloo, Investigation of the optical and electronic properties of functionalized Ti_3C_2 Mxene with halid atoms using DFT calculation, Mater. Today Commun. 35 (2023) 106136, https://doi.org/10.1016/j.mtcomm.2023.106136.
[124] A.A. Banu, S. Sinthika, S. Premkumar, J. Vigneshwaran, S.Z. Karazhanov, S. P. Jose, DFT study of NH_3 adsorption on 2D monolayer MXenes (M_2C, M = Cr, Fe) via oxygen functionalization: suitable materials for gas sensors, FlatChem 31 (2022) 100329, https://doi.org/10.1016/j.flatc.2021.100329.
[125] O.M. Yaghi, G.M. Li, H.L. Li, Selective binding and removal of guests in a microporous metal-organic framework, Nature 378 (1995) 703–706, https://doi.org/10.1038/378703a0.
[126] X.F. Lu, Y.J. Fang, D. Luan, X.W.D. Lou, Metal-organic frameworks derived functional materials for electrochemical energy storage and conversion: a mini review, Nano Lett. 21 (2021) 1555–1565, https://doi.org/10.1021/acs.nanolett.0c04898.
[127] X. Zhang, F. Peng, D.H. Wang, MOFs and MOF-derived materials for antibacterial application, J. Funct. Biomater. 13 (2022) 215, https://doi.org/10.3390/jfb13040215.
[128] G.J. Zhou, Y. Wang, Z.H. Huang, Structure and function tailored metal-organic frameworks for heterogeneous catalysis, Chem Catal. 2 (2022) 3304–3319, https://doi.org/10.1016/j.checat.2022.10.023.
[129] S.E. Skrabalak, R. Vaidhyanathan, The chemistry of metal organic framework materials, Chem. Mater. 35 (2023) 5713–5722, https://doi.org/10.1021/acs.chemmater.3c01729.
[130] X.Y. Yin, A. Alsuwaidi, X.Y. Zhang, Hierarchical metal-organic framework (MOF) pore engineering, Microporous Mesoporous Mater. 330 (2022) 111633, https://doi.org/10.1016/j.micromeso.2021.111633.
[131] J.Q. Chen, L. Esrafili, F. Parsa, A.N. Sun, M.L. Hu, A. Morsali, P. Retailleau, Z. F. Guo, P.C. Junk, Multi-functionalized MOFs with large-pore apertures as luminescent probes for efficient sensing of quinones, New J. Chem. 47 (2023) 4920–4930, https://doi.org/10.1039/D2NJ05689E.
[132] S.A. Yuan, L.F. Zou, J.S. Qin, J.L. Li, L. Huang, L. Feng, X. Wang, M. Bosch, A. Alsalme, T. Cagin, H.C. Zhou, Construction of hierarchically porous metal-organic frameworks through linker labilization, Nat. Commun. 8 (2017) 15356, https://doi.org/10.1038/ncomms15356.
[133] H. Li, M. Eddaoudi, M.O. Keeffe, O.M. Yaghi, Design and synthesis of an exceptionally stable and highly porous metal-organic framework, Nature 402 (1999) 276–279, https://doi.org/10.1038/46248.
[134] K.C. Wang, X.L. Lv, D.W. Feng, J. Li, S.M. Chen, J.L. Sun, L. Song, Y. Xie, J.R. Li, H.C. Zhou, Pyrazolate-based porphyrinic metal-organic framework with extraordinary base-resistance, J. Am. Chem. Soc. 138 (2016) 914–919, https://doi.org/10.1021/jacs.5b10881.
[135] O.A. Kholdeeva, I.Y. Skobelev, I.D. Ivanchikova, K.A. Kovalenko, V.P. Fedin, A. B. Sorokin, Hydrocarbon oxidation over Fe- and Cr-containing metal-organic frameworks MIL-100 and MIL-101-a comparative study, Catal. Today 238 (2014) 54–61, https://doi.org/10.1016/j.cattod.2014.01.010.
[136] B.F.R. Mendoza, O.A.E. Filho, K.J.F. Andrade, F. Curbelo, F.F. da Silva, R. Luque, J.M.R. Diaz, MOF@biomass hybrids: trends on advanced functional materials for adsorption, Environ. Res. 216 (2023) 114424, https://doi.org/10.1016/j.envres.2022.114424.
[137] S.J. Guan, J.X. Li, Y.Y. Wang, Y. Yang, X. Zhu, D.D. Ye, R. Chen, Q. Liao, Multifunctional MOF-derived au, co-doped porous carbon electrode for a wearable sweat energy harvesting-storage hybrid system, Adv. Mater. 35 (2023) 2304465, https://doi.org/10.1002/adma.202304465.
[138] G.J. Song, Y.X. Shi, S. Jiang, H. Pang, Recent progress in MOF-derived porous materials as electrodes for high-performance lithium-ion batteries, Adv. Funct. Mater. (2023) 2303121, https://doi.org/10.1002/adfm.202303121.
[139] H. Wang, S. Li, H. Zhu, S.Y. Yu, T.Y. Yang, H.W. Zhao, A MOF-derived porous In_2O_3 flower-like hierarchical architecture sensor: near room-temperature preparation and fast trimethylamine sensing performance, New J. Chem. 47 (2023) 10265–10272, https://doi.org/10.1039/D3NJ01350B.
[140] X.Z. Wang, D. Kukkar, S.A. Younis, K. Vikrant, Y. Ahmadi, D. Boukhvalov, K. H. Kim, The co-adsorption potential of metal–organic framework/activated carbon composites against both polar and non-polar volatile organic compounds in air, Sep. Purif. Technol. 306 (2023) 122594, https://doi.org/10.1016/j.seppur.2022.122594.
[141] Y. Liu, Z. Wei, S. Wu, S. Qiao, H.B. Zhao, Enhanced bioelectrochemical performance by NiCoAl-LDH/MXene hybrid as cathode catalyst for microbial fuel cell, Int. J. Hydrogen Energy 48 (2023) 6056–6066, https://doi.org/10.1016/j.ijhydene.2022.11.173.
[142] T.X. Liang, X.J. Yang, B. Liu, R.D. Song, F. Xiao, Y.J. Yang, D. Wang, M.Y. Dong, J. Ren, B.B. Xu, H. Algadi, Y.Y. Yang, Ammonium perchlorate@graphene oxide/cu-MOF composites for efficiently catalyzing the thermal decomposition of ammonium perchlorate, Adv. Compos. Hybrid Mater. 6 (2023) 67, https://doi.org/10.1007/s42114-023-00651-2.
[143] V. Siva, A. Murugan, A. Shameem, M.A. Jothi, S. Kannan, Nanoscale Zn-MOF enwrapped polymer nanocomposite as electrode material for enhanced energy storage system, Inorg. Chem. Commun. 154 (2023) 110986, https://doi.org/10.1016/j.inoche.2023.110986.
[144] H. Cheng, G.Y. Xu, C.Y. Zhu, Z. Alhalili, X. Du, G. Gao, Porous MOF derived TiO_2/ZnO/C@CNTs composites for enhancing lithium storage performance, Chem. Eng. J. 454 (2023) 140454, https://doi.org/10.1016/j.cej.2022.140454.
[145] X.F. Li, Q.L. Zhu, MOF-based materials for photo- and electrocatalytic CO_2 reduction, Energychem 2 (2020) 100033, https://doi.org/10.1016/j.enchem.2020.100033.
[146] Y.Y. Yang, Y.Q. Xu, Q.H. Li, Y.G. Zhang, H. Zhou, Two-dimensional carbide/nitride (MXene) materials in thermal catalysis, J. Mater. Chem. A 10 (2022) 19444–19465, https://doi.org/10.1039/D2TA03481F.
[147] X. Chen, H. Yu, Y. Gao, L. Wang, G. Wang, The marriage of two-dimensional materials and phase change materials for energy storage, conversion and applications, Energychem 4 (2022) 100071, https://doi.org/10.1016/j.enchem.2022.100071.
[148] S.H. Huang, V.N. Mochalin, Combination of high pH and an antioxidant improves chemical stability of two-dimensional transition-metal carbides and Carbonitrides (MXenes) in aqueous colloidal solutions, Inorg. Chem. 61 (2022) 9877–9887, https://doi.org/10.1021/acs.inorgchem.2c00537.
[149] A. Iqbal, J.P. Hong, T.Y. Ko, C.M. Koo, Improving oxidation stability of 2D MXenes: synthesis, storage media, and conditions, Nano Convergence 8 (2021) 9, https://doi.org/10.1186/s40580-021-00259-6.
[150] L. Yang, D.X. Kan, C.X.D. Agnese, Y.D. Agnese, B. Wang, A.K. Jena, Y.J. Wei, G. Chen, X.F. Wang, Y. Gogotsi, T. Miyasaka, Performance improvement of MXene-based perovskite solar cells upon property transition from metallic to semiconductive by oxidation of $Ti_3C_2T_x$ in air, J. Mater. Chem. A 9 (2021) 5016–5025, https://doi.org/10.1039/D0TA11397B.
[151] X.F. Zhao, A. Vashisth, E. Prehn, W.M. Sun, S.A. Shah, T. Habib, Y.X. Chen, Z. Tan, J.L. Lutkenhaus, M. Radovic, M.J. Green, Antioxidants unlock shelf-stable $Ti_3C_2T_x$ (MXene) nanosheet dispersions, Matter 1 (2019) 513, https://doi.org/10.1016/j.matt.2019.05.020.
[152] X.F. Zhao, H.X. Cao, B.J. Coleman, Z. Tan, I.J. Echols, E.B. Pentzer, J. L. Lutkenhaus, M. Radovic, M.J. Green, The role of antioxidant structure in mitigating oxidation in $Ti_3C_2T_x$ and Ti_2CT_x MXenes, Adv. Mater. Interfaces 9 (2022) 2200480, https://doi.org/10.1002/admi.202200480.
[153] R.A. Soomro, P. Zhang, B.M. Fan, Y. Wei, B. Xu, Progression in the oxidation stability of MXenes, Nano-Micro Lett. 15 (2023) 108, https://doi.org/10.1007/s40820-023-01069-7.
[154] S.S. Zheng, H.J. Zhou, H.G. Xue, P. Braunstein, H. Pang, Pillared-layer Ni-MOF nanosheets anchored on Ti_3C_2 MXene for enhanced electrochemical energy storage, J. Colloid Interface Sci. 614 (2022) 130–137, https://doi.org/10.1016/j.jcis.2022.01.094.
[155] P. Xiao, G.D. Zhu, X.H. Shang, B. Hu, B.S. Zhang, Z.Y. Tang, J.M. Yang, J.Y. Liu, An Fe-MOF/MXene-based ultra-sensitive electrochemical sensor for arsenic (III) measurement, J. Electroanal. Chem. 916 (2022) 116382, https://doi.org/10.1016/j.jelechem.2022.116382.
[156] Y.J. Li, Y.Y. Liu, Z.Y. Wang, P. Wang, Z.K. Zheng, H.F. Cheng, Y. Dai, B.B. Huang, In-situ growth of Ti_3C_2@MIL-NH_2 composite for highly enhanced photocatalytic H_2 evolution, Chem. Eng. J. 411 (2021) 128446, https://doi.org/10.1016/j.cej.2021.128446.
[157] R. Ramachandran, K. Rajavel, W.L. Xuan, D.H. Lin, F. Wang, Influence of $Ti_3C_2T_x$ (MXene) intercalation pseudocapacitance on electrochemical performance of Co-MOF binder-free electrode, Ceram. Int. 44 (2018) 14425–14431, https://doi.org/10.1016/j.ceramint.2018.05.055.
[158] C.Y. Wen, D.H. Guo, X.Z. Zheng, H.F. Li, G.B. Sun, Hierarchical nMOF-867/MXene nanocomposite for chemical adsorption of polysulfides in lithium-sulfur batteries, ACS Appl. Energy Mater. 4 (2021) 8231–8241, https://doi.org/10.1021/acsaem.1c01481.
[159] X.L. Hong, Z. Lu, Y. Zhao, L. Lyu, L. Ding, Y.Y. Wei, H.H. Wang, Fast fabrication of freestanding MXene-ZIF-8 dual-layered membranes for H_2/CO_2 separation,

J. Membr. Sci. 642 (2022) 119982, https://doi.org/10.1016/j.memsci.2021.119982.
[160] Y.J. Liu, Y. He, E. Vargun, T. Plachy, P. Saha, Q. Cheng, 3D porous Ti_3C_2 MXene/NiCo-MOF composites for enhanced lithium storage, Nanomaterials 10 (2020) 695, https://doi.org/10.3390/nano10040695.
[161] T.Q. Hou, Z.R. Jia, B.B. Wang, H.B. Li, X.H. Liu, Q.G. Chi, G.L. Wu, Metal-organic framework-derived $NiSe_2$-$CoSe_2$@C/$Ti_3C_2T_x$ composites as electromagnetic wave absorbers, Chem. Eng. J. 422 (2021) 130079, https://doi.org/10.1016/j.cej.2021.130079.
[162] B. Cao, H. Liu, X. Zhang, P. Zhang, Q.Z. Zhu, H.L. Du, L.L. Wang, R. Zhang, B. Xu, MOF-derived ZnS nanodots/$Ti_3C_2T_x$ MXene hybrids boosting superior lithium storage performance, Nano-Micro Lett. 13 (2021) 202, https://doi.org/10.1007/s40820-021-00728-x.
[163] J.H. Wang, J.X. Gong, H. Zhang, L.L. Lv, Y.X. Liu, Y.T. Dai, Construction of hexagonal nickel-cobalt oxide nanosheets on metal-organic frameworks based on MXene interlayer ion effect for hybrid supercapacitors, J. Alloys Compd. 870 (2021) 159466, https://doi.org/10.1016/j.jallcom.2021.159466.
[164] X.Q. Fan, Y. Yang, X.L. Shi, Y. Liu, H.P. Li, J.J. Liang, Y.S. Chen, A MXene-based hierarchical design enabling highly efficient and stable solar-water desalination with good salt resistance, Adv. Funct. Mater. 30 (2020) 2007110, https://doi.org/10.1002/adfm.202007110.
[165] R.M. Huang, D. Liao, S. Chen, J.G. Yu, X.Y. Jiang, A strategy for effective electrochemical detection of hydroquinone and catechol: decoration of alkalization-intercalated Ti_3C_2 with MOF-derived N-doped porous carbon, Sens. Actuators B Chem. 320 (2020) 128386, https://doi.org/10.1016/j.snb.2020.128386.
[166] H.G. Oh, S.K. Park, Two-dimensional composite of nitrogen-doped graphitic carbon-coated cobaltosic oxide nanocrystals on MXene nanosheets as high-performance anode for lithium-ion batteries, Appl. Surf. Sci. 564 (2021) 150415, https://doi.org/10.1016/j.apsusc.2021.150415.
[167] P. Tian, X. He, L. Zhao, W.X. Li, W. Fang, H. Chen, F.Q. Zhang, Z.H. Huang, H. L. Wang, Enhanced charge transfer for efficient photocatalytic H_2 evolution over UiO-66-NH_2 with annealed $Ti_3C_2T_x$ MXenes, Int. J. Hydrogen Energy 44 (2019) 788–800, https://doi.org/10.1016/j.ijhydene.2018.11.016.
[168] J.N. Chen, X.L. Yuan, F.L. Lyu, Q.X. Zhong, H.C. Hu, Q. Pan, Q. Zhang, Integrating MXene nanosheets with cobalt-tipped carbon nanotubes for an efficient oxygen reduction reaction, J. Mater. Chem. A 7 (2019) 1281–1286, https://doi.org/10.1039/C8TA10574J.
[169] B.W. Deng, Z. Xiang, J. Xiong, Z.C. Liu, L.Z. Yu, W. Lu, Sandwich-like Fe&TiO_2@C nanocomposites derived from MXene/Fe-MOFs hybrids for electromagnetic absorption, Nano-Micro Lett. 12 (2020) 55, https://doi.org/10.1007/s40820-020-0398-2.
[170] C.L. Liu, Y. Bai, W.T. Li, F.Y. Yang, G.X. Zhang, H. Pang, In situ growth of three-dimensional MXene/metal-organic framework composites for high-performance supercapacitors, Angew. Chem. Int. Ed. 61 (2022) e202116282, https://doi.org/10.1002/anie.202116282.
[171] N. Kitchamsetti, D. Kim, Facile synthesis of hierarchical core–shell heterostructured ZnO/SnO_2@$NiCo_2O_4$ nanorod sheet arrays on carbon cloth for high performance quasi-solid-state asymmetric supercapacitors, J. Mater. Res. Technol. 21 (2022) 590–603, https://doi.org/10.1016/j.jmrt.2022.09.041.
[172] N. Kitchamsetti, Y.R. Ma, P.M. Shirge, R.S. Devan, Mesoporous perovskite of interlocked nickel titanate nanoparticles for efficient electrochemical supercapacitor electrode, J. Alloys Compd. 833 (2020) 155134, https://doi.org/10.1016/j.jallcom.2020.155134.
[173] N. Kitchamsetti, P.N. Didwal, S.R. Mulani, M.S. Patil, R.S. Devan, Photocatalytic activity of $MnTiO_3$ perovskite nanodiscs for the removal of organic pollutants, Heliyon 7 (2021) e07297, https://doi.org/10.1016/j.heliyon.2021.e07297.
[174] N. Kitchamsetti, M. Samtham, P.N. Didwal, D. Kumar, D. Singh, S. Bimli, P. R. Chikate, D.A. Basha, S. Kumar, C.J. Park, S. Chakraborty, R.S. Devan, Theory abide experimental investigations on morphology driven enhancement of electrochemical energy storage performance for manganese titanate perovskites electrodes, J. Power Sources 538 (2022) 231525, https://doi.org/10.1016/j.jpowsour.2022.231525.
[175] N. Kitchamsetti, R.S. Kalubarme, P.R. Chikate, C.J. Park, Y.R. Ma, P.M. Shirage, R. S. Devan, An investigation on the effect of Li-ion cycling on the vertically aligned Brookite TiO_2 nanostructure, ChemistrySelect 4 (2019) 6620, https://doi.org/10.1002/slct.201900395.
[176] N. Kitchamsetti, P.R. Chikate, R.A. Patil, Y.R. Ma, P.M. Shirage, R.S. Devan, Perforated mesoporous NiO nanostructures for an enhanced pseudocapacitive performance with ultra-high rate capability and high energy density, CrystEngComm 21 (2019) 7130–7140, https://doi.org/10.1039/C9CE01475F.
[177] M.S. Patil, N. Kitchamsetti, S.R. Mulani, S.R. Rondiya, N.G. Deshpande, R.A. Patil, R.W. Cross, N.Y. Dzade, K.K. Sharma, P.S. Patil, Y.R. Ma, H.K. Cho, R.S. Devan, Photocatalytic behavior of $Ba(Sb/Ta)_2O_6$ perovskite for reduction of organic pollutants: experimental and DFT correlation, J. Taiwan Inst. Chem. Eng. 122 (2021) 201–209, https://doi.org/10.1016/j.jtice.2021.04.032.
[178] Y.P. Qu, C.J. Shi, H.F. Cao, Y.Z. Wang, Synthesis of Ni-MOF/$Ti_3C_2T_x$ hybrid nanosheets via ultrasonic method for supercapacitor electrodes, Mater. Lett. 280 (2020) 128526, https://doi.org/10.1016/j.matlet.2020.128526.
[179] Y.Y. Wen, Z.T. Wei, C. Ma, X.F. Xing, Z.X. Li, D. Luo, MXene boosted CoNi-ZIF-67 as highly efficient electrocatalysts for oxygen evolution, Nanomaterials 9 (2019) 775, https://doi.org/10.3390/nano9050775.
[180] H.B. Zhang, Z. Li, Z.Y. Hou, H. Mei, Y. Feng, B. Xu, D.F. Sun, Self-assembly of MOF on MXene nanosheets and in-situ conversion into superior nickel phosphates/MXene battery-type electrode, Chem. Eng. J. 425 (2021) 130602, https://doi.org/10.1016/j.cej.2021.130602.
[181] X.R. Bu, F. Ma, Q. Wu, H.Y. Wu, Y.B. Yuan, L. Hu, C.Y. Han, X.L. Wang, W.H. Liu, X. Li, Metal-organic frameworks-derived Co_3O_4/$Ti_3C_2T_x$ Mxene nanocomposites for high performance ethanol sensing, Sens. Actuators B Chem. 369 (2022) 132232, https://doi.org/10.1016/j.snb.2022.132232.
[182] C.F. Du, Q.T. Song, Q.H. Liang, X.Y. Zhao, J.J. Wang, R.C. Zhi, Y.X. Wang, H. Yu, The passive effect of MXene on electrocatalysis: a case of $Ti_3C_2T_x$/CoNi-MOF nanosheets for oxygen evolution reaction, ChemNanoMat 7 (2021) 539–544, https://doi.org/10.1002/cnma.202100061.
[183] L.T. Shi, C.C. Wu, Y. Wang, Y.H. Dou, D. Yuan, H. Li, H.W. Huang, Y. Zhang, I. D. Gates, X.D. Sun, T.Y. Ma, Rational design of coordination bond connected metal organic frameworks/MXene hybrids for efficient solar water splitting, Adv. Funct. Mater. 32 (2022) 2202571, https://doi.org/10.1002/adfm.202202571.
[184] D. Cheng, P.P. Li, X.H. Zhu, M.L. Liu, Y.Y. Zhang, Y. Liu, Enzyme-free electrochemical detection of hydrogen peroxide based on the three-dimensional flower-like cu-based metal organic frameworks and MXene nanosheets, Chin. J. Chem. 39 (2021) 2181–2187, https://doi.org/10.1002/cjoc.202100158.
[185] Y. Chen, S.B. Li, L. Zhang, T. Jing, J.X. Wang, L.J. Zhao, F.B. li, C. Li, J.Y. Sun, Facile and fast synthesis of three-dimensional Ce-MOF/$Ti_3C_2T_x$ MXene composite for high performance electrochemical sensing of L-Tryptophan, J. Solid State Chem. 308 (2022) 122919, doi:https://doi.org/10.1016/j.jssc.2022.122919.
[186] W.L. Xiang, Y.P. Zhang, H.F. Lin, C.J. Liu, Nanoparticle/metal-organic framework composites for catalytic applications: current status and perspective, Molecules 22 (2017) 2103, https://doi.org/10.3390/molecules22122103.
[187] Y.T. Sun, M. Xie, H.F. Feng, H. Liu, Efficient visible-light-driven photocatalytic hydrogen generation over 2D/2D Co-ZIF-9/Ti_3C_2 hybrids, ChemPlusChem 87 (2022) e202100553, https://doi.org/10.1002/cplu.202100553.
[188] Y.Q. Xu, M. Xie, X.F. Li, F.Q. Shao, S.S. Li, S. Li, Y.C. Xu, J.R. Chen, F.G. Zeng, Y. Jiao, Regulating the electronic structure of Fe-based metal organic frameworks by electrodeposition of au nanoparticles for electrochemical overall water splitting, J. Colloid Interface Sci. 626 (2022) 426–434, https://doi.org/10.1016/j.jcis.2022.06.163.
[189] D.H. Duan, D.S. Guo, J. Gao, S.B. Liu, Y.F. Wang, Electrodeposition of cobalt-iron bimetal phosphide on Ni foam as a bifunctional electrocatalyst for efficient overall water splitting, J. Colloid Interface Sci. 622 (2022) 250–260, https://doi.org/10.1016/j.jcis.2022.04.127.
[190] Y.X. Shi, G.Y. Zhu, X.T. Guo, Q.L. Jing, H. Pang, Y.Z. Zhang, Three-dimensional MXene-encapsulated porous Ni-NDC nanosheets as anodes for enhanced lithium-ion batteries, Nano Res. 16 (2023) 2528–2535, https://doi.org/10.1007/s12274-022-5168-7.
[191] Y.L. Wang, J. Song, W.Y. Wong, Constructing 2D sandwich-like MOF/MXene heterostructures for durable and fast aqueous zinc-ion batteries, Angew. Chem. Int. Ed. 62 (2023) e202218343, https://doi.org/10.1002/anie.202218343.
[192] W.W. Zhao, J. Peng, W.K. Wang, B.B. Jin, T.T. Chen, S.J. Liu, Q. Zhao, W. Huang, Interlayer hydrogen-bonded metal porphyrin frameworks/MXene hybrid film with high capacitance for flexible all-solid-state supercapacitors, Small 15 (2019) 1901351, https://doi.org/10.1002/smll.201901351.
[193] K.F. Yu, L. Tang, X. Cao, Z.H. Guo, Y. Zhang, N. Li, C.X. Dong, X. Gong, T. Chen, R. He, W.K. Zhu, Semiconducting metal-organic frameworks decorated with spatially separated dual Cocatalysts for efficient uranium(VI) photoreduction, Adv. Funct. Mater. 32 (2022) 2200315, https://doi.org/10.1002/adfm.202200315.
[194] R. Rauti, M. Musto, S. Bosi, M. Prato, L. Ballerini, Properties and behavior of carbon nanomaterials when interfacing neuronal cells: how far have we come? Carbon 143 (2019) 430–446, https://doi.org/10.1016/j.carbon.2018.11.026.
[195] C. Zhao, J. Kang, Y.W. Li, Y. Wang, X.Y. Tang, Z.Q. Jiang, Carbon-based stimuli-responsive nanomaterials: classification and application, Cyborg Bionic Syst. 4 (2023) 0022, https://doi.org/10.34133/cbsystems.0022.
[196] D. Liu, W.Y. Gu, L. Zhou, L.Z. Wang, J.L. Zhang, Y.D. Liu, J.Y. Lei, Recent advances in MOF-derived carbon-based nanomaterials for environmental applications in adsorption and catalytic degradation, Chem. Eng. J. 427 (2022) 131503, https://doi.org/10.1016/j.cej.2021.131503.
[197] S.J. Xu, A.R. Dong, Y. Hu, Z. Yang, S.M. Huang, J.J. Qian, Multidimensional MOF-derived carbon nanomaterials for multifunctional applications, J. Mater. Chem. A 11 (2023) 9721–9747, https://doi.org/10.1039/D3TA00239J.
[198] L.J. Mao, Y.J. Ge, D.D. Chen, Y.D. Yang, S.J. Xu, J.H. Xue, K.K. Xiao, X.M. Zhou, J. J. Qian, Z. Yang, Ligand-induced hollow MOF-derived carbon nanomaterials with abundant Fe species for efficient oxygen reduction, Sci. China Mater. 66 (2023) 2257–2265, https://doi.org/10.1007/s40843-022-2374-3.
[199] J.C. Ren, Y. Huang, H. Zhu, B.H. Zhang, H.K. Zhu, S.H. Shen, G.Q. Tan, F. Wu, H. He, S. Lan, X.H. Xia, Q. Liu, Recent progress on MOF-derived carbon materials for energy storage, carbon, Energy 2 (2020) 176–202, https://doi.org/10.1002/cey2.44.
[200] G.Y. Jiang, N. Zheng, X. Chen, G.Y. Ding, Y.H. Li, F.G. Sun, Y.S. Li, In-situ decoration of MOF-derived carbon on nitrogen-doped ultrathin MXene nanosheets to multifunctionalize separators for stable Li-S batteries, Chem. Eng. J. 373 (2019) 1309–1318, https://doi.org/10.1016/j.cej.2019.05.119.
[201] Y. Chen, H. Guo, F. Yang, N. Wu, J.Y. Zhang, L.P. Peng, B.Q. Liu, Z.L. Pan, W. Yang, Ni@NC@NiCo-LDH nanocomposites from a sacrificed template Ni@NC@ZIF-67 for high performance supercapacitor, Int. J. Hydrogen Energy 47 (2022) 29636–29647, https://doi.org/10.1016/j.ijhydene.2022.06.299.
[202] Z. Yang, Q.H. Cheng, W.W. Li, Y.J. Li, C. Yang, K. Tao, L. Han, Construction of 2D ZIF-derived hierarchical and hollow NiCo-LDH “nanosheet-on-nanosheet” arrays on reduced graphene oxide/Ni foam for boosted electrochemical energy storage, J. Alloys Compd. 850 (2021) 156864, https://doi.org/10.1016/j.jallcom.2020.156864.

[203] D.K. Yadav, J. Muhommad, S. Deka, Metal-organic framework-derived ZnCoNi-layered double-hydroxide nanosheets with charge storage characteristics for supercapacitors, ACS Appl. Nano Mater. 6 (2023) 13513–13523, https://doi.org/10.1021/acsanm.3c02176.
[204] K. Chhetri, A. Muthurasu, B. Dahal, T. Kim, T. Mukhiya, S.H. Chae, T.H. Ko, Y. C. Choi, H.Y. Kim, Engineering the abundant heterointerfaces of integrated bimetallic sulfide-coupled 2D MOF-derived mesoporous CoS_2 nanoarray hybrids for electrocatalytic water splitting, Mater. Today Nano 17 (2022) 100146, https://doi.org/10.1016/j.mtnano.2021.100146.
[205] C.L. Liu, W.H. Feng, Y. Bai, H. Pang, Compositing MXenes with hierarchical ZIF-67/cobalt hydroxide via controllable in situ etching for a high-performance supercapacitor, Inorg. Chem. Front. 9 (2022) 5463–5468, https://doi.org/10.1039/D2QI01641A.
[206] Z.Q. Ye, Y. Jiang, L. Li, F. Wu, R.J. Chen, Self-assembly of 0D-2D heterostructure electrocatalyst from MOF and MXene for boosted lithium polysulfide conversion reaction, Adv. Mater. 33 (2021) 2101204, https://doi.org/10.1002/adma.202101204.
[207] H.H. Li, H. Zhang, M. Zarrabeitia, H.P. Liang, D. Geiger, U. Kaiser, A. Varzi, S. Passerni, Metal-organic framework derived copper chalcogenides-carbon composites as high-rate and stable storage materials for Na ions, Adv. Sustain. Syst. 6 (2022) 2200109, https://doi.org/10.1002/adsu.202200109.
[208] C.X. Miao, X.H. Xiao, Y. Gong, K. Zhu, K. Cheng, K. Ye, J. Yan, D.X. Cao, G. L. Wang, P.P. Xu, Facile synthesis of metal-organic framework-derived $CoSe_2$ nanoparticles embedded in the N-doped carbon nanosheet array and application for supercapacitors, ACS Appl. Mater. Interfaces 12 (2020) 9365–9375, https://doi.org/10.1021/acsami.9b22606.
[209] Z.W. Cao, R. Momen, S.S. Tao, D.Y. Xiong, Z.R. Song, X.H. Xiao, W.T. Deng, H. H. Hou, S. Yasar, S. Altin, F. Bulut, G.Q. Zou, X.B. Ji, Metal-organic framework materials for electrochemical supercapacitors, Nano-Micro Lett. 14 (2022) 181, https://doi.org/10.1007/s40820-022-00910-9.
[210] Y. Liu, X.M. Xu, Z.P. Shao, S.P. Jiang, Metal-organic frameworks derived porous carbon, metal oxides and metal sulfides-based compounds for supercapacitors application, Energy Storage Mater. 26 (2020) 1–22, https://doi.org/10.1016/j.ensm.2019.12.019.
[211] X.F. Yang, Y.H. Tian, S. Li, Y.P. Wu, Q.C. Zhang, D.S. Li, S.Q. Zhang, Heterogeneous Ni-MOF/V_2CT_x-MXene hierarchically-porous nanorods for robust and high energy density hybrid supercapacitors, J. Mater. Chem. A 10 (2022) 12225–12234, https://doi.org/10.1039/D2TA02114E.
[212] D.Y. Wang, D.Z. Zhang, Y. Yang, Q. Mi, J.H. Zhang, L.D. Yu, Multifunctional latex/polytetrafluoroethylene-based triboelectric nanogenerator for self-powered organ-like MXene/metal-organic framework-derived CuO nanohybrid ammonia sensor, ACS Nano 15 (2021) 2911–2919, https://doi.org/10.1021/acsnano.0c09015.
[213] J.J. Wang, X.Y. Yue, Z.K. Xie, A. Abudula, G.Q. Guan, MOFs-derived transition metal sulfide composites for advanced sodium ion batteries, Energy Storage Mater. 41 (2021) 404–426, https://doi.org/10.1016/j.ensm.2021.06.025.
[214] X. Liu, Y.Q. Li, Z.Y. Cao, Z.H. Yin, T.L. Ma, S. Chen, Current progress of metal sulfides derived from metal-organic frameworks for advanced electrocatalysis: potential electrocatalysts with diverse applications, J. Mater. Chem. A 10 (2022) 1617–1641, https://doi.org/10.1039/D1TA09925F.
[215] H.Y. Zou, B.W. He, P.Y. Kuang, J.G. Yu, K. Fan, Metal-organic framework-derived nickel-cobalt sulfide on ultrathin Mxene nanosheets for electrocatalytic oxygen evolution, ACS Appl. Mater. Interfaces 10 (2018) 22311–22319, https://doi.org/10.1021/acsami.8b06272.
[216] G.L. Xia, J.W. Su, M. Li, P. Jiang, Y. Yang, Q.W. Chen, A MOF-derived self-template strategy toward cobalt phosphide electrodes with ultralong cycle life and high capacity, J. Mater. Chem. A 5 (2017) 10321–10327, https://doi.org/10.1039/C7TA02600E.
[217] Q. Wang, Z.Q. Liu, H.Y. Zhao, H. Huang, H. Jiao, Y.P. Du, MOF-derived porous Ni_2P nanosheets as novel bifunctional electrocatalysts for the hydrogen and oxygen evolution reactions, J. Mater. Chem. A 6 (2018) 18720–18727, https://doi.org/10.1039/C8TA06491A.
[218] H. Zong, R.J. Qi, K. Yu, Z.Q. Zhu, Ultrathin Ti_2NTx MXene-wrapped MOF-derived CoP frameworks towards hydrogen evolution and water oxidation, Electrochim. Acta 393 (2021) 139068, https://doi.org/10.1016/j.electacta.2021.139068.
[219] J. Feng, S.H. Luo, Y.C. Lin, Y. Zhan, S.X. Yan, P.Q. Hou, Q. Wang, Y.H. Zhang, Metal-organic framework derived $CoSe_2$/N-doped carbon core-shell nanoparticles encapsulated in porous N-doped carbon nanotubes as high-performance anodes for sodium-ion batteries, J. Power Sources 535 (2022) 231444, https://doi.org/10.1016/j.jpowsour.2022.231444.
[220] D.J. Xiao, S.Q. Liu, K.M. Zhao, G.Y. Ye, Y. Su, W.W. Zhu, Z. He, Metal-organic framework-derived ultrasmall nitrogen-doped carbon-coated $CoSe_2$/ZnSe nanospheres as enhanced anode materials for sodium-ion batteries, Ionics 27 (2021) 3327–3337, https://doi.org/10.1007/s11581-021-04124-8.
[221] H.T. Mi, L.Y. Li, C.T. Zeng, Y.H. Jin, Q.Q. Zhang, K.L. Zhou, J.B. Liu, H. Wang, Cuboid-like phosphorus-doped metal-organic framework-derived $CoSe_2$ on carbon cloth as an advanced bifunctional oxygen electrocatalyst for rechargeable zinc-air batteries, J. Colloid Interface Sci. 633 (2023) 424–431, https://doi.org/10.1016/j.jcis.2022.11.116.
[222] S.Q. Guo, X.L. Xu, J.B. Liu, Q.Q. Zhang, H. Wang, Cohesive porous Co_3O_4/C composite derived from zeolitic imidazole framework-67 (ZIF-67) single-source precursor as supercapacitor electrode, J. Electrochem. Soc. 166 (2019) A960, https://doi.org/10.1149/2.0381906jes.
[223] F.J. Kong, J. Wang, J.Y. Chen, S. Tao, B. Qian, H.M. Luo, MOF-derived ultrasmall $CoSe_2$ nanoparticles encapsulated by an N-doped carbon matrix and their superior lithium/sodium storage properties, Chem. Commun. 56 (2020) 9218–9221, https://doi.org/10.1039/D0CC03113E.
[224] Y. Zhou, Y. Zhang, X.Z. Xu, S.L. Zhao, Z. Guo, K.H. Wu, C.H. Tan, Z.H. Wang, Bimetallic metal-organic framework derived metal-carbon hybrid for efficient reversible oxygen electrocatalysis, Front. Chem. 7 (2019) 747, https://doi.org/10.3389/fchem.2019.00747.
[225] W.T. Wang, N. Batool, T.H. Zhang, J. Liu, X.F. Han, J.H. Tian, R.Z. Yang, When MOFs meet MXenes: superior ORR performance in both alkaline and acidic solutions, J. Mater. Chem. A 9 (2021) 3952–3960, https://doi.org/10.1039/D0TA10811A.
[226] X.B. Liu, F.F. Liu, X.D. Zhao, L.Z. Fan, Constructing MOF-derived CoP-NC@MXene sandwich-like composite by in-situ intercalation for enhanced lithium and sodium storage, J. Materiomics 8 (2022) 30–37, https://doi.org/10.1016/j.jmat.2021.06.002.
[227] J. Liu, H.B. Zhang, R.H. Sun, Y.F. Liu, Z.S. Liu, A.G. Zhou, Z.Z. Yu, Hydrophobic, flexible, and lightweight MXene foams for high-performance electromagnetic-interference shielding, Adv. Mater. 29 (2017) 1702367, https://doi.org/10.1002/adma.201702367.
[228] S.J. Wang, D.S. Li, L. Jiang, Synergistic effects between MXenes and Ni chains in flexible and ultrathin electromagnetic interference shielding films, Adv. Mater. Interfaces 6 (2019) 1900961, https://doi.org/10.1002/admi.201900961.
[229] R. Li, X.Y. Ma, J.M. Li, J. Cao, H.Z. Gao, T.S. Li, X.Y. Zhang, L.C. Wang, Q. H. Zhang, G. Wang, C.Y. Hou, Y.G. Li, T. Palacios, Y.X. Lin, H.Z. Wang, X. Ling, Flexible and high-performance electrochromic devices enabled by self-assembled 2D TiO_2/MXene heterostructures, Nat. Commun. 12 (2021) 1587, https://doi.org/10.1038/s41467-021-21852-7.
[230] X. Tian, L. Yao, X.X. Cui, R.J. Zhao, T. Chen, X.C. Xiao, Y. Wang, A two-dimensional $Ti_3C_2T_x$ MXene@TiO_2/MoS_2 heterostructure with excellent selectivity for the room temperature detection of ammonia, J. Mater. Chem. A 10 (2022) 5505–5519, https://doi.org/10.1039/D1TA10773A.
[231] Q. Liao, M. He, Y.M. Zhou, S.X. Nie, Y.J. Wang, B.B. Wang, X.M. Yang, X.H. Bu, R. Wang, Rational construction of $Ti_3C_2T_x$/co-MOF-derived laminated co/TiO_2-C hybrids for enhanced electromagnetic wave absorption, Langmuir 34 (2018) 15854–15863, https://doi.org/10.1021/acs.langmuir.8b03238.
[232] M. Garai, M. Mahato, S.H. Nam, E. Kim, D. Seo, Y.H. Lee, V.H. Nguyen, S.W. Oh, P. Sambyal, H.J. Yoo, A.K. Taseer, S.A. Syed, H. Han, C.W. Ahn, J.W. Kim, I.K. Oh, Metal organic framework-MXene nanoarchitecture for fast responsive and ultra-stable electro-ionic artificial muscles, Adv. Funct. Mater. 33 (2022) 2212252, https://doi.org/10.1002/adfm.202212252.
[233] R. Luo, Z.Y. Li, R.X. Li, C.L. Jiang, R.J. Qi, M.Q. Liu, H.C. Lin, R. Huang, C.H. Luo, H. Peng, Ultrafine Ru nanoparticles derived from few-layered $Ti_3C_2T_x$ MXene templated MOF for highly efficient alkaline hydrogen evolution, Int. J. Hydrogen Energy 47 (2022) 32787–32795, https://doi.org/10.1016/j.ijhydene.2022.07.205.
[234] H. Guo, J.Y. Zhang, M.N. Xu, M.Y. Wang, F. Yang, N. Wu, T.T. Zhang, L. Sun, W. Yang, Zeolite-imidazole framework derived nickel-cobalt hydroxide on ultrathin MXene nanosheets for long life and high performance supercapacitance, J. Alloys Compd. 888 (2021) 161250, https://doi.org/10.1016/j.jallcom.2021.161250.
[235] L.Y. Hu, R.S. Xiao, X. Wang, X.S. Wang, C.L. Wang, J. Wen, W.L. Gu, C.Z. Zhu, MXene-induced electronic optimization of metal-organic framework-derived CoFe LDH nanosheet arrays for efficient oxygen evolution, Appl. Catal. Environ. 298 (2021) 120599, https://doi.org/10.1016/j.apcatb.2021.120599.
[236] K. Jayaramulu, M. Horn, A. Schneemann, H. Saini, A. Bakandritsos, V. Ranc, M. Petr, V. Stavila, C. Narayana, B. Scheibe, S. Kment, M. Otyepka, N.Z. Motta, D. Dubal, R. Zboril, R.A. Fischer, Covalent graphene-MOF hybrids for high-performance asymmetric supercapacitors, Adv. Mater. 33 (2021) 2004560, https://doi.org/10.1002/adma.202004560.
[237] X.H. Wu, Z.Y. Wang, M.Z. Yu, L.Y. Xiu, J.S. Qiu, Stabilizing the MXenes by carbon nanoplating for developing hierarchical nanohybrids with efficient lithium storage and hydrogen evolution capability, Adv. Mater. 29 (2017) 1607017, https://doi.org/10.1002/adma.201607017.
[238] T. Xiao, J. Jin, Y.F. Zhang, W. Xi, R. Wang, Y.S. Gong, B.B. He, H.W. Wang, Rational construction of 2D/2D $Ti_3C_2T_x$/NiCo MOF heterostructure for highly efficient Li^+ storage, Electrochim. Acta 427 (2022) 140851, https://doi.org/10.1016/j.electacta.2022.140851.
[239] A.K. Wei, L. Wang, Z. Li, Metal-organic framework derived binary-metal oxide/MXene composite as sulfur host for high-performance lithium-sulfur batteries, J. Alloys Compd. 899 (2022) 163369, https://doi.org/10.1016/j.jallcom.2021.163369.
[240] X.X. Guo, S. Geng, M.J. Zhuo, Y. Chen, M.J. Zaworotko, P. Cheng, Z.J. Zhang, The utility of the template effect in metal-organic frameworks, Coord. Chem. Rev. 391 (2019) 44–68, https://doi.org/10.1016/j.ccr.2019.04.003.
[241] H.J. Lee, W. Cho, M. Oh, Advanced fabrication of metal–organic frameworks: template-directed formation of polystyrene@ZIF-8 core-shell and hollow ZIF-8 microspheres, Chem. Commun. 48 (2012) 221–223, https://doi.org/10.1039/C1CC16213F.
[242] L. Feng, K.Y. Wang, J. Powell, H.C. Zhou, Controllable synthesis of metal-organic frameworks and their hierarchical assemblies, Matter 1 (2019) 801–824, https://doi.org/10.1016/j.matt.2019.08.022.
[243] N.A. Mazlan, F.S. Butt, A. Lewis, Y.H. Yang, S.Q. Yang, Y. Huang, The growth of metal-organic frameworks in the presence of graphene oxide: a mini review, Membranes 12 (2022) 501, https://doi.org/10.3390/membranes12050501.
[244] X. Qiu, X. Wang, Y.W. Li, Controlled growth of dense and ordered metal-organic framework nanoparticles on graphene oxide, Chem. Commun. 51 (2015) 3874–3877, https://doi.org/10.1039/C4CC09933H.

[245] C.Y. Ruan, D.D. Zhu, J.Q. Qi, Q.K. Meng, F.X. Wei, Y.J. Ren, Y.W. Sui, H. Zhang, MXene-modulated $CoNi_2S_4$ dendrite as enhanced electrode for hybrid supercapacitors, Surf. Interfaces 25 (2021) 101274, https://doi.org/10.1016/j.surfin.2021.101274.
[246] X. Zhang, S.X. Yang, W. Lu, D. Lei, Y.H. Tian, M.G. Guo, P.P. Mi, N. Qu, Y.Y. Zhao, MXenes induced formation of Ni-MOF microbelts for high-performance supercapacitors, J. Colloid Interface Sci. 592 (2021) 95–102, https://doi.org/10.1016/j.jcis.2021.02.042.
[247] B.Z. Lyu, Y.S. Choi, H.Y. Jing, C. Qian, H.S. Kang, S.J. Lee, J.H. Cho, 2D MXene-TiO_2 Core-Shell Nanosheets as a data-storage medium in memory devices, Adv. Mater. 32 (2020) 1907633, https://doi.org/10.1002/adma.201907633.
[248] H. Zeng, Z.H. Li, G.S. Li, X.Q. Cui, M.X. Jin, T.F. Xie, L. Liu, M.P. Jiang, X. Zhong, Y.W. Zhang, H. Zhang, K.K. Ba, Z.K. Yan, Y. Wang, S.Y. Song, K. Huang, S.H. Feng, Interfacial engineering of TiO_2/Ti_3C_2 MXene/carbon nitride hybrids boosting charge transfer for efficient photocatalytic hydrogen evolution, Adv. Energy Mater. 12 (2022) 2102765, https://doi.org/10.1002/aenm.202102765.
[249] J.Z. Feng, X.Q. Zhang, Y.T. Xu, H.Y. Ma, Y. Xue, L.J. Su, J.W. Lang, Y. Wang, S. R. Yang, X.B. Yan, Regulating the electrolyte ion types and exposed crystal facets for pseudocapacitive energy storage of transition metal nitrides, Energy Storage Mater. 46 (2022) 278–288, https://doi.org/10.1016/j.ensm.2022.01.024.
[250] B.Q. Wang, S.G. Liu, W.P. Sun, Y.X. Tang, H.G. Pan, M. Yan, Y.Z. Jiang, Intercalation Pseudocapacitance boosting ultrafast sodium storage in Prussian blue analogs, ChemSusChem 12 (2019) 2415–2420, https://doi.org/10.1002/cssc.201900582.
[251] M. Okubo, A. Sugahara, S. Kajiyama, A. Yamada, MXene as a charge storage host, Acc. Chem. Res. 51 (2018) 591–599, https://doi.org/10.1021/acs.accounts.7b00481.
[252] Z.P. Zhang, B.Z. Wang, H.B. Zhao, J.F. Liao, Z.C. Zhou, T.H. Liu, B.C. He, Q. Wei, S. Chen, H.Y. Chen, D.B. Kuang, Y. Li, G.C. Xing, Self-assembled lead-free double perovskite-MXene heterostructure with efficient charge separation for photocatalytic CO_2 reduction, Appl. Catal. Environ. 312 (2022) 121358, https://doi.org/10.1016/j.apcatb.2022.121358.
[253] B.B. Shao, Z.F. Liu, G.M. Zeng, H. Wang, Q.H. Liang, Q.Y. He, M. Cheng, C. Y. Zhou, L.B. Jiang, B. Song, Two-dimensional transition metal carbide and nitride (MXene) derived quantum dots (QDs): synthesis, properties, applications and prospects, J. Mater. Chem. A 8 (2020) 7508–7535, https://doi.org/10.1039/D0TA01552K.
[254] P.A. Shinde, A.M. Patil, S.C. Lee, E.G. Jung, S.C. Jun, Two-dimensional MXenes for electrochemical energy storage applications, J. Mater. Chem. A 10 (2022) 1105–1149, https://doi.org/10.1039/D1TA04642J.
[255] N. Raza, T. Kumar, V. Singh, K.H. Kim, Recent advances in bimetallic metal-organic framework as a potential candidate for supercapacitor electrode material, Coord. Chem. Rev. 430 (2021) 213660, https://doi.org/10.1016/j.ccr.2020.213660.
[256] Y.M. Zhang, X.L. Zhu, S. Sun, Q.R. Guo, M.G. Xu, G. Wu, Ordered interface engineering enabled high-performance $Ti_3C_2T_x$ MXene fiber-based supercapacitors, Energy Fuel 36 (2022) 7898–7907, https://doi.org/10.1021/acs.energyfuels.2c01882.
[257] L.G. Yue, L. Chen, X.Y. Wang, D.Z. Lu, W.L. Zhou, D.J. Shen, Q. Yang, S.F. Xiao, Y. Y. Li, Ni/co-MOF@aminated MXene hierarchical electrodes for high-stability supercapacitors, Chem. Eng. J. 451 (2023) 138687, https://doi.org/10.1016/j.cej.2022.138687.
[258] B.Z. Jia, H.L. Yang, L. Wang, Z.Q. Zhao, X.M. Wu, Synergistic interface-pillared Fe-MOF on 2D $Ti_3C_2T_x$ MXene electrode coupling toward high energy density, Appl. Surf. Sci. 602 (2022) 154386, https://doi.org/10.1016/j.apsusc.2022.154386.
[259] G. Wu, S. Sun, X.L. Zhu, Z.Y. Ma, Y. Zhang, N.Z. Bao, Microfluidic fabrication of hierarchical-ordered ZIF-L(Zn)@$Ti_3C_2T_x$ core-sheath fibers for high-performance asymmetric supercapacitors, Angew. Chem. Int. Ed. 61 (2022) e202115559, https://doi.org/10.1002/anie.202115559.
[260] A. Yadav, S. Singal, P. Soni, G. Singh, R.K. Sharma, Structural engineering and carbon enrichment in V_2CT_x MXene: an approach for enhanced supercapacitive charge storage, J. Alloys Compd. 934 (2023) 167859, https://doi.org/10.1016/j.jallcom.2022.167859.
[261] R. Ramachandran, C.H. Zhao, M. Rajkumar, K. Rajavel, P.L. Zhu, W.L. Xuan, Z. X. Xu, F. Wang, Porous nickel oxide microsphere and $Ti_3C_2T_x$ hybrid derived from metal-organic framework for battery-type supercapacitor electrode and non-enzymatic H_2O_2 sensor, Electrochim. Acta 322 (2019) 134771, https://doi.org/10.1016/j.electacta.2019.134771.
[262] A.G. Olatoye, W.L. Li, E.O. Fagbohun, X. Zeng, Y.H. Zheng, Y.B. Cui, High-performance asymmetric supercapacitor based on nickel-MOF anchored MXene//NPC/rGO, J. Electroanal. Chem. 928 (2023) 117036, https://doi.org/10.1016/j.jelechem.2022.117036.
[263] X.F. Yang, C.M. Xu, S. Li, Y.P. Wu, X.Q. Wu, Y.M. Yin, D.S. Li, Thermal treatment for promoting interfacial interaction in co-BDC/$Ti_3C_2T_x$ hybrid nanosheets for hybrid supercapacitors, J. Colloid Interface Sci. 617 (2022) 633, https://doi.org/10.1016/j.jcis.2022.03.015.
[264] C. Zhang, L. Wang, W. Lei, Y.T. Wu, C.W. Li, M.A. Khan, Y. Ouyang, X.Y. Jiao, H. T. Ye, S. Mutahir, Q.L. Hao, Achieving quick charge/discharge rate of 3.0 V s^{-1} by 2D titanium carbide (MXene) via N-doped carbon intercalation, Mater. Lett. 234 (2019) 21–25, https://doi.org/10.1016/j.matlet.2018.08.124.
[265] W.Y. Xie, Y.Z. Wang, J. Zhou, M. Zhang, J.L. Yu, C.Z. Zhu, J. Xu, MOF-derived $CoFe_2O_4$ nanorods anchored in MXene nanosheets for all pseudocapacitive flexible supercapacitors with superior energy storage, Appl. Surf. Sci. 534 (2020) 147584, https://doi.org/10.1016/j.apsusc.2020.147584.
[266] J.Q. Qi, M.Y. Huang, C.Y. Ruan, D.D. Zhu, L. Zhu, F.X. Wei, Y.W. Sui, Q.K. Meng, Construction of $CoNi_2S_4$ nanocubes interlinked by few-layer $Ti_3C_2T_x$ MXene with high performance for asymmetric supercapacitors, Rare Metals 41 (2022) 4116–4126, https://doi.org/10.1007/s12598-022-02167-y.
[267] T.T. Yu, S.B. Li, L. Zhang, F.B. Li, J.X. Wang, H. Pan, D.Q. Zhang, In situ growth of ZIF-67-derived nickel-cobalt-manganese hydroxides on 2D V_2CT_x MXene for dual-functional orientation as high-performance asymmetric supercapacitor and electrochemical hydroquinone sensor, J. Colloid Interface Sci. 629 (2023) 546–558, https://doi.org/10.1016/j.jcis.2022.09.107.
[268] X. Chen, K.Y. Wang, K. Xie, H.J. Tao, Y.Q. Wang, MXene-coated nickel ion-exchanged ZIF skeleton-cavity layered double hydroxides for supercapacitors, Energy Fuel 37 (2023) 763–773, https://doi.org/10.1021/acs.energyfuels.2c03589.
[269] L. Luo, Y.L. Zhou, W. Yan, G.B. Du, M. Fan, W.G. Zhao, Construction of advanced zeolitic imidazolate framework derived cobalt sulfide/MXene composites as high-performance electrodes for supercapacitors, J. Colloid Interface Sci. 615 (2022) 282–292, https://doi.org/10.1016/j.jcis.2022.02.001.
[270] W.H. Wei, S.J. Luo, Y. Zhao, X.M. Li, B. Liang, J.Z. Fang, M. Luo, A solution-assisted etching preparation of an MOF-derived $NH_4CoPO_4.H_2O/Ti_3C_2T_x$ MXene nanocomposite for high-performance hybrid supercapacitors, New J. Chem. 45 (2021) 11174–11182, https://doi.org/10.1039/D1NJ01394G.
[271] H. Guo, J.Y. Zhang, F. Yang, M.Y. Wang, T.T. Zhang, Y.R. Hzo, W. Yang, Sandwich-like porous MXene/Ni_3S_4/CuS derived from MOFs as superior supercapacitor electrode, J. Alloys Compd. 906 (2022) 163863, https://doi.org/10.1016/j.jallcom.2022.163863.
[272] Y.A. Deng, Y.Y. Shen, Y. Du, T. Goto, J.F. Zhang, A novel electrode hybrid of N-$Ti_3C_2T_x$/C/CuS fabricated using ZIF-67 as an intermediate derivation for superhigh electrochemical properties of supercapacitors, J. Mater. Res. Technol. 19 (2022) 3507–3520, https://doi.org/10.1016/j.jmrt.2022.06.118.
[273] H. Shi, S. Chen, W. Shi, Z.F. Peng, J.Y. Li, Z. Liu, G.Y. Zhang, L. Liu, High performance fiber-shaped supercapacitors based on core-shell fiber electrodes with adjustable surface wrinkles and robust interfaces, J. Mater. Chem. A 9 (2021) 16852–16859, https://doi.org/10.1039/D1TA04007C.
[274] M.S. Asl, R. Hadi, L. Salehghadimi, A.G. Tabrizi, S. Farhoudian, A. Babapoor, M. Pahlevani, Flexible all-solid-state supercapacitors with high capacitance, long cycle life, and wide operational potential window: recent progress and future perspectives, J. Energy Storage 50 (2022) 104223, https://doi.org/10.1016/j.est.2022.104223.
[275] J. Huang, K. Yuan, Y.W. Chen, Wide voltage aqueous asymmetric supercapacitors: advances, strategies, and challenges, Adv. Funct. Mater. 32 (2022) 2108107, https://doi.org/10.1002/adfm.202108107.
[276] Y.D. Wei, M.M. Zheng, W.L. Luo, B. Dai, J.J. Ren, M.L. Ma, T.X. Li, Y. Ma, All pseudocapacitive MXene-MnO_2 flexible asymmetric supercapacitor, J. Energy Storage 45 (2022) 103715, https://doi.org/10.1016/j.est.2021.103715.
[277] E. Olsson, J. Yu, H.Y. Zhang, H.M. Cheng, Q. Cai, Atomic-scale design of anode materials for alkali metal (Li/Na/K)-ion batteries: progress and perspectives, Adv. Energy Mater. 12 (2022) 2200662, https://doi.org/10.1002/aenm.202200662.
[278] H. Zong, L. Hu, Z.G. Wang, R.J. Qi, K. Yu, Z.Q. Zhu, Metal-organic frameworks-derived CoP anchored on MXene toward an efficient bifunctional electrode with enhanced lithium storage, Chem. Eng. J. 416 (2021) 129102, https://doi.org/10.1016/j.cej.2021.129102.
[279] L.J. Sun, H.L. Wang, S.L. Zhai, J. Sun, X. Fang, H.Y. Yang, D. Zhai, C.C. Liu, W. Q. Deng, H. Wu, Dual-conductive metal-organic framework@MXene heterogeneity stabilizes lithium-ion storage, J. Energy Chem. 76 (2023) 368–376, https://doi.org/10.1016/j.jechem.2022.09.035.
[280] Y.H. Zheng, X.L. Gao, C.Y. Miao, H.H. Dai, Z.M. Xia, H.F. Wang, Z.J. Yao, J. Y. Zhou, G.Z. Sun, $Co_2V_2O_7$@$Ti_3C_2T_x$ MXene hollow structures synergizing the merits of conversion and intercalation for efficient Lithium ion storage, Adv. Sustain. Syst. 6 (2022) 2200153, https://doi.org/10.1002/adsu.202200153.
[281] W.L. Wu, C.H. Zhao, H. Liu, T.T. Liu, L. Wang, J.F. Zhu, Hierarchical architecture of two-dimensional Ti_3C_2 nanosheets@metal-organic framework derivatives as anode for hybrid li-ion capacitors, J. Colloid Interface Sci. 623 (2022) 216–225, https://doi.org/10.1016/j.jcis.2022.05.038.
[282] C.Y. Li, Z.Q. Dai, W. Liu, P. Kantichaimongkol, P.F. Yu, P. Pattananuwat, J.Q. Qin, X.Y. Zhang, A self-sacrifice template strategy to synthesize co-LDH/MXene for lithium-ion batteries, Chem. Commun. 57 (2021) 11378–11381, https://doi.org/10.1039/D1CC04492C.
[283] J.J. Zhong, L. Qin, J.L. Li, Z. Yang, K. Yang, M.J. Zhang, MOF-derived molybdenum selenide on $Ti_3C_2T_x$ with superior capacitive performance for lithium-ion capacitors, Int. J. Miner. Metall. Mater. 29 (2022) 1061–1072, https://doi.org/10.1007/s12613-022-2469-5.
[284] P. Zhang, J.Y. Chen, L.F. Feng, M.C. Jiang, B. Xu, Dual confinement of Si nanoparticles in a MXene/ZIF-8-derived carbon framework for lithium-ion batteries, ACS Appl. Nano Mater. 5 (2022) 12720–12728, https://doi.org/10.1021/acsanm.2c02594.
[285] L. Hong, S.L. Ju, Y.H. Yang, J. Zheng, G.L. Xia, Z.G. Huang, X.Y. Liu, X.B. Yu, Hollow-shell structured porous $CoSe_2$ microspheres encapsulated by MXene nanosheets for advanced lithium storage, sustainable, Energy Fuel 4 (2020) 2352–2362, https://doi.org/10.1039/C9SE01271K.
[286] Q. Li, Q.Z. Jiao, Y. Yan, H.J. Li, W. Zhou, T.T. Gu, X.R. Shen, C.X. Lu, Y. Zhao, Y. Y. Zhang, H.S. Li, C.H. Feng, Optimized co-S bonds energy and confinement effect of hollow MXene@CoS_2/NC for enhanced sodium storage kinetics and stability, Chem. Eng. J. 450 (2022) 137922, https://doi.org/10.1016/j.cej.2022.137922.
[287] E.Z. Xu, P.C. Li, J.J. Quan, H.W. Zhu, L. Wang, Y. Chang, Z.J. Sun, L. Chen, D. Yu, Y. Jiang, Dimensional gradient structure of $CoSe_2$@CNTs-MXene anode assisted

by ether for high-capacity, stable sodium storage, Nano-Micro Lett. 13 (2021) 40, https://doi.org/10.1007/s40820-020-00562-7.
[288] M.Q. Wang, X.L. Liu, B.Y. Qin, Z.Y. Li, Y.F. Zhang, W. Yang, H.S. Fan, In-situ etching and ion exchange induced 2D-2D MXene@Co_9S_8/$CoMo_2S_4$ heterostructure for superior Na^+ storage, Chem. Eng. J. 451 (2023) 138508, https://doi.org/10.1016/j.cej.2022.138508.
[289] X.L. Liu, Z.T. Liu, W. Yang, M.Q. Wang, B.Y. Qin, Y.F. Zhang, Z. Liu, H.S. Fan, In situ fragmented and confined CoP nanocrystals into sandwich-structure MXene@CoP@NPC heterostructure for superior sodium-ion storage, Mater. Today Chem. 26 (2022) 101002, https://doi.org/10.1016/j.mtchem.2022.101002.
[290] H.W. Zhang, D.P. Xiong, Y.D. Xie, K.D. Wu, Z.Y. Feng, K.H. Wen, Z.Y. Li, M. He, Co_3C/Mxene composites wrapped in N-rich carbon as stable-performance anodes for potassium/sodium-ion batteries, Colloids Surf. A Physicochem. Eng. Asp. 656 (2023) 130332, https://doi.org/10.1016/j.colsurfa.2022.130332.
[291] R.X. Hu, D.W. Sha, X. Cao, C.J. Lu, Y.C. Wei, L. Pan, Z.M. Sun, Anchoring metal-organic framework-derived ZnTe@C onto elastic $Ti_3C_2T_x$ MXene with 0D/2D dual confinement for ultrastable potassium-ion storage, Adv. Energy Mater. 12 (2022) 2203118, https://doi.org/10.1002/aenm.202203118.
[292] L.J. Sun, J. Sun, S.L. Zhai, T.T. Dong, H.Y. Yang, Y. Tan, X. Fang, C.C. Liu, W. Q. Deng, H. Wu, Homologous MXene-derived electrodes for potassium-ion full batteries, Adv. Energy Mater. 12 (2022) 2200113, https://doi.org/10.1002/aenm.202200113.
[293] R.Z. Li, D.S. Wang, Understanding the structure-performance relationship of active sites at atomic scale, Nano Res. 15 (2022) 6888–6923, https://doi.org/10.1007/s12274-022-4371-x.
[294] L. Hu, Q.W. Chen, Hollow/porous nanostructures derived from nanoscale metal–organic frameworks towards high performance anodes for lithium-ion batteries, Nanoscale 6 (2014) 1236–1257, https://doi.org/10.1039/C3NR05192G.
[295] S.Q. Li, K. Wang, G. Zhang, S. Li, Y. Xu, X.D. Zhang, X. Zhang, S.G. Zheng, X. Z. Sun, Y.W. Ma, Fast charging anode materials for Lithium-ion batteries: current status and perspectives, Adv. Funct. Mater. 32 (2022) 2200796, https://doi.org/10.1002/adfm.202200796.
[296] X.L. Gao, Y. Zheng, J. Chang, H. Xu, Z.Y. Hui, H.H. Dai, H.F. Wang, Z.M. Xia, J. Y. Zhou, G.Z. Sun, Universal strategy for preparing highly stable PBA/$Ti_3C_2T_x$ MXene toward Lithium-ion batteries via chemical transformation, ACS Appl. Mater. Interfaces 14 (2022) 15298, https://doi.org/10.1021/acsami.2c01382.
[297] F.X. Xie, L. Zhang, C. Ye, M.T. Jaroniec, S.Z. Qiao, The application of hollow structured anodes for sodium-ion batteries: from simple to complex systems, Adv. Mater. 31 (2019) 1800492, https://doi.org/10.1002/adma.201800492.
[298] A. Mauger, C.M. Julien, State-of-the-art electrode materials for sodium-ion batteries, Materials 13 (2020) 3453, https://doi.org/10.3390/ma13163453.
[299] Y.Y. Wang, W.P. Kang, D.F. Sun, Metal-organic assembly strategy for the synthesis of layered metal chalcogenide anodes for Na^+/K^+-ion batteries, ChemSusChem 16 (2023) e202202332, https://doi.org/10.1002/cssc.202202332.
[300] D.P. Qiu, Y.L. Hou, Carbon materials toward efficient potassium storage: rational design, performance evaluation and potassium storage mechanism, Green, Energy Environ. 8 (2023) 115–140, https://doi.org/10.1016/j.gee.2022.05.007.
[301] Y.L. Ren, Q.X. Zhai, B. Wang, L.B. Hu, Y.J. Ma, Y.M. Dai, S.C. Tang, X.K. Meng, Synergistic adsorption-electrocatalysis of 2D/2D heterostructure toward high performance Li-S batteries, Chem. Eng. J. 439 (2022) 135535, https://doi.org/10.1016/j.cej.2022.135535.
[302] T. Xiao, Y.F. Zhang, W. Xi, R. Wang, Y.S. Gong, B.B. He, H.W. Wang, J. Jin, Rationally designing a $Ti_3C_2T_x$/CNTs-Co_9S_8 heterostructure as a sulfur host with multi-functionality for high-performance lithium-sulfur batteries, Nanoscale 14 (2022) 16139–16147, https://doi.org/10.1039/D2NR04526E.
[303] X.Y. Zhou, Y.C. Cui, X. Huang, Q.Y. Zhang, B. Wang, S.C. Tang, Interface engineering of Fe_3Se_4/FeSe heterostructures encapsulated in MXene for boosting LiPS conversion and inhibiting shuttle effect, Chem. Eng. J. 457 (2023) 141139, https://doi.org/10.1016/j.cej.2022.141139.
[304] F.F. Liu, T.T. Wang, X.B. Liu, N. Jiang, L.Z. Fan, High-performance heterojunction Ti_3C_2/$CoSe_2$ with both intercalation and conversion storage mechanisms for magnesium batteries, Chem. Eng. J. 426 (2021) 130747, https://doi.org/10.1016/j.cej.2021.130747.
[305] Y.M. Zhang, J.M. Cao, Z. Yuan, H. Xu, D.D. Li, Y.L. Li, W. Han, L. Wang, TiVCT$_x$ MXene/chalcogenide heterostructure-based high-performance magnesium-ion battery as flexible integrated units, Small 18 (2022) 2202313, https://doi.org/10.1002/smll.202202313.
[306] L. Yao, S.L. Ju, T. Xu, X.B. Yu, Spatial isolation-inspired ultrafine $CoSe_2$ for high-energy aluminum batteries with improved rate cyclability, ACS Nano 15 (2021) 13662–13763, https://doi.org/10.1021/acsnano.1c04895.
[307] Y. Gao, Q.Y. Guo, Q. Zhang, Y. Cui, Z. Zheng, Fibrous materials for flexible Li-S battery, Adv. Energy Mater. 11 (2021) 2002580, https://doi.org/10.1002/aenm.202002580.
[308] H. Dong, O. Tutusaus, Y.L. Liang, Y. Zhang, Z.L. Higgins, W.L. Yang, R. Mohtadi, Y. Yao, High-power Mg batteries enabled by heterogeneous enolization redox chemistry and weakly coordinating electrolytes, Nat. Energy 5 (2020) 1043–1050, https://doi.org/10.1038/s41560-020-00734-0.
[309] J.M. Pan, X. Wang, H.K. Li, Z.H. Cui, H. Chen, J.N. Nie, H.B. Gou, D.M. Yu, C. G. Chen, Y.P. Liu, The conversion-type selenides as potential high-energy cathode materials for mg-based batteries: a review, ACS Sustain. Chem. Eng. 10 (2022) 14980–15006, https://doi.org/10.1021/acssuschemeng.2c05222.
[310] T.T. Lv, G.Y. Zhu, S.Y. Dong, Q.Q. Kong, Y. Peng, S. Jiang, G.X. Zhang, Z. Yang, S. Y. Yang, X.C. Dong, H. Pang, Y.Z. Zhang, Co-Intercalation of Dual Charge Carriers in Metal-Ion-Confining Layered Vanadium Oxide Nanobelts for Aqueous Zinc-Ion Batteries, Angew. Chem, Int. Ed. 62 (2022) e202216089, doi:https://doi.org/10.1002/anie.202216089.
[311] I.R. Tay, J.M. Xue, W.S.V. Lee, Methods for characterizing intercalation in aqueous zinc ion battery cathodes: a review, Adv. Sci. 10 (2023) 2303211, https://doi.org/10.1002/advs.202303211.
[312] G.A. Elia, K.V. Kravchyk, M.V. Kovalenko, J. Chacon, A. Holland, R.G.A. Wills, An overview and prospective on Al and Al-ion battery technologies, J. Power Sources 481 (2021) 228870, https://doi.org/10.1016/j.jpowsour.2020.228870.
[313] L.Q. Wang, L. Song, Z.Y. Yang, Y.M. Chang, F. Hu, L. Li, L.L. Li, H.Y. Chen, S. J. Peng, Electronic modulation of metal-organic frameworks by interfacial bridging for efficient pH-universal hydrogen evolution, Adv. Funct. Mater. 33 (2023) 2210322, https://doi.org/10.1002/adfm.202210322.
[314] J.P. Zhang, W.X. Zhang, J.M. Zhang, Y.X. Li, Y.L. Wang, L.Y. Yang, S.G. Yin, MOF-derived bimetallic NiMo-based sulfide electrocatalysts for efficient hydrogen evolution reaction in alkaline media, J. Alloys Compd. 935 (2023) 167974, https://doi.org/10.1016/j.jallcom.2022.167974.
[315] X.Q. Zhu, T.R. Zhu, Q.M. Chen, W.C. Peng, Y. Li, F.B. Zhang, X.B. Fan, FeP-CoP nanocubes in situ grown on $Ti_3C_2T_x$ MXene as efficient electrocatalysts for the oxygen evolution reaction, Ind. Eng. Chem. Res. 61 (2022) 10837–10845, https://doi.org/10.1021/acs.iecr.2c01745.
[316] C.M. Xu, X.F. Yang, S. Li, K. Li, B.J. Xi, Q.W. Han, Y.P. Wu, X.Q. Wu, R.A. Chi, D. S. Li, Modulating the electronic configuration of co species in MOF/MXene nanosheet derived Co-based mixed spinel oxides for an efficient oxygen evolution reaction, Inorg. Chem. Front. 10 (2022) 85–92, https://doi.org/10.1039/D2QI02098J.
[317] J.Z. Li, C. Chen, Z.P. Lv, W.S. Ma, M. Wang, Q. Li, J. Dang, Constructing heterostructures of ZIF-67 derived C, N doped Co_2P and $Ti_2VC_2T_x$ MXene for enhanced OER, J. Mater. Sci. Technol. 145 (2023) 74–82, https://doi.org/10.1016/j.jmst.2022.10.048.
[318] Z.W. Fang, C.X. Xu, X.L. Zhang, Y.C. Wang, T. Xiao, L. Wang, M. Chen, X.T. Liu, MXene ($Ti_3C_2T_x$)-supported binary Co-, Zn-doped carbon as oxygen reduction reaction catalyst for anion exchange membrane fuel cells, Energy Technol. 10 (2022) 2101168, https://doi.org/10.1002/ente.202101168.
[319] P.P. Tan, R.W. Gao, Y.W. Zhang, N. Han, Y.Z. Jiang, M.W. Xu, S.J. Bao, X. Zhang, Electrostatically directed assembly of two-dimensional ultrathin Co_2Ni-MOF/$Ti_3C_2T_x$ nanosheets for electrocatalytic oxygen evolution, J. Colloid Interface Sci. 630 (2023) 363–371, https://doi.org/10.1016/j.jcis.2022.10.109.
[320] J. Li, C. Chen, Z.P. Lv, W.S. Ma, M. Wang, Q. Li, J. Dang, Constructing heterostructures of ZIF-67 derived C, N doped Co_2P and $Ti_2VC_2T_x$ MXene for enhanced OER, J. Mater. Sci. Technol. 145 (2023) 74–82, https://doi.org/10.1016/j.jmst.2022.10.048.
[321] Y.C. Pi, Z.M. Qiu, Y. Sun, H. Ishii, Y.F. Liao, X.Y. Zhang, H.Y. Chen, H. Pang, Synergistic mechanism of sub-nanometric Ru clusters anchored on tungsten oxide nanowires for high-efficient bifunctional hydrogen electrocatalysis, Adv. Sci. 10 (2023) 2206096, https://doi.org/10.1002/advs.202206096.
[322] K.A. Adegoke, O.R. Adegoke, R.A. Adigun, N.W. Maxakato, O.S. Bello, Two-dimensional metal-organic frameworks: from synthesis to biomedical, environmental, and energy conversion applications, Coord. Chem. Rev. 473 (2022) 214817, https://doi.org/10.1016/j.ccr.2022.214817.
[323] E.V. Kondratenko, G. Mul, J. Baltrusaitis, G.O. Larrazabal, J.P. Ramirez, Status and perspectives of CO_2 conversion into fuels and chemicals by catalytic, photocatalytic and electrocatalytic processes, Energ. Environ. Sci. 6 (2013) 3112–3135, https://doi.org/10.1039/C3EE41272E.
[324] N. Li, X.Z. Chen, W.J. Ong, D.R. MacFarlane, X.J. Zhao, A.K. Cheetham, C.H. Sun, Understanding of electrochemical mechanisms for CO_2 capture and conversion into hydrocarbon fuels in transition-metal carbides (MXenes), ACS Nano 11 (2017) 10825–10833, https://doi.org/10.1021/acsnano.7b03738.
[325] Q. Zhao, C. Zhang, R.M. Hu, Z.G. Du, J.N. Gu, Y.L.S. Cui, X. Chen, W.J. Xu, Z. J. Cheng, S.M. Li, B. Li, Y.F. Liu, W.H. Chen, C.T. Liu, J.X. Shang, L. Song, S. B. Yang, Selective etching quaternary MAX phase toward single atom copper immobilized MXene ($Ti_3C_2Cl_x$) for efficient CO_2 electroreduction to methanol, ACS Nano 15 (2021) 4927–4936, https://doi.org/10.1021/acsnano.0c09755.
[326] Y. Li, Y.P. Chen, Z.L. Guo, C.C. Tang, B.S. Sa, N.H. Miao, J. Zhou, Z.M. Sun, Breaking the linear scaling relations in MXene catalysts for efficient CO_2 reduction, Chem. Eng. J. 429 (2022) 132171, https://doi.org/10.1016/j.cej.2021.132171.

Narasimharao Kitchamsetti received his Ph.D. from Indian Institute of Technology Indore, India in June 2021. Later, he joined Kyung Hee University as a postdoctoral fellow. Since 2022, he has been working as a postdoctoral researcher at Chungbuk National University in the Department of Engineering Chemistry. His current research interests include design of core-shell heterostructures, MXenes, MOFs, energy storage and environmental applications such as supercapacitors, metal ion batteries, and photocatalytic water treatment.

Jung Sang Cho received his Ph. D. from interdisciplinary program for bioengineering, college of engineering, Seoul national university, Korea in 2013, and had post-doc experience at the department of materials science and engineering, Korea university, Korea (2014-2016). He is currently a professor at the department of engineering chemistry, chungbuk national university, Korea since 2016. His research group works on the development of nanostructured materials for the energy storage, sensor, catalyst, display, and biomaterials. For details, please see the lab website: https://jjj777.wixsite.com/professor-cho/members.